

The Role of MHD Instabilities in the Improved H-Mode Scenario

Von der Fakultät Mathematik und Physik der Universität Stuttgart
zur Erlangung der Würde eines Doktors der
Naturwissenschaften (Dr. rer. nat) genehmigte Abhandlung

Vorgelegt von

Asher Flaws

aus Neuseeland

Hauptberichter:	Prof. Dr. U. Stroth
Mitberichter:	Prof. Dr. H. Zohm
Vorsitzender:	Prof. Dr. G. Wunner

Tag der mündlichen Prüfung: 16.02.2009

Institut für Plasmaforschung der Universität Stuttgart

2009

Abstract

Recently a regime of tokamak operation has been discovered, dubbed the improved H-mode scenario, which simultaneously achieves increased energy confinement and stability with respect to standard H-mode discharges. It has been suggested that magnetohydrodynamic (MHD) instabilities play some role in establishing this regime. In this thesis MHD instabilities were identified, characterised, and catalogued into a database of improved H-mode discharges in order to statistically examine their behaviour. The onset conditions of MHD instabilities were compared to existing models based on previous H-mode studies. Slight differences were found, most notably a reduced β_N onset threshold for the frequently interrupted regime for neoclassical tearing modes (NTM). This reduced threshold is due to the relatively low magnetic shear of the improved H-mode regime. This study also provided a first-time estimate for the seed island size of spontaneous onset NTMs, a phenomenon characteristic of the improved H-mode scenario. Energy confinement investigations found that, although the NTM impact on confinement follows the same model applicable to other operating regimes, the improved H-mode regime acts to mitigate the impact of NTMs by limiting the saturated island sizes for NTMs with toroidal mode number $n \geq 2$. Surprisingly, although a significant loss in energy confinement is observed during the sawtooth envelope, it has been found that discharges containing fishbones and low frequency sawteeth achieve higher energy confinement than those without. This suggests that fishbone and sawtooth reconnection may indeed play a role in establishing the high confinement regime. It was found that the time evolution of the central magnetic shear consistently locks in the presence of sawtooth and fishbone reconnection. Presumably this is due to the periodic redistribution of the central plasma current, an effect which is believed to help establish and maintain the characteristic current profile required for improved H-mode operation. A similar effect was proposed for the NTM instability whereby the magnetic island drives an additional toroidal current which flattens the central current density profile. However, it was found that the NTM impact on the toroidal current density could be accounted for purely in terms of the 3 conventional current contributions, namely: ohmic, bootstrap, and auxiliary heating current drive, without requiring an additional current source.

Zusammenfassung

In Sternen wechselwirken die Fusionspartner nur schwach und fusionieren somit mit relativ geringer Wahrscheinlichkeit. Zu Energiegewinnungszwecken auf der Erde benötigt man jedoch große Wechselwirkungsquerschnitte, weshalb man sich im Gegensatz zur kosmischen Wasserstofffusion im Fusionsexperiment auf die Deuterium-Tritium ($D - T$) Reaktion konzentriert. Deren Wahrscheinlichkeit liegt in etwa 25 Größenordnungen über der für die Fusion der leichten Wasserstoffkerne im Stern. Heutige Konzepte für Fusionreaktoren gehen von der Verwendung der $D - T$ aus.

Eines der Hauptziele der Kernfusionsforschung ist das Erreichen eines sogenannten gezündeten Fusionsplasmas, das sich durch die Kompensation der Energieverlust durch die beim Fusionsprozess entstehenden α -Teilchen auszeichnet. Um diese Zündbedingung zu erreichen, muss das Plasma heiss und dicht sein sowie ausreichende Wärmeisolation - charakterisiert durch die sogenannte Energieeinschlusszeit τ_E - aufweisen.

Vom heutigen Standpunkt aus betrachtet, gilt für den magnetischen Einschluss von Fusionsplasmen das ringförmige Tokamakexperiment als die aussichtsreichste experimentielle Anordnung, die Zündbedingung zu erreichen. Da die Fusionsleistung näherungsweise mit dem Quadrat des Plasmadruckes zunimmt wird zusätzlich zur Einschlusszeit auch β , das Verhältnis des Plasmadruckes zum magnetischen Druck, als charakteristische Maßzahl herangezogen.

Die Einschlusseigenschaften hängen stark vom Betriebsregime ab. Beispielsweise führt der "Hoch-Einschluss" Modus (H-Mode) durch die Herstellung einer Energie- und Teilchentransportbarriere in der äussersten Randschicht des Plasmavolumens zu deutlich erhöhten β - und τ_E -Werten. Das "Improved H-Mode" genannte Regime zeigt ebenfalls einen verbesserten Energieeinschluss der nach heutigem Verständnis durch einen speziellen radialen Verlauf der toroidalen Stromdichte im Plasma erzeugt wird. Dabei könnten auch magnetohydrodynamische (MHD) Instabilitäten eine Rolle spielen.

Das Ziel dieser Dissertation lag darin, die Rolle von MHD Instabilitäten in Improved H-Mode Entladungen zu verstehen und folgende Fragen zu beantworten: Welche Plasmabedingungen führen zur Destabilisierung von Instabilitäten? Was sind die Auswirkungen der Instabilitäten auf den Energieeinschluss und wie ändern die Instabilitäten das Stromprofil des Plasmas?

Eine Datenbank von Improved H-Mode Entladungen wurde zunächst erstellt, mit dem Ziel, die Rolle der in der folgenden Tabelle gelisteten MHD

Instabilitäten im Improved H-Mode Regime statistisch zu untersuchen

- Neoklassische Tearing Moden (NTM) - magnetische Inseln, getrieben durch das Druckprofil im Plasma
- Frequently Interrupted Regime NTM (FIR-NTM) - wie NTM Instabilität, jedoch wird die maximale Inselgröße durch periodische Stochastisierung limitiert
- Fishbones - Instabilitäten getrieben durch Teilchenresonanz mit Moden
- Sägezähne - periodische Relaxation des zentralen Strom- und Druckprofils

Entwickelt wurden neue Analysemethoden fuer die Auswertung von MHD-Moden, ein Korrelation-Spektrogrammsystem fuer die Mirnov-Spulen Diagnostik, ein Sägezahn-Detektionsalgorithmus für die Temperatureprofil-Diagnostik und ein soft X-ray Tomographiesystem. MHD Instabilitäten wurden damit identifiziert, charakterisiert und katalogisiert. Die Datenbank kombiniert Zeitfolgen von Instabilitäten mit Plasmabedingungen, schnellen Teilchen-Simulationen und Gleichgewichtsrekonstruktionen.

Wir haben zuerst die Einsatzbedingungen von Instabilitäten in Improved H-Mode Entladungen untersucht und diese mit dem Verhalten in Standard H-Mode verglichen. Alle Einsatzbedingungen zeigen gute Übereinstimmung mit der MHD Theorie, mit Ausnahme der FIR-NTM Instabilität. Der Schwellwert für das Frequently Interrupted Regime ist im Vergleich zu Standard H-Mode Entladungen gering, was auf das abgeflachte Stromprofil zurückzuführen ist.

NTMs in Improved H-Mode Entladungen wachsen regelmäßig ohne ein sichtbares Precursor Ereignis. Wir nennen solche NTMs Spontaneous Onset NTMs (SNTMs). Eine anfängliche Inselgröße von ungefähr 1.3 ± 0.7 cm wurde für SNTMs in Improved H-Mode Entladungen identifiziert, was Erwartungen der NTM-Theorie nahekommt (1.0 ± 0.4 cm).

Die Vorhersage der Einschlussniedrigung durch NTM-Aktivität gelingt mit dem Belt Model sowohl bei Improved H-Moden als auch im Falle der Standard H-Mode Entladungen. Das Improved H-Mode Szenario führt jedoch zur Abmilderung der Einschlussniedrigung durch Begrenzung der maximalen Inselgröße durch den FIR-NTM Mechanismus (bei NTMs) mit der toroidalen Modenzahl $n \geq 2$. Überraschenderweise findet man, dass trotz eines signifikanten Verlustes von zentralem Energieeinschluss durch

die Sawteeth-Instabilität, Entladungen mit Fishbones und niederfrequenter Sawtooth-Aktivität höheren Energieeinschluss zeigen als Entladungen ohne derartige Instabilitäten. Eine mögliche Erklärung dafür ist, dass die zwei Instabilitäten bei der Herstellung des für das Hocheinschlusszenario charakteristischen Stromprofils eine Rolle spielen.

Durch weitere Untersuchungen ist festgestellt worden, dass sich das zentrale Stromprofil nicht mehr verändert, sobald Fishbone- bzw. Sawtooth-Aktivität einsetzt, was sich in der periodischen Neuverteilung des Plasmasstroms gründet. Dieser Effekt soll bei der Erreichung eines abgeflachten Stromprofils, welches für Improved H-Mode Operation benötigt wird, ausgenutzt werden. Eine ähnliche Vorstellung existiert auch für NTMs, in der die magnetische Insel zusätzlichen Plasmastrom in toroidaler Richtung treiben und dabei ein Abflachen des Stromprofils verursachen soll. Jedoch ist in dieser Arbeit kein zusätzlicher Strom gefunden worden. Die Auswirkung von NTMs auf das Stromprofil konnte allein durch die drei Standardstrombeiträge (induktiv, druckgetrieben sowie durch Zusatzheizung erzeugt) erklärt werden, ohne eine vierte Komponente zu benötigen.

Contents

Abstract	ii
Abbreviations	ix
1 Introduction	1
2 Basics	7
2.1 Magneto Hydrodynamics	7
2.2 Plasma Equilibrium	8
2.2.1 The CLISTE Equilibrium Code	12
2.3 MHD Instabilities	14
2.3.1 Ideal Instabilities	14
2.3.2 Resistive Instabilities	15
2.3.3 Neo-classical Tearing Modes	16
2.3.4 Frequently Interrupted Regime NTM	20
2.3.5 The Fishbone Instability	21
2.3.6 The Sawtooth Instability	22
2.4 The Improved H-Mode Scenario	26
2.5 Toroidal Current in a Tokamak	28
2.5.1 The FAFNER Fast Particle Code	31
3 Diagnostics	33
3.1 Mirnov Coils	33
3.2 The Motional Stark Effect Diagnostic	35
3.3 The Electron Cyclotron Emission Diagnostic	36
3.4 The Soft X-ray Diagnostic	37
3.4.1 Mode Identification with the SXR Diagnostic	39

4	Soft X-ray Tomography	41
4.1	Maximum Entropy Regularisation	42
4.2	The Contribution Matrix	44
4.3	Rotation Tomography	45
4.4	Periodic Noise Reduction	50
4.5	Smoothness Constraint	50
4.6	Example: Disruption Reconstructions	51
5	MHD Instability Database	53
5.1	Correlated Spectrogram Analysis	53
5.2	Neoclassical Tearing Modes	56
5.2.1	Frequently Interrupted Regime NTMs	60
5.3	Fishbones	60
5.4	Sawteeth	61
5.4.1	Sawtooth Detection Algorithm, SAWSCAN	62
6	Onset Criteria and Characterisation of MHD Instabilities in Improved H-Mode	65
6.1	Neo-classical Tearing Modes	65
6.2	The Frequently Interrupted Regime	71
6.3	The Fishbone Instability	74
6.3.1	Suppression by NTMs	74
6.3.2	Suppression by a Sawtooth Crash	78
6.4	The Sawtooth Instability	80
6.4.1	Compound Sawteeth	81
6.4.2	Reconstructions Using SXR Tomography	84
7	MHD Modes and Confinement	91
7.1	Testing The Belt Model for Confinement Loss	91
7.2	Sawteeth, Fishbones and Confinement	95
8	MHD Modes and the Current Profile	99
8.1	Sawtooth and Fishbone Reconnection	99
8.2	Impact of NTMs on the Current Density Profile	101
9	Conclusions	107

A ASDEX Upgrade	113
Bibliography	114
Acknowledgements	120

List of Abbreviations

ASDEX	A xial S ymmetric D ivertor E xperiment
CLISTE	C omplete I nterpretive S uite for T okamak E quilibria
ECE	E lectron C yclotron E mission
FIR	F requently I nterrupted R egime for NTM
FWHM	F ull W idth at H alf M aximum
ITER	I nternational T hermonuclear E xperimental R eactor
LCFS	L ast C losed F lux S urface
MHD	M agneto- h ydrodynamic
MSE	M otional S tark E ffect
NBI	N eutral B eam I njection
NTM	N eo-classical T earing M ode
PNTM	P recursor triggered NTM
PSL	P assive S tabilisation L oop
SNTM	S pontaneous onset NTM
SVD	S ingular V alue D ecomposition
SXR	S oft X -ray

Chapter 1

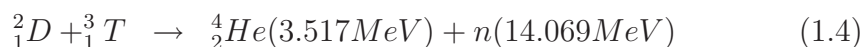
Introduction

The ever growing demand for energy from civilisation and industry has become an increasing concern over the last 100 years. Renewable energy sources such as wind, solar, and hydroelectric power are unable to satisfy all of this demand. Exhaustible resources such as coal, natural gas, and crude oil have become increasingly scarce. Additionally, the burning of these fossil fuels contributes greatly to atmospheric carbon pollution. Nuclear fission provides an alternative. However, the long half life radioactive waste produced by such power plants is widely held as an environmental risk. These factors combine to motivate a search for a new energy source, and this leads us to nuclear fusion power.

By far the most common source of energy in the universe, nuclear fusion is the process that powers stars. Under temperatures of the order of several million Kelvin, light elements, such as hydrogen, can fuse to form heavier nuclei with a lower average energy per nucleon. This missing energy is released as energetic particles or gamma rays. In stars, the immense pressures required are provided simply by gravity. The sheer weight of the stellar mass drives extreme pressures at the centre of the star. For example, our own star the sun has a core temperature of the order of 15×10^6 °K, and 340×10^9 atm pressure. This results in the following 3 stage nuclear reaction from hydrogen to helium:



Recreating these conditions on the Earth is difficult. We are therefore forced to use a different reaction using isotopes of hydrogen: deuterium and tritium. A reaction chosen for its high cross section at low temperatures, see fig 1.1, and carried out at much lower densities,¹:



The energetic α particles released in this reaction are expected to provide enough heating to sustain the reaction without the need for external heating, while the neutrons escaping the vessel will be used to extract the gained power. The planned ITER (International Thermonuclear Experimental Reactor) will test the efficiency of the α particle heating.

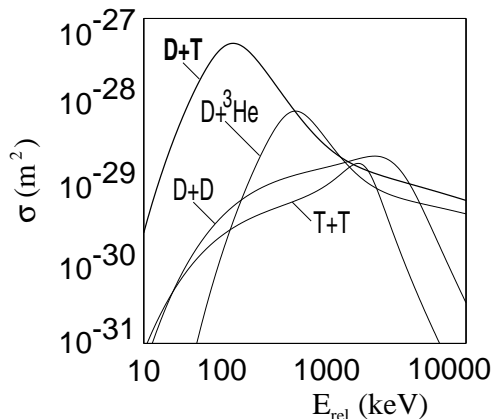


Figure 1.1: Fusion reaction cross sections.

move perpendicular to the toroidal field and thereby escape the confinement region. However, this is not enough to ensure a good confinement, as the gyrating electrons and ions will diverge due to a $B \times \nabla B$ force. This divergence gives rise to an electric field, which in turn leads to an $E \times B$ drift of particles

¹At least in the case of magnetic confinement fusion, where the plasma pressure is of the order of 1atm .

out of the torus. This drift can be compensated by imposing a helicity on the magnetic field lines. Two approaches to generating helical field lines are realised by the Tokamak and Stellarator fusion devices.

Tokamak devices, a group to which ASDEX Upgrade belongs, produce this helicity by inducing a toroidal current in the plasma using a transformer located at the centre of the torus. This current produces a poloidal magnetic field, which modifies the existing toroidal field to create helical field lines, see fig 1.2.

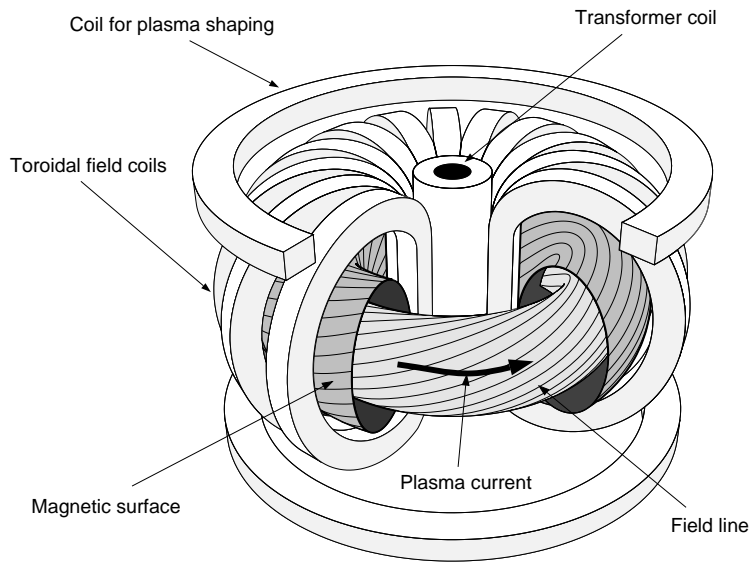


Figure 1.2: The Tokamak.

Stellarator devices use specially shaped magnetic coils to directly create the helical field lines without the need for a plasma current. However, this is done at the cost of geometric simplicity, as assumptions of toroidal symmetry are no longer valid in this configuration.

Magnetohydrodynamic (MHD) instabilities, discussed in more detail in chapter 2, are one of the major limiting factors for achieving high core temperatures. Magnetic islands, formed by these instabilities, allow easy interaction between hot central plasma and cooler plasma further outside the core. The resulting flattening of the temperature profile results in a net drop in the core temperature, see fig 1.3.

In addition to achieving high ion temperatures and densities the energy must be confined for a sufficient time, τ_E , if thermonuclear conditions are to be achieved where,

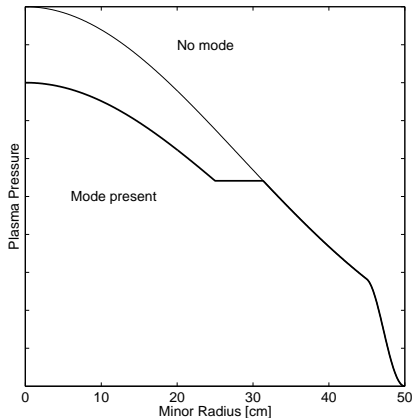


Figure 1.3: Magnetic islands limit the core plasma pressure due to flattening of the temperature profile.

of plasma turbulence, which is not yet quantitatively understood. Empirical representations have been developed to describe the behaviour of τ_E . However, no single empirical scaling is sufficient to describe τ_E under all tokamak operation regimes. Four distinct regimes have been identified, each characterised by a different empirical representation of τ_E : Ohmically heated plasmas, L-mode, H-mode, and improved H-mode.

The ohmically heated regime refers to plasmas heated solely by ohmic heating [1]. L-mode and H-mode regimes are achieved through additional heating using beams of high energy neutral particles or radio frequency heating. The L or low-mode refers to those discharges which, despite the additional heating, fail to show a substantial increase in stored energy. For all discharge configurations the confinement time is degraded by additional heating [1]. H or high-mode discharges show an improved response to heating power in terms of stored energy (with respect to L mode) due to the abrupt appearance of an edge transport barrier [2]. The improved H-mode scenario refers to a subset of H-mode discharges which simultaneously achieve an improved confinement and normalised plasma pressure. These discharges are characterised by a hollow or flattened central current profile, $j(r)$, [3]. It has been conceived that magneto hydrodynamic (MHD) instabilities play a role

$$\tau_E \equiv \frac{\text{plasma stored energy}}{\text{heat loss rate}} \quad (1.5)$$

The ignition threshold for peak ion density, \hat{n} , ion temperature, \hat{T} , and the energy confinement time, τ_E , can be approximated by,

$$\hat{n}\tau_E\hat{T} > 5 \times 10^{21} \text{ s keV m}^{-3} \quad (1.6)$$

The values of τ_E observed in tokamak experiments are much lower than those predicted by neoclassical theory [1]. This behaviour is due to the effect

in establishing this type of current profile. The improved H-mode scenario is of particular interest because its characteristic high confinement makes it a potential advanced operating scenario for the planned ITER experiment. The improved H-mode scenario is discussed in more detail in chapter 2.4. Figure 1.4 shows an example of an improved H-mode discharge. Here it can be seen that subtle changes in the current profile have a large impact on the performance.

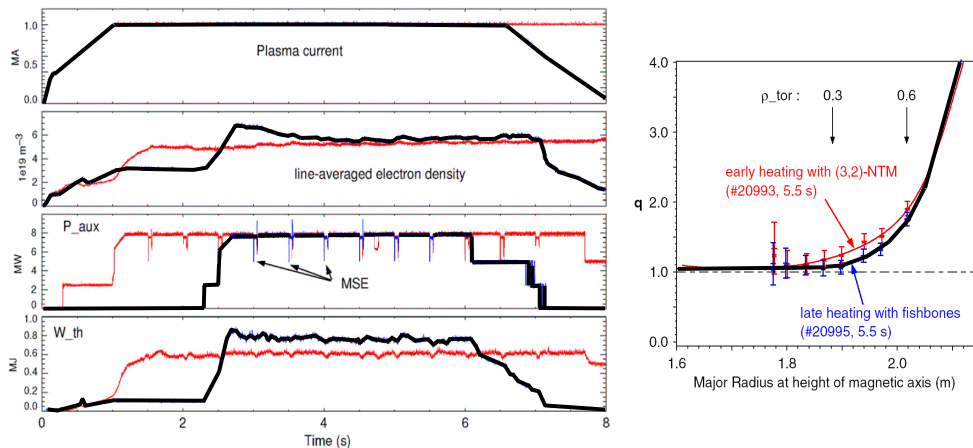


Figure 1.4: Subtle changes in the current profile have a large impact on the discharge performance. Here two discharges are shown which have the same plasma current (left top), and heating power (left 3rd), but with slightly different current profiles (right). The current profile in #20995 is noticeably flatter than for #20993. We observe that #20995 achieves a greater stored energy than #20993 (left 4th). (Figure courtesy of J. Stober [3])

The goal of this thesis is to study, characterise and record MHD events in the improved H-mode scenario, using a variety of plasma diagnostics, discussed in 3. To aid in this analysis a new tool has been implemented for ASDEX Upgrade, Soft X-ray Tomography. This tool combines data from several Soft X-ray (SXR) cameras to reconstruct a poloidal cross section of emissivity for a given time point and frequency range. This allows us to locate and identify MHD instabilities, as well as observe the time evolution of these events. More details about the implementation of this tomography program are given in chapter 4.

The results of this analysis have been compiled into a database of MHD events, that will be used to answer the following questions: under what conditions do the various types of MHD instabilities appear, what is their

effect on confinement, and what role, if any, do they play in establishing the current profile in the improved H-mode scenario? The MHD instability database is discussed in chapter 5. These questions and the conclusions drawn from the MHD instability study are discussed in detail in chapters 6 through 8. Finally, a summary and discussion of these results is given in chapter 9.

Chapter 2

Basics

This chapter aims to characterise the key magneto hydrodynamic (MHD) instabilities studied in this thesis. This is followed by an introduction to the improved H-mode operating scenario in which these MHD instabilities have been observed. Finally, there will be an overview of the main plasma diagnostics used to make these observations.

2.1 Magneto Hydrodynamics

The term *magneto hydrodynamic* comes from the single fluid model of a plasma. In this model a hydrogen plasma is treated as a fluid of ions and electrons. This model is best summarised by the following equations. If we assume the plasma to be quasi neutral, $n_e \approx Z_{eff}n_i$, that the displacement current is negligible in the limit, $v \ll c$, we arrive at the following forms of the Maxwell equations,

$$\nabla \times \mathbf{E} = -\frac{\partial \mathbf{B}}{\partial t} \quad (2.1)$$

$$\nabla \times \mathbf{B} = \mu_0 \mathbf{j}, \quad v \ll c \quad (2.2)$$

$$\nabla \cdot \mathbf{B} = 0 \quad (2.3)$$

$$\nabla \cdot \mathbf{E} = 0 \quad (2.4)$$

We define the plasma mass density, ρ , the velocity of the centre of mass, \mathbf{v} , and the plasma current density, \mathbf{j} ,

$$\boldsymbol{\rho} = m_i n_i + m_e n_e \quad (2.5)$$

$$\approx m_i n, \text{ assuming } m_i \gg m_e \quad (2.6)$$

$$\boldsymbol{v} = \frac{1}{\rho} (m_i n_i \boldsymbol{u}_i + m_e n_e \boldsymbol{u}_e) \quad (2.7)$$

$$\approx \boldsymbol{u}_i \quad (2.8)$$

$$\boldsymbol{j} = en(\boldsymbol{u}_i - \boldsymbol{u}_e) \quad (2.9)$$

We assume the following forms of the hydrodynamic equation for continuity and the adiabatic equation,

$$\frac{\partial \rho}{\partial t} + \nabla \cdot \rho \boldsymbol{v} = 0 \quad (2.10)$$

$$\left(\frac{\partial}{\partial t} + \boldsymbol{v} \cdot \nabla \right) \frac{p}{\rho^\gamma} = 0 \quad (2.11)$$

where p is the pressure and γ is the adiabatic exponent. These equations are then coupled via the Ohmic law and Newtonian law of momentum conservation to form,

$$\eta \boldsymbol{j} = \boldsymbol{E} + \boldsymbol{v} \times \boldsymbol{B} \quad (2.12)$$

$$\rho \left(\frac{\partial}{\partial t} + \boldsymbol{v} \cdot \nabla \right) \boldsymbol{v} = -\nabla p + \boldsymbol{j} \times \boldsymbol{B} \quad (2.13)$$

2.2 Plasma Equilibrium

We define a magnetic surface as a contour of constant poloidal flux, ψ , i.e. for which $\boldsymbol{B} \cdot \nabla \psi = 0$. These surfaces form nested tori within the plasma. Figure 2.1 shows an illustration of such tori for a typical discharge on ASDEX Upgrade. If we neglect flow, $\boldsymbol{v} = 0$,¹ and assume the plasma to be in equilibrium, $\frac{\partial}{\partial t} = 0$, then we can use the equation of motion (2.13) to find the isotropic pressure,

$$\nabla p = \boldsymbol{j} \times \boldsymbol{B} \quad (2.14)$$

¹This is a good approximation so long as $\boldsymbol{v} \ll c_{\text{sound}}$.

This equation has two important consequences, namely, $\mathbf{B} \cdot \nabla p = \mathbf{B} \cdot (\mathbf{j} \times \mathbf{B}) = 0$ and $\mathbf{j} \cdot \nabla p = \mathbf{j} \cdot (\mathbf{j} \times \mathbf{B}) = 0$. Or in other words, pressure is a constant within any given magnetic surface and the current vector \mathbf{j} always lies within the magnetic surface.

If we consider flux surfaces with decreasing mean minor radius, r , to the limit $r \rightarrow 0$, we converge to a point called the magnetic axis. Flux surfaces of increasing minor radius make a transition from closed loops within the vessel (in a poloidal projection) to loops which intersect the vessel wall, or "open" loops. The last closed flux surface, LCFS, before this transition can be either in a so called "limiter" or "separatrix" configuration. In the limiter case, the LCFS makes physical contact with an in-vessel component, while the separatrix is formed using magnetic coils to generate an x-point, i.e. a point where the poloidal magnetic field drops to zero, pictured in figure 2.1. The separatrix has the effect of removing particles from the vacuum vessel into the divertor region. The divertor configuration plays an important role in fusion research as it limits the influx of impurities into the plasma. These impurities not only potentially dilute the fuel but also cause increased radiated losses. The nested flux surfaces discussed above form the basis for two convenient coordinate systems used often in this thesis. The first, $(\rho_{\text{pol}}, \theta, \varphi)$, is based on the poloidal flux, ψ ,

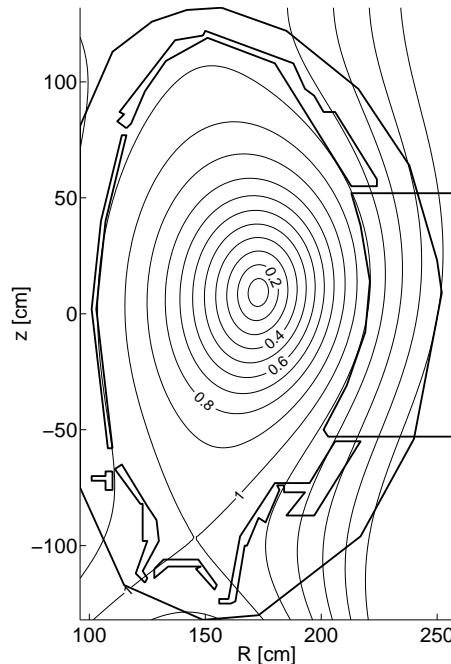


Figure 2.1: A typical poloidal cross section on ASDEX Upgrade showing contours of ρ_{pol} .

$$\rho_{\text{pol}} = \sqrt{\frac{\psi - \psi_0}{\psi_{\text{sep}} - \psi_0}} \quad (2.15)$$

where $\psi_0, \psi_{\text{sep}}$ represent the poloidal flux through the magnetic axis and separatrix respectively. ρ_{pol} forms the analogue of the minor radius in a toroidal coordinate system. θ and φ are the poloidal and toroidal angles.

This is the most commonly used coordinate system on ASDEX Upgrade as it is defined both inside and outside the LCFS. However, the poloidal flux is not a well known quantity close to the magnetic axis. The consequence of which is that the ρ_{pol} coordinate is very sensitive to the equilibrium reconstruction. For some applications this renders it a poor basis for comparison.

A similar coordinate system based on the toroidal magnetic flux exists, $(\rho_{\text{tor}}, \theta, \varphi)$. Unlike ψ , the toroidal flux, Φ , is a well defined quantity from the magnetic axis to the separatrix. Outside of the separatrix ρ_{tor} is not defined.

$$\rho_{\text{tor}} = \sqrt{\frac{\Phi - \Phi_0}{\Phi_{\text{sep}} - \Phi_0}} \quad (2.16)$$

Where Φ_0 and Φ_{sep} represent the toroidal flux through the magnetic axis and separatrix respectively. Both ρ_{tor} and ρ_{pol} range from zero at the magnetic axis to 1 at the LCFS. At this point it is also convenient to introduce a 3rd flux surface quantity called the safety factor, q . This quantity is named due to its role in quantifying the plasma stability against disruption. Generally a higher value of q close to the separatrix means improved stability. The value of q on a given magnetic surface is a measure of the field line helicity. In other words, how many toroidal windings, N_{tor} , and poloidal windings, N_{pol} , the field line undergoes before joining up on itself.

$$q = \frac{N_{\text{tor}}}{N_{\text{pol}}} = \frac{d\phi}{d\psi} = \frac{r B_\phi}{R B_\theta} \quad (2.17)$$

$$\lim_{\rho_{\text{pol}} \rightarrow 1} q \rightarrow \infty \quad (2.18)$$

The above limit for q at $\rho_{\text{pol}} = 1$ is true only for separatrix configurations, and is due to the x -point, where the poloidal magnetic field drops to zero. A magnetic surface for which q is equal to the ratio of two integers is known as a rational surface.

Radial profiles of $q(\rho_{\text{tor}})$ are important for many discussions in later chapters. It is possible to make a crude characterisation of a given q profile using two quantities: q_0 , the value of the q profile at the magnetic axis, and q_{95} , the value of the q flux surface bounding 95% of the toroidal flux. Note, the choice of 95% is arbitrary. It is simply necessary to choose a value of q within the separatrix due to the limit $q_{\text{sep}} \rightarrow \infty$.

Accurate reconstruction of the safety factor is difficult, especially close to the magnetic axis. In this thesis q profiles have been reconstructed using the CLISTE equilibrium code. This code is discussed more in chapter 2.2.1. Figure 2.2 shows an example of an equilibrium reconstruction on ASDEX Upgrade. The q surfaces shown here correspond to integer values of N_{pol} and N_{tor} . The normalised plasma pressure, β , is a combination of the plasma pressure and magnetic field pressure.

$$\beta_{\text{tor}} = p \left(\frac{B_{\text{tor}}^2}{2\mu_0} \right)^{-1} \quad (2.19)$$

Ideal MHD optimisation studies into the maximum achievable β_{tor} have found the following relation [1],

$$\beta_{\text{tor}}^{\text{max}} = c \frac{I_P}{aB} \quad (2.20)$$

where I_P is the plasma current (in MA), and a is the minor plasma radius. The constant, c , depends on the plasma configuration, e.g. $c = 2.8$ for a circular plasma, or $c \approx 3.5$ for an elliptical configuration. This allows us to define a new quantity, β_N , which is a measure of how close the achieved β_{tor} is to the theoretical limit,

$$\beta_N = \beta_{\text{tor}} \left(\frac{I_P}{aB} \right)^{-1} \quad (2.21)$$

For example, a $\beta_N = 3.0$ in an elliptical configuration tells us that we are operating at approximately 85% of the theoretical limit. In order to discuss the stored energy in the plasma it is necessary to define the energy confinement. A normalised quantity called the H factor is often used when discussing the plasma confinement. It is based on the confinement time, τ_E , and a normalising quantity appropriate for the type of plasma discharge being observed. For this thesis the $H_{98(y,2)}$ factor will be used [5].

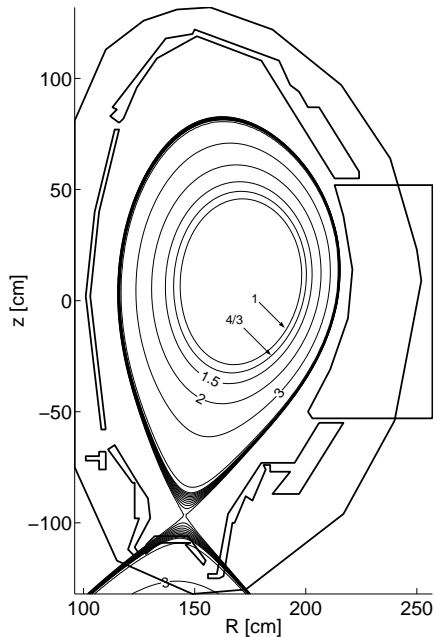


Figure 2.2: A poloidal cross section of ASDEX Upgrade, showing the reconstructed q surfaces. This reconstruction was done by the CLISTE equilibrium code.

It is given by,

$$\tau_{E\ 98(y,2)} = CI_P^{\alpha_I} B_\phi^{\alpha_B} P_{\text{heat}}^{\alpha_P} \left(\frac{n_e}{10^{20}} \right)^{\alpha_n} A^{\alpha_A} R^{\alpha_R} \epsilon^{\alpha_\epsilon} \kappa^{\alpha_\kappa} \quad (2.22)$$

$$H_{98(y,2)} = \frac{\tau_E}{\tau_{E\ 98(y,2)}} \quad (2.23)$$

C	α_I	α_B	α_P	α_n	α_A	α_R	α_ϵ	α_κ
0.0365	0.97	0.08	-0.63	0.41	0.2	1.93	0.23	0.67

where C is a constant, I is the plasma current [MA], B the magnetic field [T], n the plasma density [m^{-3}], A the ion mass number, R the major plasma radius, ϵ the inverse aspect ratio, and κ the plasma elongation. The α_* terms are fitted scaling factors. $H_{98(y,2)} = 1$ is the goal for ITER, while $H_{98(y,2)} > 1$ represents an improved scenario.

2.2.1 The CLISTE Equilibrium Code

For axially symmetric configurations the fluid description of macroscopic plasma behaviour in equilibrium can be reduced to a single partial differential equation [6], commonly called the Grad-Shafranov equation (2.24). This equation describes the plasma equilibrium in terms of two arbitrary flux functions, $p(\psi)$, and $F(\psi)$,

$$\begin{aligned} - \left(\frac{\partial^2 \psi}{\partial R^2} - \frac{1}{R} \frac{\partial \psi}{\partial R} + \frac{\partial^2 \psi}{\partial z^2} \right) &= \mu_0 R^2 p'(\psi) + FF'(\psi) \\ &\equiv \mu_0 R j_\phi \end{aligned} \quad (2.24)$$

Note that $p'(\psi)$ and $FF'(\psi)$ define the toroidal current density profile, j_ϕ . The CLISTE² equilibrium code solves this partial differential equation for $\psi(R, z)$ by specifying the functions $p(\psi)$, $F(\psi)$ along with a set of boundary conditions and externally imposed constraints on ψ . In practice $p'(\psi)$ and $FF'(\psi)$ are constructed by a linear superposition of basis functions. The magnitude of each basis function forms a set of free parameters which can be varied to find the best fit to a set of experimental measurements. The CLISTE equilibrium code uses a family of solutions, $p(\psi) \propto \psi$, and $F^2(\psi) \propto \psi^2 + \gamma\psi + F_0$ due to their ability to better parameterise experimental current profiles [7].

The experimental measurements used in this thesis include the external magnetic data, pitch angle measurements of the magnetic field lines from

²CompLete Interpretive Suite for Tokamak Equilibria.

the Motional Stark Effect (MSE) diagnostic, kinetic profiles, and the parallel/perpendicular fast fuel ion pressure profiles calculated by the FAFNER code [8]. The free parameters are varied such that the penalty or *cost function* (the square modulus of the vector of weighted differences between the experimental measurements and those predicted by the equilibrium code) is minimised.

Figure 2.3 shows three fitted q profiles with increasing experimental constraints. The location of the (3, 2) rational surface is indicated as determined by Soft X-ray and Electron Cyclotron measurements of a (3, 2) instability present in this time window.

The first q profile, labelled **MAG**, shows a CLISTE reconstruction constrained only by the external magnetics. The mismatch between this equilibrium and the location of the (3, 2) mode is significant.

The second curve, **MAG, KIN, FAF, MSE**, has been further constrained by fitted kinetic profiles, T_e , T_i , n_e , fast particle simulations (performed by the FAFNER Monte Carlo code, see chapter 2.5.1), and pitch angle measurements provided by the MSE diagnostic. The mismatch between this reconstruction and the mode position measurements is reduced. All equilibria used in this thesis were reconstructed using the external magnetic, kinetic, and fast particle information. The MSE diagnostic was only available for a subset of the discharges studied.

The third q profile, **MAG, KIN, FAF, MSE, MHD**, has been reconstructed using the location of the (3, 2) mode as an additional constraint. While mode positions can clearly improve the accuracy of the equilibrium, they will not be used in this thesis.

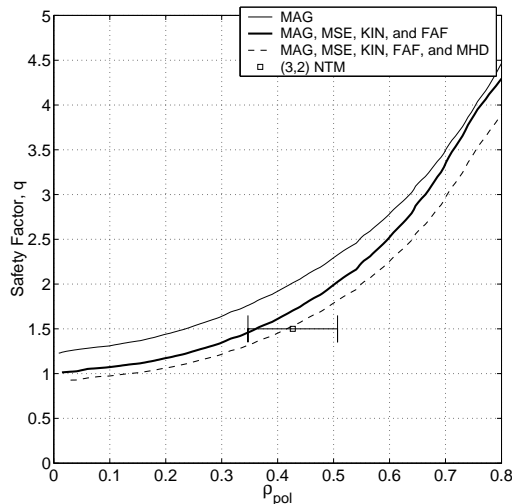


Figure 2.3: This figure shows the reconstructed q profile using increasing experimental constraint. The uppermost curve has been constrained only by the external magnetics. The solid dark curve beneath it has been further constrained by the plasma kinetic profiles; fast particle simulations, and MSE measurements. The dashed curve uses the location of the (indicated) (3, 2) mode as an additional constraint.

Additional Functionality

In addition to functioning as an equilibrium code, CLISTE can independently calculate the bootstrap and ohmic current densities using kinetic profile information [32]. In this way it mimics some of the functionality of a transport code. The bootstrap current $\langle \mathbf{j} \cdot \mathbf{B} \rangle_{boot}$ is calculated using the Sauter-Angioni-Lin-Liu model [33], while the induced ohmic current $\langle \mathbf{j}_{\Omega, \parallel} \rangle$ is calculated from the equilibrium solution above,

$$\langle \mathbf{j}_{\Omega, \parallel} \rangle = \sigma \langle \mathbf{E} \cdot \mathbf{B} \rangle = \sigma \left[-\frac{F}{2\pi} \left\langle \frac{\partial \psi}{\partial t} \frac{1}{R^2} \right\rangle + \oint E_{\theta} d\ell \right] \quad (2.25)$$

2.3 MHD Instabilities

Magneto hydrodynamic (MHD) instabilities are one of the major limiting factors to achieving high confinement. These instabilities can be separated into two categories: *ideal*, and *resistive*.

2.3.1 Ideal Instabilities

Ideal instabilities are modes which would occur even if the plasma were perfectly conducting. We can determine the plasma stability against a given ideal instability by calculating the change in potential energy, W , resulting from a displacement function $\boldsymbol{\xi}(\mathbf{x})$, from the volume integral below,

$$\delta W = -\frac{1}{2} \int \boldsymbol{\xi} \cdot \mathbf{F} dV \quad (2.26)$$

where $\mathbf{F}(\mathbf{x})$ is the force arising from the displacement. If the change in potential $\delta W < 0$ then the plasma is unstable against this mode. Ideal instabilities grow on the Alfvén timescale, $\tau_{\text{Alfvén}}$, defined below,

$$\tau_{\text{Alfvén}} = \frac{R}{B/\sqrt{A\mu_0 m_p n}} \quad (2.27)$$

where R is the major radius, B is the magnetic field, A and m_p are the atomic number and proton mass, and n is the density. Typical values for $\tau_{\text{Alfvén}}$ on ASDEX Upgrade are between $1 \rightarrow 10 \mu\text{s}$.

2.3.2 Resistive Instabilities

In the ideal MHD equations the plasma resistivity is taken to be zero. In this scenario there can be no local perturbed electric field, \mathbf{E}_1 in the direction of \mathbf{B}_0 . When the resistivity is non-zero then we can describe a perturbed magnetic field, \mathbf{B}_1 ,

$$\frac{\partial \mathbf{B}_1}{\partial t} = \nabla \times \left(\frac{d\xi}{dt} \times \mathbf{B} \right) - \nabla \times \frac{1}{\sigma} \mathbf{j}_1 \quad (2.28)$$

where σ and \mathbf{j}_1 represent the conductivity and local current perturbation respectively. We can generate an equation for the diffusion of the magnetic field, $\Delta \mathbf{B}$,

$$\Delta \mathbf{B} = -\nabla \times (\nabla \times \mathbf{B}) \quad (2.29)$$

$$= -\nabla \times (\mu_0 \mathbf{j}) \quad (2.30)$$

taking σ to be
constant in space

$$= -\mu_0 \sigma \nabla \times \mathbf{E} \quad (2.31)$$

$$= \mu_0 \sigma \frac{\partial \mathbf{B}}{\partial t} \quad (2.32)$$

From this we can define a quantity called the resistive MHD time scale, τ_{res} , which considers the diffusion time with respect to the plasma minor radius, a ,

$$\tau_{\text{res}} = \mu_0 \sigma a^2 \quad (2.33)$$

which is typically of the order of $1 \rightarrow 10$ s on ASDEX Upgrade, compared to the $1 \rightarrow 10 \mu\text{s}$ associated with the Alfvén time scale for ideal MHD instabilities. In addition to a longer time scale, the resistive MHD equations allow for the breaking and reconnection of magnetic field lines. Which in turn can lead to the formation of magnetic islands in the plasma, see fig 2.4. This breaking, or "tearing" of the magnetic field lines gives rise to the name of a particular type of MHD instability studied in this thesis, Neo-classical Tearing Modes (NTM).

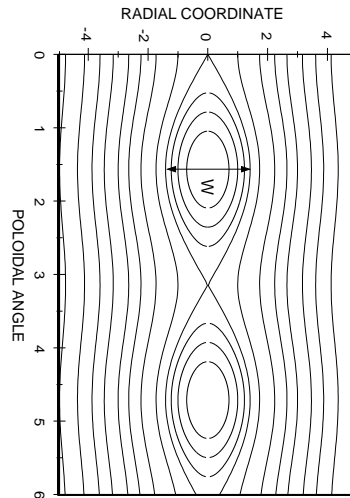


Figure 2.4: Resistivity allows for the breaking and reconnection of magnetic field lines, which can result in the formation of a magnetic island. The X point is the islands last closed flux surface, and the O point is the point of maximum field line separation.

2.3.3 Neo-classical Tearing Modes

Neo-classical Tearing Modes (NTM) are resistive MHD instabilities that form magnetic islands in the plasma. The island width, w , is defined as the radial extent of the islands LCFS at the island O-point, see figure 2.4. NTM are labelled according to their poloidal and toroidal mode numbers, m , n , respectively. For example an NTM with $m = 3$, $n = 2$ would be called a (3, 2) NTM. These modes can have a strong impact on the plasma energy confinement as the magnetic island allows for relatively high transport between hot central plasma and cooler plasma outside the NTM rational surface. This leads to a flattening of the local temperature profile and to a net drop in the core plasma temperature, see figure 1.3. The extent to which a given NTM will effect the plasma confinement is predicted by the Belt Model [9, 10]. This model will be tested against improved H-mode observations in chapter 7.

The growth of an NTM is governed by the Rutherford equation, shown below [11]. This equation will be used to discuss the onset of NTM instabilities observed in the improved H-mode scenario in chapter 6.1. What follows is an explanation of the terms and quantities used in this thesis, as well as the physical meaning behind each term,

$$\frac{\tau_{res}}{r_s} \frac{dw}{dt} = r_s \Delta' + a_0 [\Delta_{bs} + \Delta_{GGJ}] \quad (2.34)$$

τ_{res} is the resistive time scale from equation (2.33), r_s is the minor radius of the NTM resonant surface, and dw/dt is the island growth rate. a_0 has been found to be $a_0 = 0.85 \pm 0.15$ [12]. For $dw/dt \leq 0$ the plasma is stable against this instability. Two of the terms on the right hand side of equation (2.34) are stabilising in that they are typically negative: Δ' and Δ_{GGJ} . The term Δ' represents the plasma stability against the tearing mode. It describes the free energy available in plasma current density to drive the tearing mode. There are two forms of Δ' used in this thesis. The first is the vacuum approximation,

$$\Delta' \approx -m \quad (2.35)$$

where m is the poloidal mode number of the NTM. This term will be used to fit NTM onset observations in chapter 6.1 to test the validity of this approximation. While this term can be potentially used for NTM onset studies, it cannot be used to study the NTM island saturation, as Δ' has

been found to depend on the island width in the non-linear stage of island growth. The second expression for Δ' has been fitted for a typical (3, 2) NTM in numerical simulations [13]. As yet no such fitting exists for other (m, n) combinations,

$$\Delta' = -(1.97 + 45.5 \frac{w}{a}) \quad (2.36)$$

This form of Δ' will be used in chapter 6.1 to study the initial versus saturated island sizes of (3, 2) NTMs. The second generally stabilising term, Δ_{GGJ} , comes about due to the effects of curvature on the evolution of magnetic islands, [14]. A tearing mode island in a toroidal plasma with finite plasma pressure bends the field lines in such a way as to increase the magnetic energy. This additional energy requirement has the effect of increasing the plasma stability against the tearing mode.

$$\Delta_{GGJ} = 6.35 r_s \frac{\mu_0 D_R}{\sqrt{w^2 + 0.65 w_d^2}} \quad (2.37)$$

The stabilising effect comes from the negative sign of the resistive interchange parameter, D_R . The threshold temperature width, w_d , comes into play when the effects of parallel/perpendicular heat diffusion and curvature are considered. In this thesis the following forms of D_R and w_d were used,

$$D_R = \frac{-(q^2 - 1) L_q^2 r_s \beta_p}{q^2 L_p R_0^2 \mu_0} \quad (2.38)$$

$$w_d = 5.1 \sqrt{\frac{R_0 L_q q}{m}} \left(\frac{\chi_{GB}}{\chi_{par}} \right)^{1/4} \quad (2.39)$$

$$\chi_{par} = \frac{26.4 \pi^{3/4} T_e^{5/2} \epsilon_0^2}{n_e \sqrt{2 m_e} e_\ell^{3/2} \ln(\Lambda)} \sqrt{1 + \left(\frac{1137.6 n w}{4 \pi R_0 L_q} \right)^2} \quad (2.40)$$

$$\chi_{GB} = 3.25 \frac{T_e}{1000} \frac{3 \sqrt{A}}{2 B_{tor}^2 a Z^2} \quad (2.41)$$

where χ_{GB}, χ_{par} , represent the perpendicular gyro Bohm and the parallel heat conductivities respectively. Equation (2.40) assumes we are at the so called "heat flux limit", where the electron mean free path is long compared to the temperature gradient length [15]. L_p and L_q represent the pressure and q -profile scale lengths. β_p is the local poloidal β , see equation (2.19). The driving term for NTM growth, Δ_{bs} , comes from the bootstrap current,

j_{bs} . Equation (2.43) shows that this current is proportional to the inverse of the corrected pressure scale length, L_{p*} ,

$$\Delta_{bs} = \frac{6.34}{2} r_s \mu_0 L_q \frac{j_{bs}}{B_{pol}} \left(\frac{w}{w^2 + w_d^2} + \frac{w}{w^2 + 28w_b^2} \right) \quad (2.42)$$

$$= \frac{6.34}{2} r_s \frac{L_q}{L_{p*}} \sqrt{\varepsilon} \beta_p \left(\frac{w}{w^2 + w_d^2} + \frac{w}{w^2 + 28w_b^2} \right) \quad (2.43)$$

where ε is the plasma inverse aspect ratio and w_b is the banana orbit width. An explanation of the bootstrap current and banana orbitals follows

in chapter 2.5. The banana orbit width at the magnetic midplane, w_b , is defined as,

$$w_b = \frac{2}{e_l} \frac{A m_p T_i}{B_{pol}} \sqrt{\varepsilon} \quad (2.44)$$

where e_l , A , and m_p represent the charge of an electron, the atomic number, and proton mass respectively. T_i is the local ion temperature. It is important to note the difference between the pressure scale length, L_p , and the corrected pressure scale length, L_{p*} ,

$$\frac{1}{L_{p*}} = \frac{C_T}{L_T} + \frac{C_n}{L_n} \quad (2.45)$$

here the contributions to the pressure scale length are weighted by temperature, $C_T = 0.6$, and density, $C_n = 2.27$. As the driving term, Δ_{bs} , depends strongly on the pressure gradient, NTMs are grouped into a subset

of MHD instabilities known as pressure driven instabilities. Figure 2.5 shows dw/dt as a function of w for different values of β_p . It can be seen that for $\beta_p < \beta_{p,crit.}$, $dw/dt < 0$, i.e. the plasma is stable against this NTM. For $\beta_p \geq \beta_{p,crit.}$ the NTM can grow if a sufficiently large seed island is present with $w_{seed} \geq w_{min}$.

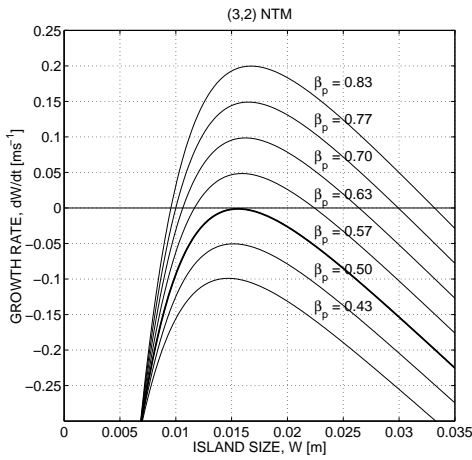


Figure 2.5: The Rutherford equation (2.34) gives us dw/dt as a function of w . Several contours are shown for increasing β_p . For $\beta_p < \beta_{p,crit.}$, $dw/dt < 0$, i.e. the plasma is stable against this NTM. For $\beta_p \geq \beta_{p,crit.}$ the NTM can grow if a sufficiently large seed island is present with $w_{seed} \geq w_{min}$. The solid line shows the marginal stability limit.

We will now define two types of NTM onset. The first, precursor-triggered NTM (PNTM) onset, occurs when an event such as sawtooth or fishbone reconnection creates seed islands $w_{seed} \geq w_{min}$.

Under these conditions dw/dt becomes positive and the NTM will grow from size $w_{seed} \rightarrow w_{sat}$. This scenario is the most common in relatively low β discharges such as H and L mode.

The second type onset is called spontaneous NTM (SNTM) onset as there no visible precursor event appears to trigger the NTM. SNTMs grow from much smaller seed island sizes than PNTMs, close to the sensitivity limit of the Mirnov coil diagnostic, see figure 2.6.

The initial phase appears to have a rapid exponential growth character, rising sharply from the noise, which then makes a transition to the NTM linear resistive growth rate. The mechanism behind the initial phase is not understood. As this type of NTM onset is observed more regularly in improved H-mode discharges than in other scenarios it is possibly due to an ideal MHD mode destabilised at high β and/or low magnetic shear. This would be similar in character to the ideal infernal mode discussed in the next section on the Frequently Interrupted Regime. In figure 2.6 we observe what appear to be short time scale bursts with rapid growth rates and decay times, which increase in amplitude until an apparent threshold

is reached and the NTM begins to grow. Note that we are very close to the sensitivity limit of the Mirnov diagnostic and these features have a low signal to noise ratio. The transition from the ideal to resistive growth character oc-

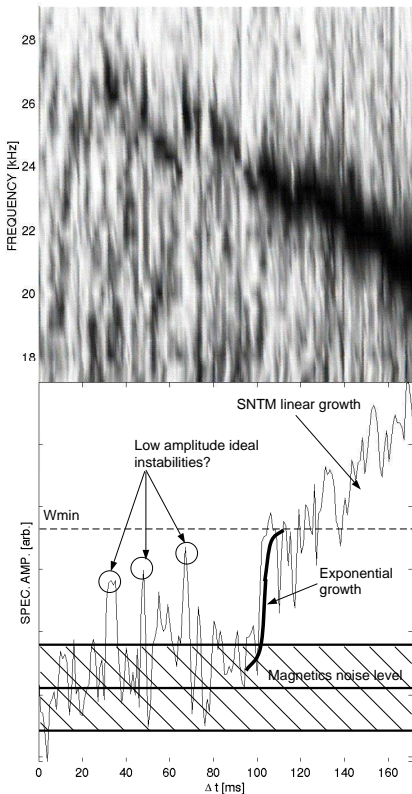


Figure 2.6: Spontaneous onset NTMs (SNTMs) are a characteristic feature of the improved H-mode scenario. Here we see a Mirnov coil spectrogram (top) and spectral amplitude plot (bottom) of an SNTM. There appears to be an initial exponential growth phase which makes a transition to linear resistive growth.

curs when $w_{min} \approx w_{seed}$. We require high β_p to ensure w_{min} is small enough to make the transition, and subsequent SNTM growth, possible. One of the goals of this thesis is to estimate the size of w_{seed} for SNTM onsets. This topic is developed further in chapters 5.2 and 6.1.

2.3.4 Frequently Interrupted Regime NTM

It has been observed that NTMs which occur in plasmas with high values of β_N sometimes have less of a detrimental impact on the energy confinement than NTMs which occur at lower β_N . Such NTMs make a transition into what is known as the Frequently Interrupted Regime for NTM (FIR-NTM). In this regime the NTM island size is sharply reduced through stochastic interaction with an ideal mode located on a nearby rational surface. As the NTM growth time is much longer than the time between two such subsequent interactions the NTMs are unable to reach their saturated amplitude. This results in a time averaged reduction in NTM amplitude, mitigating their impact of the energy confinement from roughly 30% to less than a 10% loss in confinement (for a (3, 2) NTM).

The observed losses in NTM amplitude have been explained by non-linear three wave coupling between the (m, n) NTM and $(1, 1)$, $(m+1, n+1)$ activity [16]. Figure 2.7 shows a time series of normalised NTM amplitude along with a spectrogram highlighting the (m, n) NTM, and the $(m+1, n+1)$, $(1, 1)$ mode. Note the strong drop in NTM amplitude coinciding with the appearance (and subsequent phase locking) of the $(m+1, n+1)$ and $(1, 1)$ instabilities. Smaller "crashes" are visible in the NTM amplitude which can be attributed to Edge Localised Modes (ELMs). Such modes are clearly visible in the H_α signal shown at the bottom of the lower plot.

The ideal $(m+1, n+1)$ mode, henceforth referred to as the "infernial mode",³ becomes destabilised for high values of β_N and low magnetic shear at the $q = m/n$ rational surface. On ASDEX Upgrade a threshold value of $\beta_N \geq 2.3$ has been found [17]. However, it is expected that this threshold will be lower for discharges with a low global magnetic shear.

Weak global magnetic shear is beneficial for confinement as it simultaneously reduces the NTM drive (by limiting the current gradient across its rational surface) [17], while reducing the plasma stability against the $(m+1, n+1)$

³it is called an infernial mode because it is an ideal mode destabilised at low magnetic shear and high pressure gradient across its resonant surface

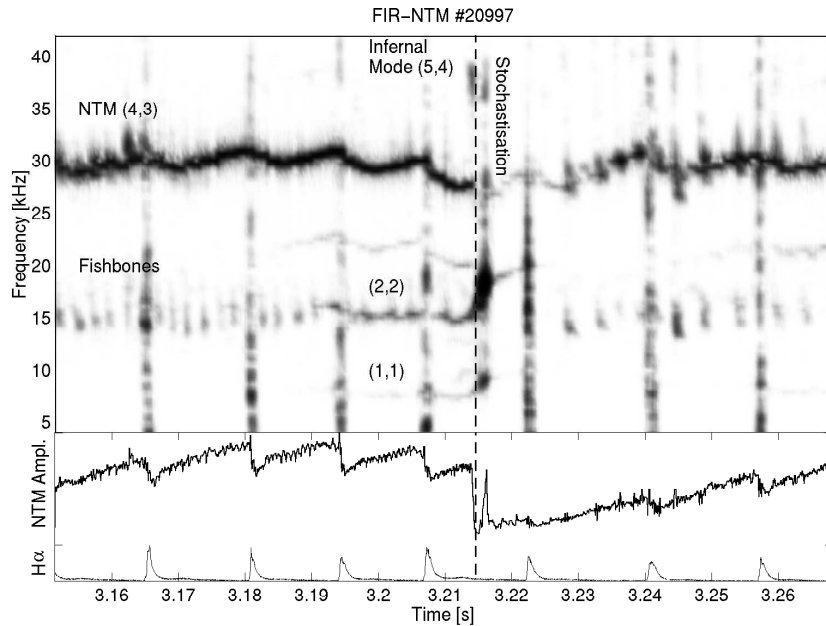


Figure 2.7: Stochastic interaction with an ideal (4,3) infernal mode causes a rapid drop in the observed (3,2) NTM amplitude, shown here as a time series. Note that the other losses in NTM amplitude coincide with a peak in the H_{α} emission. These losses are due to Edge Localised Modes (ELMs) rather than stochastisation.

infernal mode. This in turn makes for an easier transition into the frequently interrupted regime. It is therefore not surprising that low central magnetic shear is a key ingredient of the so called improved H-mode scenario, which is discussed in chapter 2.4.

2.3.5 The Fishbone Instability

The fishbone instability is an ideal instability located on the $q = 1$ surface. Its name was chosen due to its characteristic burst-like structure in the magnetic probe time series. Fast injected beam particles trapped within the $q = 1$ surface can kinetically destabilise the (1, 1) internal kink mode [18, 19].

Beam ions are subsequently scattered through a viscous dissipative process produced by mode-particle resonance which takes the form of an outward drift of those trapped particles in resonance with the mode [20].

The fast trapped particles are ejected first, then the slower fast-particle population is affected. This results in the characteristic downward sweeping

frequency progression shown in figure 2.8. This loss of fast particles reduces beam heating efficiency, thereby limiting the maximum achievable β [18]. Fast particle losses also potentially reduces the heating due to fast alpha particles which is necessary to compensate energy losses in a burning plasma.

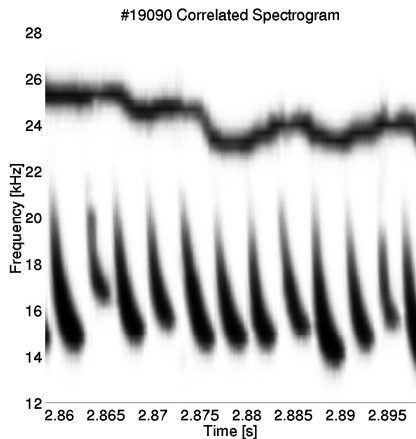


Figure 2.8: The fishbone instability has a characteristic downward sweeping frequency progression, seen clearly here in this Mirnov coil correlated spectrogram.

There is increasing evidence that the fishbone instability plays some role in fixing the central q profile close to unity [21]. In the absence of reconnection, transport codes predict that the minimum q value would decrease throughout the discharge reaching a minimum of $q_0 \simeq 0.8$. It is believed that fishbone and sawtooth reconnection periodically redistributes the central current, preventing the decrease of q_0 below one.

This fixing of the central q profile is essential for maintaining the characteristic flattened improved H-mode q profile, discussed in chapter 2.4. While reconnection due to sawteeth (discussed in the next section) can also redistribute the central current, they are less favourable than fishbones as they are more prone to triggering NTM instabilities [22].

2.3.6 The Sawtooth Instability

In this instability a (1,1) mode grows on the $q = 1$ surface, then a rapid drop in the plasma core temperature is observed, coinciding with a rise in temperature outside of the core, as shown in figure 2.9. As mentioned in the previous section, sawteeth are believed to play some role in limiting the relaxation of the central current profile. Sawtooth reconnection is believed to periodically redistribute the central plasma current, thereby fixing $q_0 \approx 1$. However, sawteeth are less desirable than fishbones as they are more prone to triggering the detrimental NTM instability. They also result in significant energy loss from within $q = 1$. The impact of this energy loss can be small if the intersawtooth period, τ_{saw} , is longer than the recovery time of the kinetic profiles, τ_E . "Fast" sawteeth $\tau_{saw} \leq \tau_E$ will repeatedly flatten the central kinetic profiles faster than they can recover to their maximum amplitude.

”Slow” sawteeth with $\tau_{saw} \gg \tau_E$ will have a time-averaged impact on the core kinetic profiles, but will not limit the maximum achievable β .

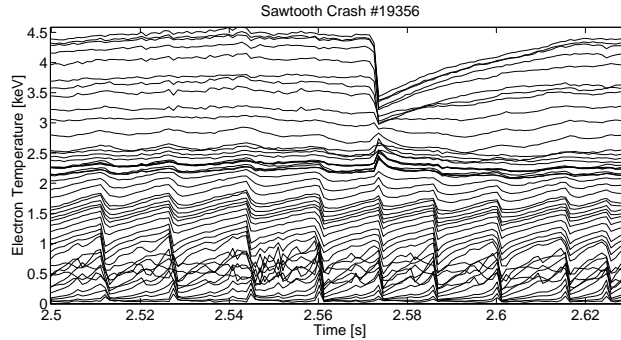


Figure 2.9: This figure shows $T_e(t)$ for each of the Electron Cyclotron Emission (ECE) diagnostic channels. Note that the vertical axis is not only a measure of temperature but also radial position. The channels with high mean T_e are core localised, while the cooler channels are located further out. During a sawtooth crash a rapid decrease is observed in the central channels of the ECE temperature diagnostic, while a corresponding sharp rise is measured in the outer ECE channels. The periodic features visible in the outermost ECE channels are Edge Localised Modes (ELMs).

Full Reconnection

A number of models exist to explain these observations. In one model an ideal kink mode becomes destabilised and results in a displacement of the $q = 1$ surface and the plasma column contained within. In the cylindrical approximation the helical flux can be written as [23],

$$\psi_* = \int_0^r B_*(r') dr' \quad (2.46)$$

$$B_* = B_\theta - rB_\varphi/R \quad (2.47)$$

Figure 2.10 shows the initial profile of $\psi_*(r)$. Here it can be seen that for every radius, r_1 , inside the $q = 1$ surface, r_s , there exists a radius $r_2 > r_s$ with the same value of ψ_* . As the column of plasma is displaced outwards, i.e. $(r_1, r_s) \rightarrow (r'_1, r'_s)$, there will be a point where the displaced r'_1 surface comes into contact with r_2 . At this point the field lines will break and reconnect, leading to an expulsion of the core plasma. This process is illustrated in figure 2.11.

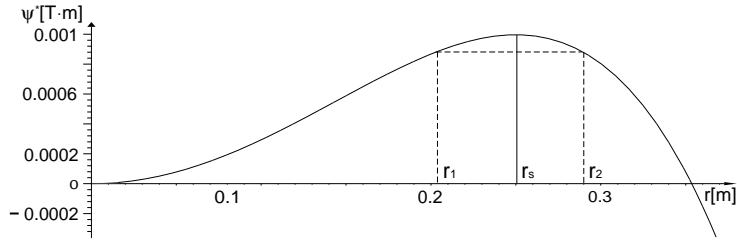


Figure 2.10: The helical flux profile, ψ_* , before a sawtooth crash. For every point r_1 inside r_s there exists a point of equal ψ_* outside r_s .

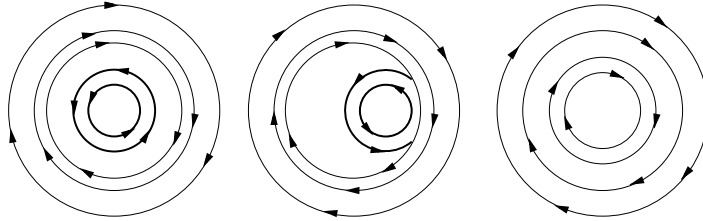


Figure 2.11: When r'_1 comes into contact with r_2 sawtooth reconnection occurs. The hot plasma column inside r_s is ejected into the outer plasma.

In addition to a $q = 1$ surface, the sawtooth instability requires a magnetic shear at the resonant surface in excess of s_{crit} [23],

$$s = \frac{r_s}{q} \frac{dq}{dr} \quad (2.48)$$

$$s \geq s_{crit} = \alpha \sqrt{S^{1/3} \frac{\rho_i}{r_s}} \left(\beta \frac{R^2}{r_s^2} \right)^{7/12} \frac{r_s}{L_n} \left(\frac{r_s}{L_p} \right)^{1/6} \quad (2.49)$$

$$\alpha = \frac{3}{2} c_*^{-7/6} \left[\frac{T_e}{T_i} \frac{1}{1 + \frac{T_e}{T_i}} \right]^{7/12} \quad (2.50)$$

$$\rho_i = \frac{\sqrt{2/e_l A m_p T_i}}{B_{pol}}, \text{ ion gyro radius} \quad (2.51)$$

$$S = \frac{\tau_{res}}{\tau_{Alfvén}}, \text{ Reynold's number} \quad (2.52)$$

where the constant c_* has been found to be of the order of unity for ASDEX Upgrade [24]. It may seem counter intuitive that an ideal onset criterion can be used for a resistive phenomenon like sawtooth reconnection. This is due to the role played by the ideal kink instability: A sufficient kink displacement is required for the reconnection to take place. However,

while this model explains most features observed during a sawtooth crash, it also requires that the central q increases above unity during the sawtooth cycle. This is in contradiction with experimental measurements showing $(1, 1)$ activity continuing after the sawtooth crash, [25, 26], and chapter 6.3.2.

Stochastic Reconnection

Recently, a stochastic sawtooth reconnection model has been proposed to explain the features observed during a sawtooth cycle, without requiring the q_0 to raise above unity [27].

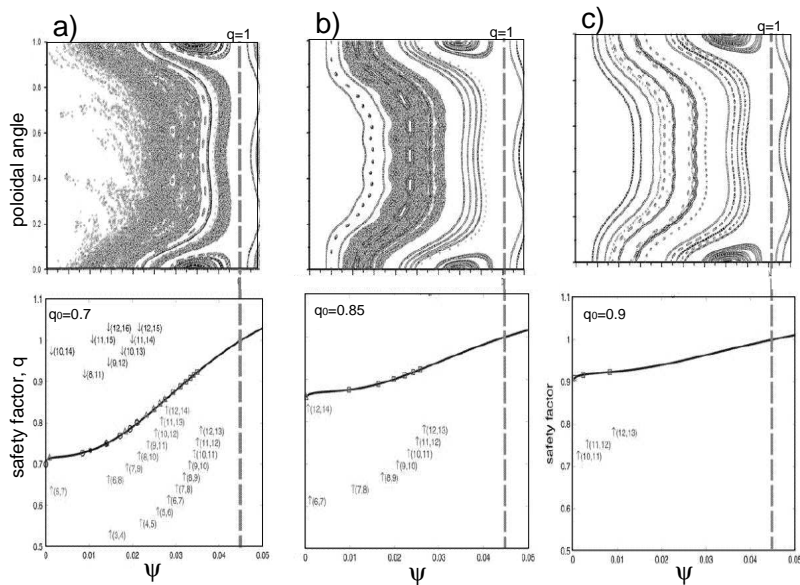


Figure 2.12: This figure demonstrates the stochastic reconnection model. The upper figures show Poincaré plots for the perturbations $(1, 1)$, $(2, 2)$, $(3, 3)$ for different q profiles (lower). The extent of the stochastic region depends strongly on the existence of the indicated low-order rational surfaces. a) $q_0 = 0.7$, the stochastic region is large, extending almost to the $q = 1$ surface. b) $q_0 = 0.8$, the number of low-order rational surfaces is less and the region of stochastisation is noticeably smaller. c) $q_0 = 0.9$, the stochastic region is nearly non-existent.

In this model the displacement eigenfunctions for the $(1, 1)$ kink and its harmonics also excite resonances on rational surfaces within $q = 1$. This displacement leads to a significant perturbation amplitude for low order resonances such as $(5, 7)$, $(6, 8)$, \dots , $(12, 14)$. As these resonances are closely

spaced the perturbations will overlap and form a region of stochasticity [28]. Radial transport in a stochastic region is very high compared to transport in non-stochastic regions. As the $(1, 1)$ displacement increases the stochastic region will overlap and erode the outer closed flux surfaces of the $(1, 1)$ instability. This erosion leads to the observed sharp drop in the mode amplitude. Stochastic erosion at the island x-point will lead to an effective breach of the $q = 1$ surface. This breach greatly increases the transport between the central plasma column and the relatively cool plasma immediately outside of the $q = 1$ surface, which in turn leads to the observed rapid relaxation of the core temperature profile. Figure 2.12 illustrates the stochastic reconnection model of a sawtooth cycle using Poincare plots of magnetic field lines traced through a poloidal cross section. Note that the $q = 1$ surface continues to exist for all phases of the sawtooth cycle.

2.4 The Improved H-Mode Scenario

Under certain conditions a rapid transition to high confinement has been observed, associated with the appearance of an *edge transport barrier* in the plasma.

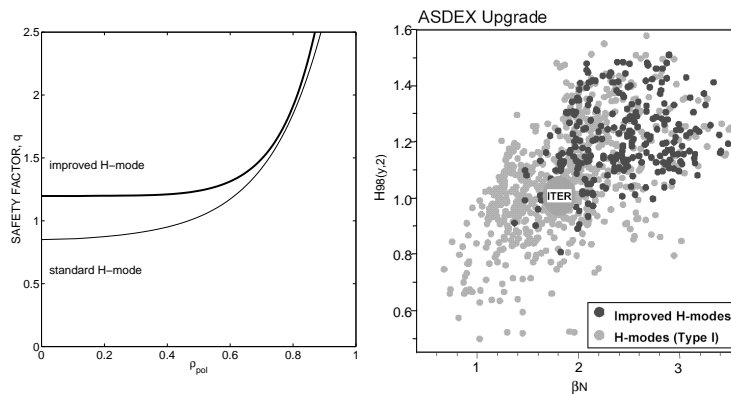


Figure 2.13: The improved H-mode discharges are characterised by a low central magnetic shear and a $q_0 \geq 1$ (left). The scatter plot (right) shows the confinement and stability achieved by the two regimes, as observed on ASDEX Upgrade. The improved H-mode discharges consistently outperform the standard H-mode by simultaneously achieving higher confinement, $H_{98(y,2)}$, and stability, β_N .

Operating scenarios which achieve this transition are called H-Mode scenarios. The transport barrier is thought to be the result of an increase in the edge flow shear, which is in turn expected to have a stabilising effect on turbulence. Improved H-mode discharges have been observed within a range $3.2 < q_{95} < 4.5$ and densities up to 85% of the Greenwald value [29]. Figure 2.13 shows typical q profiles for both the standard and improved H-Modes (left), and a scatter plot of confinement and normalised plasma pressure, β_N (right). The original publication for the latter can be found here [30].

One of the major goals of tokamak fusion experiments is the so called "advanced" tokamak scenario for stationary operation. Stationary operation means that the plasma current is provided entirely by non-inductive current drive. In this scenario an internal transport barrier is triggered by a reversed current profile (see figure 2.14), which acts to limit anomalous transport and results in a steep pressure gradient. This pressure gradient drives a substantial off-axis bootstrap⁴ current, which (combined with additional non-inductive current drive) maintains the reversed current profile. "Hybrid" discharges are seen as an achievable middle-ground between conventional and advanced current profile configurations, see figure 2.14. For this reason the Improved H-mode regime is of particular interest for reactor scale devices as it is seen as a candidate for long pulse hybrid operation [29].

It is believed that the characteristic flat q profile prevents the occurrence of high frequency sawtooth crashes. Although sawteeth are occasionally observed during improved H-mode discharges the inter-sawtooth period is typically long, $\sim 0.5s$. It has been shown that sawteeth of this kind provide less of a limit to the maximum achievable β than high frequency sawteeth. Sawteeth can also serve as the trigger for NTM instabilities, which in turn degrade confinement. Sawteeth can be avoided entirely if the q_0 is held above unity throughout the discharge.

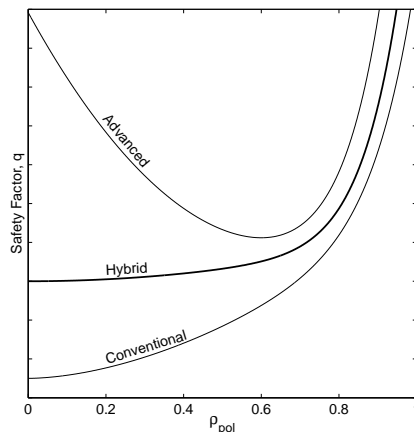


Figure 2.14: Current profiles for the conventional, advanced and hybrid regimes. Hybrid discharges are seen as an achievable middle-ground between conventional and advanced current profile configurations.

⁴The bootstrap current is explained in chapter 2.5.

Improved H-mode discharges are a subset of the H-Mode discharges which simultaneously achieve a higher confinement and stability, $H_{98(y,2)} > 1$, and $\beta_N > 2.5$. This improvement is due, in part, to an increase in pedestal top pressure p^{PED} , which in turn leads to a higher overall plasma pressure and plasma stored energy [4]. The improved H-mode is traditionally achieved by applying early additional heating power during the current ramp-up phase. This early heating increases the electron temperature which in turn increases the current diffusion time, limiting the penetration of the induced loop voltage into the plasma. This results in a flattened, or even hollow current profile. However, an explicit late heating scheme has also been discovered on ASDEX Upgrade [3] throwing into question the effect of early heating on the current ramp-up phase.

As it was mentioned in the two previous sections, it is believed that MHD reconnection phenomena play some role in preventing the relaxation of the central q below $q_0 \approx 1$, thereby maintaining the characteristic flattened q profile throughout the discharge. Other observations suggest that an NTM current drive phenomenon⁵ may aid in establishing the initial current profile [35]. All such interactions are not well understood and are the focus of ongoing research. In chapter 8 we will investigate and characterise the interaction of MHD instabilities with the bulk plasma current.

2.5 Toroidal Current in a Tokamak

In a tokamak plasma the toroidal current is provided by 3 different physical effects.

Induced Ohmic Current, $\langle j_{\Omega, \parallel} \rangle$

The first contribution to the toroidal current density is generated by a transformer located at the centre of the torus. As current is ramped through the transformer a toroidal current is induced in the plasma (which can be viewed as a secondary winding). The form of the ohmic current density profile, $\langle \mathbf{j}_{\Omega, \parallel} \rangle(r)$, can be calculated by a number of codes such as ASTRA and CLISTE. In this thesis the CLISTE equilibrium code was used [31], see chapter 2.2.1 for more details on how this calculation is done.

⁵A proposed mechanism whereby the magnetic island drives a toroidal current.

Bootstrap Current, $\langle j \cdot B \rangle_{boot}$

The second contribution comes from what is known as the bootstrap current. The following explanation will only be a brief overview of the physics involved. A more comprehensive discussion can be found in [34].

A magnetic mirror is formed in a tokamak due to the radial gradient of the toroidal magnetic field. Particles following the helical magnetic field lines will encounter an increasing magnetic field as they attempt to approach the inner wall side of the torus. Those particles with sufficient parallel kinetic energy will overcome the magnetic mirror effect and become what we refer to as the passing particles, free to follow the helical field lines around the torus.

Particles with insufficient parallel kinetic energy will be reflected back to the low-field side of the torus, effectively trapped by the magnetic mirror. Trapped particles follow paths called banana orbitals. Figure 2.15 shows the poloidal projection of two such orbitals. On the outer side of the orbital the particles are moving in the direction of the toroidal current, while on the inner side they are moving against it. The trapping condition is shown below,

$$\frac{v_{\parallel}^2(R+r)}{v_{\perp}^2(R+r)} < \frac{B_{max}}{B_{min}} - 1 \quad (2.53)$$

$$\left| \frac{v_{\parallel}}{v_{\perp}} \right| < \sqrt{2 \frac{r}{R}} \quad (2.54)$$

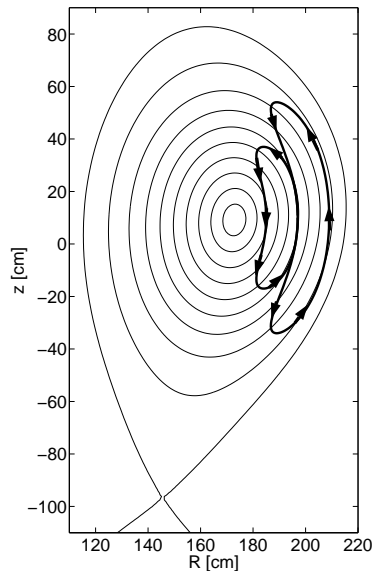


Figure 2.15: Particles reflected by the magnetic mirror effect follow banana orbitals. This figure shows the poloidal projection of two such orbitals.

Consider the region of intersection of these two orbitals indicated in figure 2.15. Here we find particles moving with and against the main toroidal direction.

If the population of both orbitals is the same, then no net current will exist in this region, as the particle motions effectively cancel. If, however, a radial density gradient exists then there will be a net current driven. This banana orbital current is transferred to the passing particle population through collisional coupling. The current carried by these passing particles is what is

referred to as the bootstrap current. A simple expression for the bootstrap current is given by,

$$\langle \mathbf{j} \cdot \mathbf{B} \rangle_{boot} \sim \sqrt{\varepsilon} \frac{\nabla p}{B_p} \quad (2.55)$$

in this thesis, however, the bootstrap current is calculated by the CLISTE equilibrium code, which is discussed more in chapter 2.2.1.

Auxiliary Heating Current Drive, $\langle \mathbf{j} \cdot \mathbf{B} \rangle_{aux}$

The third and final contribution to the toroidal current comes from the auxiliary heating (in our case this means current drive from the neutral beam heating). Fast neutral particles are injected into the plasma by the neutral beam heating system. These particles are ionised through collisions into ions and electrons. The *electron slowing-down-time*, $\tau_{sd,e}$, is much shorter than the *ion slowing-down-time*, $\tau_{sd,i}$. This means that after a time $\Delta t \sim \tau_{sd,e}$ there remains a circulating toroidal current of fast ions due to the neutral beam injection, $I_{circ}/I_{inj} = \tau_{sd,i}/\tau_{sd,e}$.

As these ions circulate around the torus they are slowed, in part, through collisions with electrons. These fast ion-electron collisions lead to an electron drift in the fast ion current direction, and therefore create a counter current. This current will exactly compensate the circulating ion current I_{circ} unless there is a difference in the charge of the injected beam ions Z_{inj} and the background plasma Z_{eff} ,

$$\frac{I_{netto}}{I_{circ}} \approx 1 - \frac{Z_{inj}}{Z_{eff}}(1 - f_{trap}) \quad (2.56)$$

where f_{trap} represents the fraction of trapped particles which are unable to contribute to the current compensation. The sum of the ion and electron currents gives the overall current density driven by the neutral beam injection, $\langle \mathbf{j} \cdot \mathbf{B} \rangle_{aux}$. If the heating is applied continuously the fast ion current will increase to the steady state condition where the particle injection rate matches that of the fast ion losses through collisions with bulk plasma ions and electrons. A neutral beam deposition code, such as FAFNER, is required to calculate the radial deposition profile.

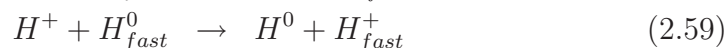
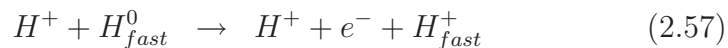
While the 3 contributions above should account for the total observed current profiles, a discrepancy has been observed, suggesting a 4th toroidal current contribution. MHD activity has been put forward as a possible source

of current drive [35]. Part of the goal of this thesis will be to verify if MHD activity can be statistically correlated to the current discrepancy. This investigation is discussed in detail in chapter 8.

2.5.1 The FAFNER Fast Particle Code

The FAFNER code is a numerical simulation designed to model neutral beam injection into 3-dimensional toroidal plasmas [8]. The code is divided into 3 sections.

1. The first section provides a 6 dimensional source function of neutral particles, $f(\mathbf{x}_i, \mathbf{v}_i)$, where \mathbf{x}_i and \mathbf{v}_i are the spatial and velocity coordinates respectively. Initial positions and velocities of fast neutrals emerging from the beam source are chosen using Monte Carlo techniques, appropriate for the given beam line configuration. Some fraction of these particles will be lost due to collisions with scrapers and ducts along the beam line, while the rest will reach the plasma and form the neutral source function.
2. The second part of the code transforms the neutral source function using a Monte Carlo algorithm to compute the initial ionisation of the neutrals in the plasma. A set of neutral particle coordinates are chosen from the neutral source function, $f(\mathbf{x}_i, \mathbf{v}_i)$, and to each an energy is assigned. Injected neutrals can become ionised through ion/electron impact ionisation, or charge exchange with thermal plasma ions,



The mean free path for all of these processes, $\lambda(\mathbf{x}_p, \mathbf{v}_i)$, is calculated for each of the relevant injected energy species. Note that λ is a function of the injected neutral velocity and of the spatial plasma coordinates \mathbf{x}_p . The plasma is described in terms of ion populations, flux-surface-averaged temperature and density profiles, along with the magnetic field configuration for the discharge in question. The resulting deposition of fast ions is governed by the following equation,

$$F(s) = \int f(\mathbf{x}_i, \mathbf{v}_i) \exp\left(-\int_0^s \frac{d\ell}{\lambda(\mathbf{x}_p, \mathbf{v}_i)}\right) d\mathbf{x}_i d\mathbf{v}_i \quad (2.60)$$

where $F(s)$ represents the flux of particles crossing the flux surface s .

- The details of all particles are then summarised by the energy deposition function $H(s)$ and the beam-shine-through, f_s , of injected particles which become lost from the system by either failing to ionise or by re-neutralisation through charge exchange with bulk plasma neutral atoms. $H(s)$ is defined such that,

$$\frac{1}{V_p} \int H(s) dV = 1 - f_s \quad (2.61)$$

where V_p is the plasma volume. FAFNER also calculates the toroidal current density driven by the injected neutrals by computing the electron compensation current (discussed briefly in the previous section).

An example of output produced by a typical FAFNER simulation is shown in figure 2.16. Here we see the ion and power deposition profiles presented along with the toroidal current density driven by the neutral beam injection. The results of FAFNER fast particle simulations are used to constrain the CLISTE equilibrium reconstructions carried out in this thesis. Additionally, the neutral beam driven current density, $\langle \mathbf{j} \cdot \mathbf{B} \rangle_{aux}$, will be used in chapter 8 to discuss interactions between MHD instabilities and the current profile.

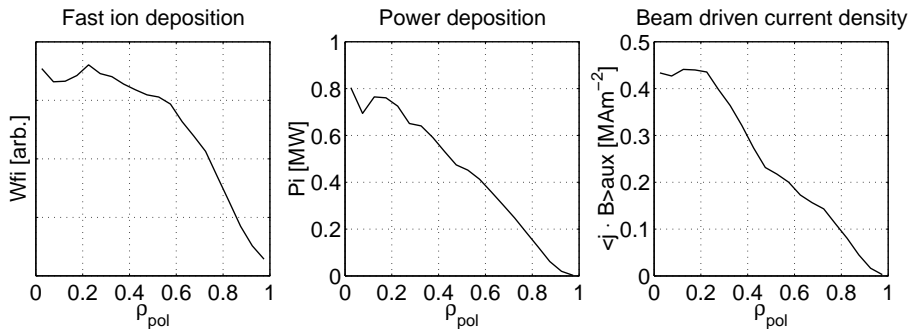


Figure 2.16: A subset of results from a FAFNER fast particle simulation. Here we see the ion and power deposition profiles plotted along side the neutral beam driven current density, $\langle \mathbf{j} \cdot \mathbf{B} \rangle (\rho_{pol})$.

Chapter 3

Diagnostics

ASDEX Upgrade has a wide range of plasma diagnostics which can be used for observing MHD modes. This section gives a series of short overviews for each of the main plasma diagnostics used in this thesis. Each overview will discuss what is observed and what the limitations of each diagnostic are.

3.1 Mirnov Coils

Mirnov coils are a standard tokamak diagnostic [42]. The Mirnov coil system on ASDEX Upgrade consists of 32 poloidally spaced coils and 10 toroidal coils, as shown in figure 3.1. Each coil measures the time derivative of the magnetic field,

$$U_{\text{coil}} \propto \frac{dB}{dt} \quad (3.1)$$

Therefore, the absolute amplitude of a perturbation caused by a mode with a poloidal mode number m , B_{pert}^m , is the time integrated signal. This amplitude drops off sharply over the plasma as shown in equation (3.2),

$$B_{\text{pert}}^m(r) \propto \frac{1}{r^{m+1}} \quad (3.2)$$

This means that signals due to core localised MHD modes are typically weak compared to those measured near the plasma edge.¹ It is possible to

infer the (m, n) of a mode by measuring a given phase across the coils. This is usually done using a phase fit [45]. For example, we attempt to fit the poloidal phase of the mode using the following expression,

$$\Phi = m(\theta + \lambda \sin \theta) + \delta_0 \quad (3.3)$$

where the poloidal mode number, m , Merezhkin correction factor, λ , and the initial phase, δ_0 , are all fit parameters. We then minimise χ^2 below for m, λ, δ_0 ,

$$\chi^2 = \frac{1}{N-p} \sum_{i=1}^N [(\Phi_f)_i - (\Phi_M)_i]^2 \quad (3.4)$$

where $p = 3$ is the number of fit parameters and $N =$ the number of measurements. The indices f and M represent the fitted and measured phase information. This method works best for low numbers of m and n . Figure 3.1 shows an example of phase fitting carried out for an $m = 6$ instability. The m number determination is further complicated by the presence of the passive stabilisation loop, PSL, structure on ASDEX Upgrade.

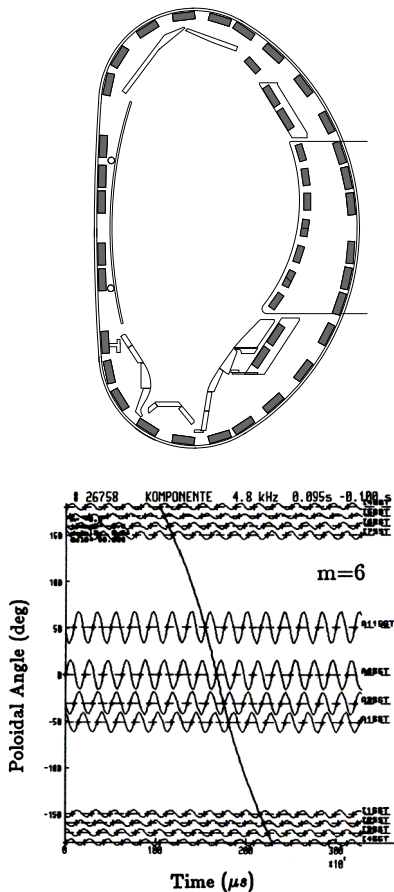


Figure 3.1: The Mirnov coil system consists of 32 poloidal and 10 toroidal coils. The lower figure shows an example of poloidal phase fitting carried out on an $m = 6$ mode (image courtesy of H.Zohm [45].)

¹Equation (3.2) is only true in the vacuum approximation and is used here for the sake of simplicity.

3.2 The Motional Stark Effect Diagnostic

In this thesis the Motional Stark Effect diagnostic (MSE) provides crucial information about the core magnetic field, which is in turn used as a constraint in the CLISTE equilibrium code. Without this diagnostic the fitted current density profiles would be only loosely constrained in the plasma core as the external magnetic field coils can only provide accurate information between $0.65 \leq \rho_{tor} \leq 1.00$. High accuracy current density profiles are required for the discussion in chapter 8 concerning the time evolution of such profiles during improved H-mode discharges. Fast neutral particles are injected into the plasma by the neutral beam heating system. These particles experience a Lorentz electric field, E_L , where,

$$\mathbf{E}_L = \mathbf{V}_{beam} \times \mathbf{B} \quad (3.5)$$

this field causes Stark splitting of the particles emission lines which is observed by the MSE diagnostic. The effect of Stark splitting is substantially greater than the Zeeman splitting due to the magnetic field [43]. The polarisation pattern of the Stark spectrum gives an accurate measure of the local magnetic pitch angle, γ , where,

$$\tan\gamma = \frac{B_\theta}{B_\phi} \quad (3.6)$$

B_θ and B_ϕ being the poloidal and toroidal magnetic field components respectively.² The pitch angle can be measured with an accuracy of $\pm 0.2^\circ$, with an effective temporal resolution of 3 ms, and a core spatial resolution of 6 cm. Figure 3.2 shows the location of the MSE diagnostic on ASDEX Upgrade and the arrangement of its spatial channels.

²on ASDEX Upgrade, however, this equation is more complicated due to the non-ideal viewing geometry of the MSE diagnostic [44].

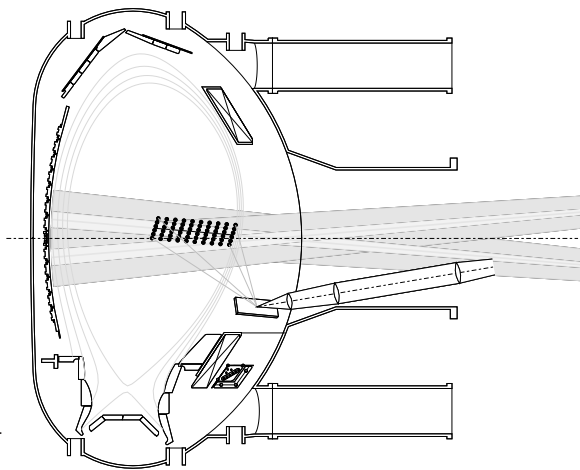
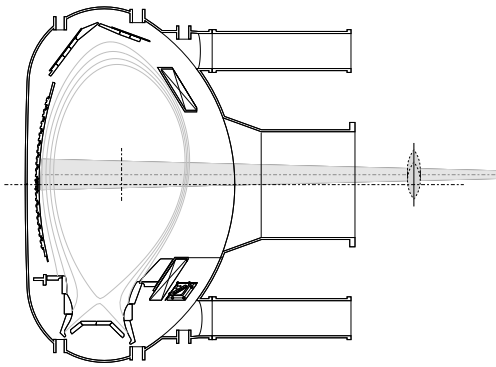


Figure 3.2: The geometry of the MSE diagnostic on ASDEX Upgrade. The vertical lines represent the location of the individual channels.

3.3 The Electron Cyclotron Emission Diagnostic

The Electron Cyclotron Emission (ECE) diagnostic measures the radiation emitted by electrons due to their motion around the magnetic field lines. The cyclotron frequency, ω_C , is the frequency of electron gyration due to the Lorentz force,



$$\omega_C = \frac{e_l B}{m_e} \quad (3.7)$$

where e_l is the electric charge, and m_e is the particle mass. The plasma is optically thick at resonant frequencies. This has the consequence that the plasma can be treated as a blackbody radiator at these frequencies, by Kirchhoffs law [46]. The radiated intensity, I_{BB} , is directly proportional to the electron temperature,

Figure 3.3: The sight line for the ECE diagnostic on ASDEX Upgrade.

$$I_{BB} = \frac{\omega^2}{4\pi^2 c^3} k T_e \quad (3.8)$$

B_{tor} provides most of the contribution to B in equation (3.7). Where $B_{\text{tor}}(R)$,

$$B_{\text{tor}}(R) \propto \frac{1}{R} \quad (3.9)$$

$$\omega_C(R) \propto \frac{e_l}{m_{e,i}} \frac{1}{R} \quad (3.10)$$

Equation (3.10) shows that spectral analysis of the cyclotron emission can be used to give electron temperature profiles, $T_e(R)$. Figure 3.3 shows the sight lines for the ECE diagnostic on ASDEX Upgrade. Perturbations caused by MHD instabilities can be detected by the ECE diagnostic as periodic fluctuations of the $T_e(R)$ profile. These fluctuations can be used to determine the position and island width of neoclassical tearing modes, see chapter 5.2.

3.4 The Soft X-ray Diagnostic

The soft X-ray (SXR) diagnostic on ASDEX Upgrade consists of 5 soft X-ray cameras, which are adapted to measure photons in the range $1 \rightarrow 10$ keV. This energy range is known as the soft X-ray range. It consists of contributions from bremsstrahlung, recombination, and line emission radiation [47]. The emissivity, ε_0 , given a Maxwellian velocity distribution is,

$$\varepsilon_0(r, \theta) = \int_0^\infty \alpha n_e^2 Z_{eff} g_{ff}(T_e, E) \frac{\exp\left(\frac{-E}{T_e}\right)}{\sqrt{T_e}} dE \quad (3.11)$$

where Z_{eff} is the effective ion charge, g_{ff} is the temperature averaged Gaunt factor, $\alpha = 3 \times 10^{11}$ is a constant, and n_e [cm^{-3}], T_e [keV] are the electron density and temperature. The emissivity measured by a SXR camera diode, ε , also depends on the response functions of the camera diodes, f_{cam} , and the filter, f_{fil} ,

$$\varepsilon(r, \theta) = \int_0^\infty \varepsilon_0(E; r, \theta) f_{cam} f_{fil} dE \quad (3.12)$$

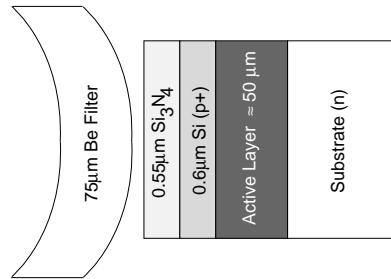


Figure 3.4: The layer thickness and materials in a Minisox camera diode.

If a sight line is broken into infinitesimal elements, length $d\ell$, it can be assumed that the total emissivity observed by a sight line, ε_{total} , is the sum of the emissivity elements,

$$\varepsilon_{total} = \sum_k \varepsilon_k d\ell \quad (3.13)$$

$$\varepsilon_k = G \frac{n_e^2}{\sqrt{T_e}} \sum_{i=1}^N f_{sum}(E_0 + i\Delta E) \exp\left(-\frac{E_0 + i\Delta E}{T_e}\right) \Delta E \quad (3.14)$$

where the integral of infinitesimal elements dE in equation (3.12) has been substituted by a summation over finite energy elements ΔE . The factor G is related to the geometry of the camera. The diode dimensions, D_x, D_y , are

used along with the pinhole, P_x, P_y , the camera focal length, Δ , and the sight line angle with respect to the camera normal, α . The MiniSox cameras used on ASDEX Upgrade have the following geometric correction factor [48],

$$G^{-1} = \frac{P_x P_y D_x D_y \cos^4 \alpha}{4\pi \Delta^2} \left[1 - \frac{1}{6} \frac{D_y^2 + P_y^2}{\Delta^2} \cos \alpha^2 + \frac{D_x^2 + P_x^2}{\Delta^2} \left(\sin \alpha^2 - \frac{1}{6} \right) + O\left(\frac{D_x, D_y, P_x, P_y}{\Delta}\right)^4 \right] \quad (3.15)$$

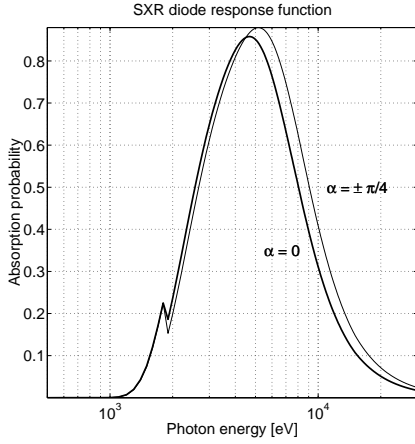


Figure 3.5: This figure shows the response function of the SXR Minisox cameras. The flat diode chip means the effective layer thicknesses and therefore overall response function changes as a function of incidence angle α .

$$f_{\text{sum}}(E) = \exp(-\mu_{Be}d_{Be} - \mu_{Si}d_{Si}) [1 - \exp(-\mu_{Si}d_0)] \quad (3.16)$$

where the absorption coefficients, μ_* , are functions of photon energy E . The angle of incidence for the radiation has an α dependence due to the flat diode chip used in the MiniSox cameras. This changing incidence angle leads to a slight change in the effective thickness of both the active and dead diode layers. The effective thickness of the Beryllium filter does not have an α dependence, due to the curvature of this filter. The effective thickness, d' changes as,

$$d' = \frac{d}{\cos \alpha} \quad (3.17)$$

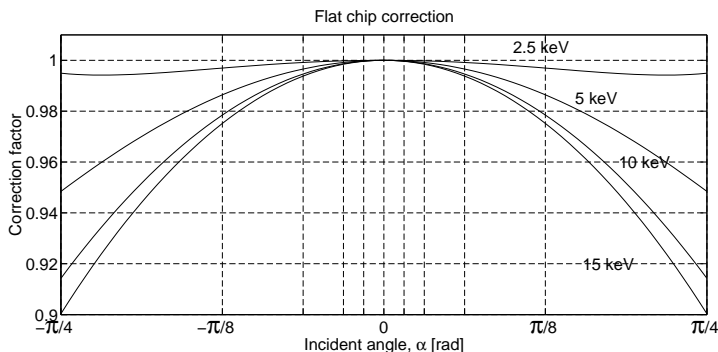


Figure 3.6: The flat chip correction factor, f_{flat} , for a typical SXR emissivity spectrum.

Figure 3.5 shows the range of different response functions due to the changing α . Figure 3.6 also shows the *flat chip correction term* f_{flat} , based on a typical SXR emissivity spectrum.

3.4.1 Mode Identification with the SXR Diagnostic

The line integrated signals can be used to determine poloidal mode number and position of MHD instabilities by comparing the spectral amplitude of a given mode across a single SXR camera. Figure 3.7 shows an example where the *B* camera on ASDEX Upgrade observes a (1, 1) ideal kink mode. If we compare the line integrated spectral amplitude we find a local minimum in the channel observing the centre of the instability, and a sharp drop at either extent of the mode. The number of local minima tells us the m number of the mode, and the FWHM of the outermost peak is taken to be the mode position. The SXR diagnostic can also provide a 2 dimensional reconstruction of the plasma emissivity by combining information from several SXR cameras. The development of this reconstruction software is explained in detail the following chapter.

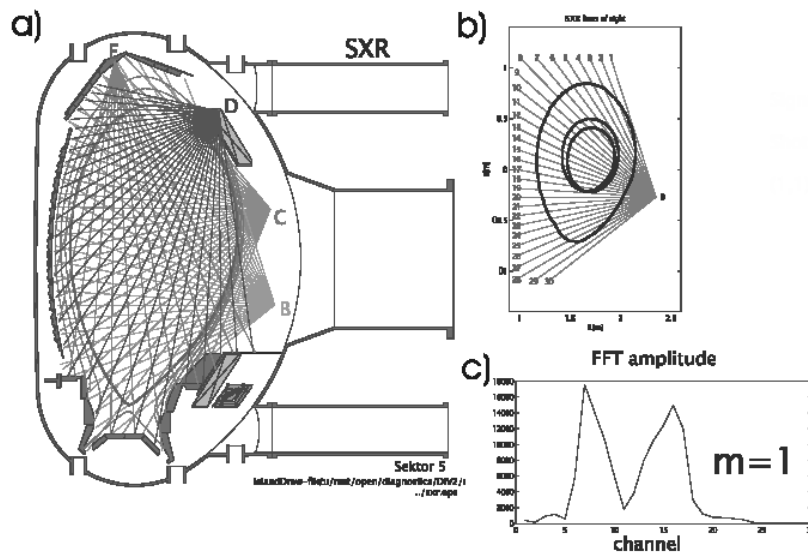


Figure 3.7: This shows how the SXR diagnostic can be used to determine the poloidal mode number and position of an MHD instability, by comparing the spectral amplitude of that instability across a single camera. The number of local minima in the spectral amplitude gives the poloidal mode number. In this case, one local minimum in the central channel tells us this is an $m = 1$ mode. The FWHM of the outermost peaks tells us the modes position.

Chapter 4

Soft X-ray Tomography

The goal of tomography is to reconstruct a cross-section of emissivity from a number of sight lines passing through that cross-section. If the emissivity is represented by a grid, and each point on that grid is stored in a column vector, \mathbf{g} , length n_g , then the line integrated signal vector, \mathbf{f} , will be,

$$\mathbf{f} = \mathbf{T}\mathbf{g} \quad (4.1)$$

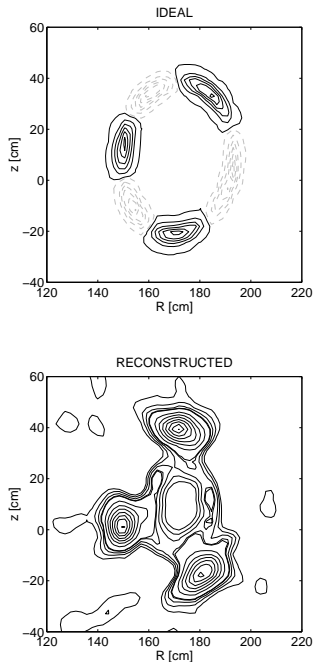
where \mathbf{T} is an $n_g \times n_f$ matrix, relating the contribution of each grid point to each sight line. Though elegant, it is nearly always impossible to invert the equation to solve for \mathbf{g} as for $n_f < n_g$, \mathbf{T}^{-1} does not exist, and even for $n_f = n_g$, \mathbf{T} is poorly conditioned. One possible solution is to minimise χ^2 ,

$$\chi^2 = \sum_{i=1}^{n_f} \left[\frac{f_i}{\sigma_i} - \sum_{j=1}^{n_g} \frac{T_{j,i}}{\sigma_i} g_j \right]^2 \quad (4.2)$$

where σ is the standard deviation of \mathbf{f} . While this can work well, it fails for the case $n_f \ll n_g$. In this scenario χ^2 can always be minimised to $\chi^2 = 0$ due to over fitting, i.e. there exist an infinite number of solutions. In order to reconstruct a cross section of emissivity to a reasonable resolution we need to employ a regularisation method. Several such methods exist: *linear regularisation*, *minimum Fisher*, and *maximum entropy*. It has been found that the maximum entropy regularisation yields the best results at the cost of processing time [49]. The maximum entropy method was selected as processing time was not a high priority for the purpose of this thesis.

4.1 Maximum Entropy Regularisation

The entropy of a solution \mathbf{g} with respect to a default model \mathbf{m} is defined as,



$$S = \sum_k^{n_g} \left[g_k - m_k - g_k \ln \left(\frac{g_k}{m_k} \right) \right] \quad (4.3)$$

where it can be shown that the maximum of $\phi(\alpha, \mathbf{g})$ is also the maximum of the posterior probability $P(\mathbf{g}|\mathbf{f}, I)$ [50]. The posterior probability is the probability of a solution \mathbf{g} , given the observed data \mathbf{f} , and some *a priori* information I is,

$$\phi(\alpha, \mathbf{g}) = -\frac{1}{2}\chi^2 + \alpha S \quad (4.4)$$

$$P(\mathbf{g}|\mathbf{f}, I) = \frac{P(\mathbf{g}|I) \cdot P(\mathbf{f}|\mathbf{g}, I)}{P(\mathbf{f}|I)} \quad (4.5)$$

Figure 4.1: Here we see the ideal solution compared with the maximum entropy tomogram. Maximum entropy fails to converge to the correct solution as it will never return a solution containing negative emissivity.

negative emissivity. For a reconstruction of the total plasma emissivity, negative emissivity does not have a physical meaning. However, a reconstruction of the perturbed emissivity can be negative. For example, consider the situation where the soft X-ray signals have been bandpass filtered to the frequency range of a (3, 2) NTM. The goal of such filtering would be not only to improve the signal to noise ratio, but to isolate the NTM from its harmonics and other MHD activity. In this reconstruction we would expect to see regions of high relative emissivity corresponding to the island O-points, and regions of low

This maximisation has been done using the curve fitting package *Newton*. Following the same method employed by the SXR tomography system on W7-AS [49].

One of the limitations of the maximum entropy method is that it will never select a solution containing negative

emissivity at the island X-points. Figure 4.1 shows the ideal emissivity compared with the maximum entropy reconstruction. Note the strong differences as the regularisation attempts to converge without negative emissivity.

This problem becomes crucial for situations where poor sight line coverage forces us to generate virtual sight lines using the assumption of a rotating mode, see chapter 4.3. In this case the reconstruction is valid only for a single rotating perturbation. For this reason the plasma background and signals due to other MHD instabilities must be filtered out for the generation of the virtual sight lines. These signals cannot be added again afterwards.

In spite of this apparent drawback it is still possible to reconstruct the perturbed emissivity correctly by using the following method. Essentially we take the difference of two reconstructions. The first, \mathbf{g}_1 , is calculated using the integrated sight line signals, \mathbf{f} . These signals are filtered to the bandpass of the perturbed emissivity, then added to a set of so called background signals. These background line integrated signals are calculated using the contribution matrix, \mathbf{T} and some background function \mathbf{G} . It has been found that the exact form chosen for \mathbf{G} has little to no influence on the final reconstruction. Typically a step function with smooth edges is used,

$$\mathbf{G}(\rho_{\text{tor}}) = \begin{cases} \varepsilon_0 & \rho_{\text{tor}} \leq 0.8 \\ \varepsilon_0 [\cos(\pi \frac{\rho_{\text{tor}} - 0.8}{0.2}) + 1] / 2 & \rho_{\text{tor}} > 0.8 \end{cases} \quad (4.6)$$

where the maximum background function emissivity, ε_0 , is chosen based on the values of \mathbf{f} ,

$$\varepsilon_0 = M_{\text{max}} \left(-\frac{\mathbf{f}}{\mathbf{b} + 1} \right) + \frac{1}{10} \sum_{k=1}^{n_f} \frac{|f_k|}{n_f} \quad (4.7)$$

$$b_i = \sum_{j=1}^{n_g} T_{j,i} G_j \quad (4.8)$$

where the function M_{max} returns the maximum value of a vector. The second reconstruction, \mathbf{g}_2 , is the reconstruction of that background function using the calculated line integrated signals.¹ The two reconstructions are

¹It may seem intuitive to use \mathbf{G} in place of \mathbf{g}_2 as, in the ideal scenario, both would be identical. While this is often the case, scenarios with poor sight line coverage can fail to correctly reconstruct the form of \mathbf{G} in the initial solution, \mathbf{g}_1 . The solution often contains 'holes' in these regions. However, as reconstruction \mathbf{g}_2 will contain the same artifacts the final subtraction, $\mathbf{g}_1 - \mathbf{g}_2$, will largely remove their influence.

then subtracted, yielding the perturbed emissivity, \mathbf{g} . Figure 4.2 shows the resulting tomogram of this two stage reconstruction. This is summarised by the equations below,

$$\phi_1(\alpha_1, \mathbf{g}_1) = -\frac{1}{2}\chi_1^2 + \alpha S, \text{ maximise} \quad (4.9)$$

$$\phi_2(\alpha_2, \mathbf{g}_2) = -\frac{1}{2}\chi_2^2 + \alpha S, \text{ maximise} \quad (4.10)$$

$$\chi_1^2 = \sum_{i=1}^{n_f} \left[\frac{f_i}{\sigma_i} + \sum_{j=1}^{n_g} T_{j,i} G_j - \sum_{j=1}^{n_g} \frac{T_{j,i}}{\sigma_i} g_j \right]^2 \quad (4.11)$$

$$\chi_2^2 = \sum_{i=1}^{n_f} \left[\frac{f_i}{\sigma_i} - \sum_{j=1}^{n_g} \frac{T_{j,i}}{\sigma_i} G_j \right]^2 \quad (4.12)$$

$$\mathbf{g} = \mathbf{g}_1 - \mathbf{g}_2 \quad (4.13)$$

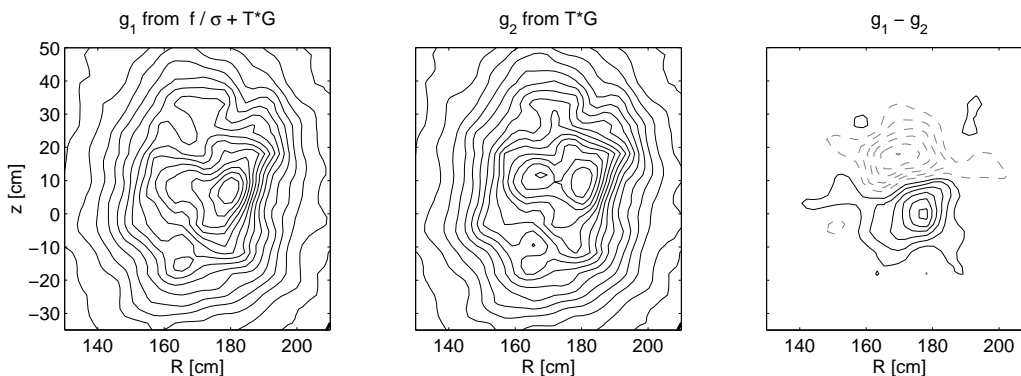


Figure 4.2: Using a two stage maximum entropy reconstruction it is possible to reconstruct negative emissivity. The first reconstruction is done using $(\mathbf{f} + \mathbf{T}\mathbf{G})$, while the second is done using only $(\mathbf{T}\mathbf{G})$. The difference of the two yields the tomogram on the right, showing only the perturbed emissivity.

4.2 The Contribution Matrix

The contribution matrix \mathbf{T} is calculated by considering the sight line arc of each diode projected onto a square-pixel grid representing the plasma cross section. Figure 4.3 shows a poloidal cross section of one of the Soft X-ray

MiniSox cameras. A sight line arc is described by (R_0, z_0) a starting point within the vessel, and $(\theta, \Delta\theta)$ the sight line centre and its angular extent. If we take (R_0, z_0) to be the centre on the camera pinhole, then it can be shown from simple geometry that,

$$\alpha = \tan^{-1} [(n_{\text{diode}} - n_0)(D_x + D_d)/\Delta] \quad (4.14)$$

$$\theta = \theta_{\text{cam}} + \alpha \quad (4.15)$$

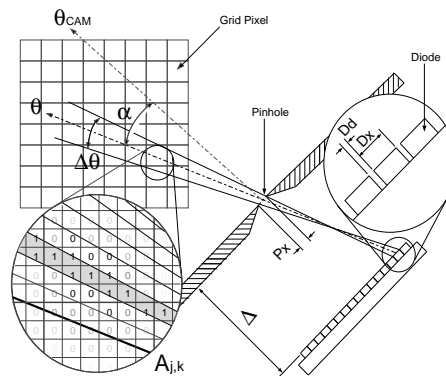
$$\Delta\theta = \sin^{-1} [(P_x + D_x)(2\Delta/\cos\alpha)^{-1}] \quad (4.16)$$

Equation (3.13) shows that the emissivity observed by a diode can be taken to be the sum of emissivity within infinitesimal sight line elements. Which in turn translates into the contributed sum of pixel emissivity. In order to calculate this contribution, the surface of the diode is divided into N_D poloidal slices, each with a corresponding sight line S_i .

Likewise each pixel is divided into N_R , N_z divisions. The contribution of the n^{th} pixel to the ℓ^{th} sight line, $T_{\ell,n}$ is,

$$T_{\ell,n} = \sum_{i=1}^{N_D} \sum_{j=1}^{N_R} \sum_{k=1}^{N_z} \frac{S_i}{N_D} \frac{A_{j,k}}{N_R N_z} \quad (4.17)$$

$$S_i A_{j,k} = \begin{cases} 0 & A_{j,k} \text{ not within } S_i \\ 1 & A_{j,k} \text{ within } S_i \end{cases} \quad (4.18)$$



The result will be a number from $0 \rightarrow 1$ where a pixel with $T_{\ell,n} = 0$ cannot be seen by this sight-line ℓ , and $T_{\ell,n} = 1$ when all of pixel n illuminates all of diode ℓ . Figure 4.4 shows a typical sum $\sum_{\ell} T_{\ell,n}$

Figure 4.3: A poloidal cross section of one of the Soft X-ray diagnostic cameras.

4.3 Rotation Tomography

Figure 4.4 represents a *best case scenario* for ASDEX Upgrade. A high number of sight line crossings gives a reasonable density of information across the plasma. In cases where the number of working sight lines is limited, the maximum entropy method will fail to converge to a meaningful solution.

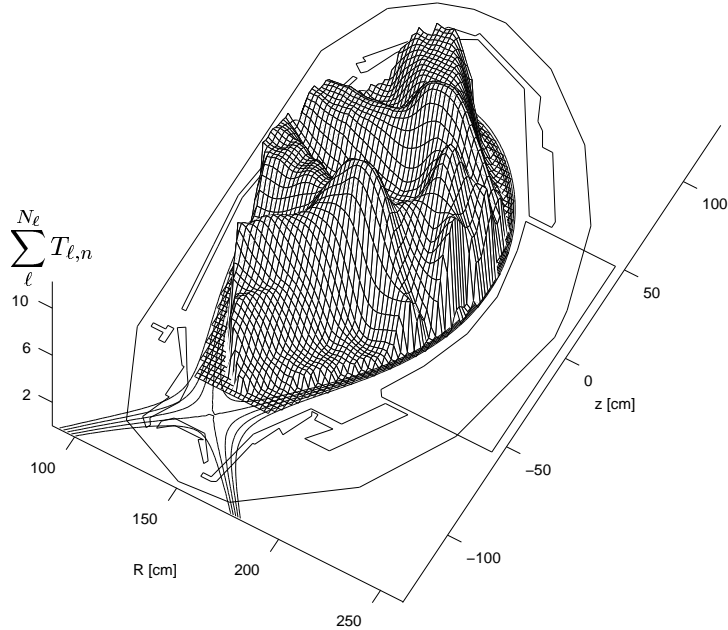


Figure 4.4: The sight line sum of the SXR contribution matrix, \mathbf{T} , on ASDEX Upgrade. Notice that the contribution matrix has only been calculated for a grid bounded by the separatrix. This is done for two reasons; the first is to minimise the number of grid points needed for the reconstruction, the second is that the virtual sight-lines (discussed in the next section) can only be calculated for grid points where θ^* is defined i.e. within $\rho_{pol} = 1.0$.

However, even with a low number of sight lines, it is possible to reconstruct MHD structures if it is assumed that these structures are rotating along a constant contour of ρ_{pol} .

Consider a line of sight, \mathbf{S} , observing a mode at time t_0 , rotating with an angular frequency ω . After a time Δt the mode will have rotated such that any feature seen by \mathbf{S} at t_0 will now be seen by a different sight line \mathbf{S}' , which is rotated with respect to \mathbf{S} . In this way it is possible to define a virtual sight line said to be observing at time t_0 but using data from time $t_0 + \Delta t$. All that is left is to calculate the shape of the virtual sight line, \mathbf{S}' . For this we need to consider how MHD instabilities rotate in the poloidal plane.

It is not enough to apply a simple Cartesian mapping $\mathbf{S}(r, \theta) \rightarrow \mathbf{S}'(r, \theta)$ as MHD instabilities do not rotate along a circular contour and do not ro-

tate with a constant wavelength. In the coordinate system $(\rho_{\text{pol}}, \theta^*, \varphi)$ both the wavelength and radial position are constant. The radial coordinate ρ_{pol} is defined in equation (2.15). The angular coordinate θ^* is related to the Cartesian poloidal angle, θ , by,

$$\theta^*(\psi, \theta) = 2\pi \frac{\int_0^\theta \partial(R, z)/\partial(\psi, \theta') R^{-1} d\theta'}{\int_0^{2\pi} \partial(R, z)/\partial(\psi, \theta') R^{-1} d\theta'} \quad (4.19)$$

where ψ is the poloidal magnetic flux. Mappings for θ^* are calculated routinely on ASDEX Upgrade and are based on the equilibria reconstructed by the CLISTE equilibrium code. Using the following mapping it is possible to generate a new contribution matrix, $T'_{S,i}$, from the contribution matrix for an existing sight-line S , $T_{S,i}$,

$$\rho'_{\text{pol}} = \rho_{\text{pol}} \quad (4.20)$$

$$\theta^{*'} = \theta^* - \omega \Delta t \quad (4.21)$$

Figure 4.5 shows the positions of real sight lines and their corresponding virtual sight lines. Although ω is often unknown, it is possible to infer ω from the Fourier frequency of a mode, f_{MHD} , and its poloidal mode number,

$$\omega = \frac{2\pi f_{\text{MHD}}}{m} \quad (4.22)$$

Even if m is not known it is possible to use trial m numbers and compare the resulting reconstructions. Figure 4.6 shows 3 reconstructions of an $m = 2$ mode using trial $m = \{1, 2, 3\}$. The tomograms which use $m = \{1, 3\}$ are noticeably distorted, while $m = 2$ results in a relatively clean reconstruction.

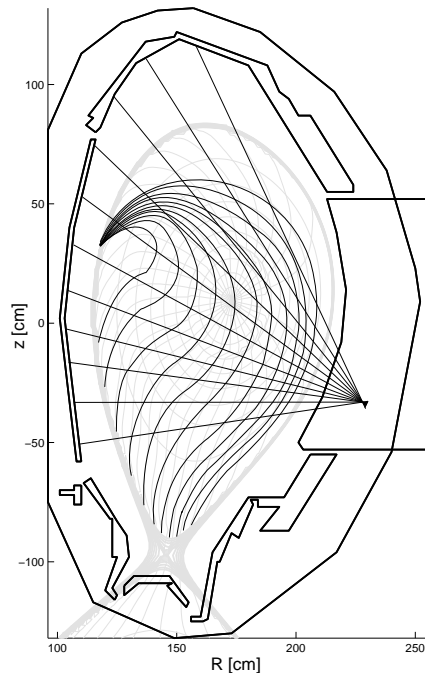


Figure 4.5: The real sight lines are rotated with constant ρ_{pol} , from $\theta^* \rightarrow \theta^* - \omega \Delta t$, giving the virtual sight lines. Note that the virtual sight-lines can only be calculated for $\rho_{\text{pol}} \leq 1.0$.

The additional virtual sight lines can make it possible for the maximum entropy algorithm to converge in spite of poor sight line coverage. Even in situations where there are enough real sight lines to converge, the additional virtual sight lines improve the quality and resolution of this reconstruction.

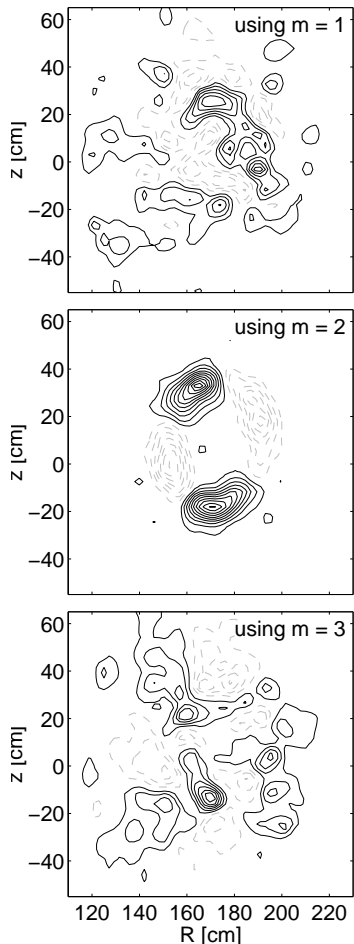


Figure 4.6: An $m = 2$ mode is reconstructed using 3 different trial values, $m = \{1, 2, 3\}$. The central reconstruction, using $m = 2$, is noticeably cleaner than the tomograms using the incorrect value for m .

Figure 4.7 shows a comparison between tomograms using a pure maximum entropy, and maximum entropy plus the rotation algorithm. For 150+ working sight lines both reconstructions are clear. Once the number of working sight lines drops below 70 the pure maximum entropy tomograms become unclear. Rotation tomography for such scenarios becomes essential.

For this method we need to assume we are observing a single MHD mode. A Butterworth filter is applied to the SXR data to filter out the plasma background and all but one MHD mode. The filtering must be done over a time window long enough to ensure a good spectral resolution. This time window must also be short enough such that the structure in question remains essentially invariant in rotation rate, ω and radial position, ρ_{pol} . A typical time buffer length is 0.01s.

While rotation tomography produces better reconstructions than pure maximum entropy, it has done so by adding assumptions about the behaviour of the MHD mode, and equilibrium mapping that may not be valid. These assumptions may limit its usefulness. For example, the assumption of mode rotation is not valid for rapidly evolving events such as a sawtooth crash.

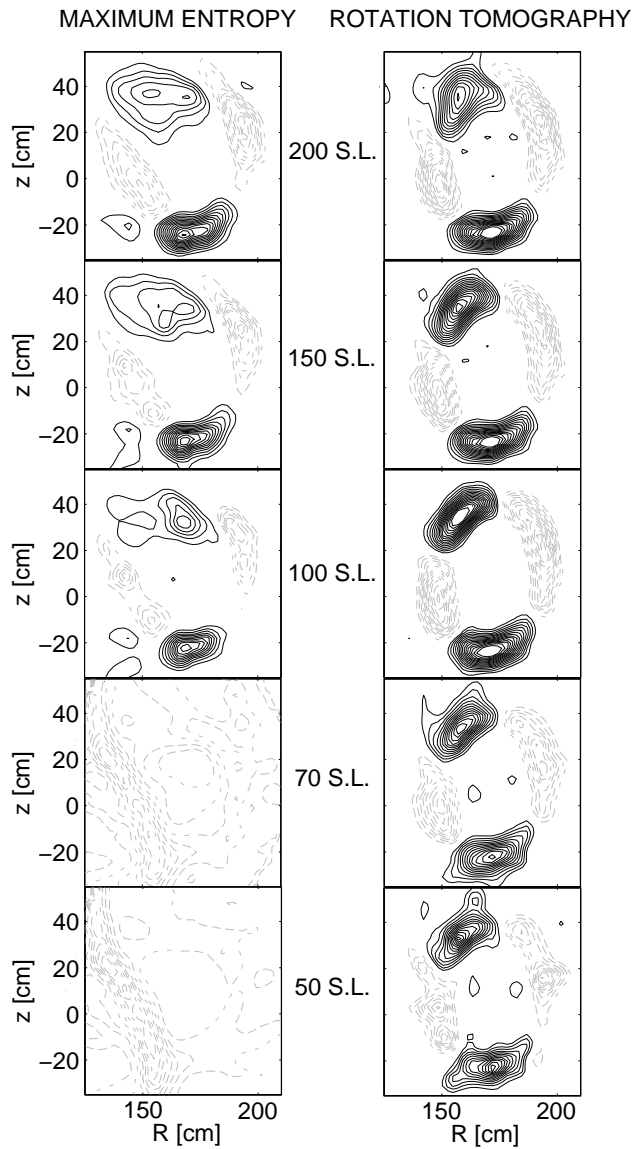


Figure 4.7: The top row of tomograms have been reconstructed with a pure maximum entropy method, making no assumption about the mode rotation. The lower row use maximum entropy plus rotation. It can be seen that for 150 sight lines both methods perform well and produce a clear reconstruction of the MHD mode. Whereas for 70 sight lines and less, pure maximum entropy becomes unclear, while the rotation tomography still produces good reconstructions. These reconstructions have been done using synthetic data.

4.4 Periodic Noise Reduction

Tomography is very sensitive to signal noise. While rotation tomography increases the sight line coverage, it does not improve the overall signal to noise ratio of the system. Furthermore, it has amplified the effect of any systematic errors in the original data. Periodic noise reduction seeks to improve the signal to noise ratio by averaging the data over a number of mode periods. The principle makes the same assumption as rotation tomography, that a given sight line observing a phase of the instability will observe that same phase after a time $\tau = 2\pi\omega^{-1}$. Unlike rotation tomography this does not make any assumptions about the $(\rho_{\text{pol}}, \theta^*)$ mapping. The signal vector, $\mathbf{f}(t)$, is averaged over a number of periods N_τ to give \mathbf{f}' ,

$$f'_i(t) = \frac{1}{N_\tau} \sum_{n=0}^{N_\tau-1} f_i(t + n\tau) \quad (4.23)$$

The mode must maintain approximately the same dominant frequency of the time window $N_\tau\tau$. Typically signals are averaged over $10 \rightarrow 20$ periods.

4.5 Smoothness Constraint

Additional smoothness constraints can be imposed to reduce the gradient between adjacent grid points. Although the imposition of a smoothness condition improves convergence to the ideal solution, it can also erase features of interest, such as emissivity fluctuations due to MHD activity, see figure 4.9. The smoothness condition distributes the emissivity of each pixel of the reconstruction to nearby pixels. The distribution is Gaussian, decreasing with increasing pixel separation, r_{kl} . The emissivity of the k^{th} pixel after smoothing is,

$$g'_k = \sum_{\ell=1}^{n_g} \frac{\exp\left(\frac{-r_{k\ell}^2}{\lambda^2}\right)}{\sum_{\ell=1}^{n_g} \exp\left(\frac{-r_{k\ell}^2}{\lambda^2}\right)} g_\ell \quad (4.24)$$

where λ is the *spot-radius* of the smoothness condition, and \mathbf{g} is the emissivity before smoothing. λ should be chosen, such that convergence is improved without destroying features of interest. λ is usually in the range $\lambda = \{3 \text{ cm} \rightarrow 8 \text{ cm}\}$.

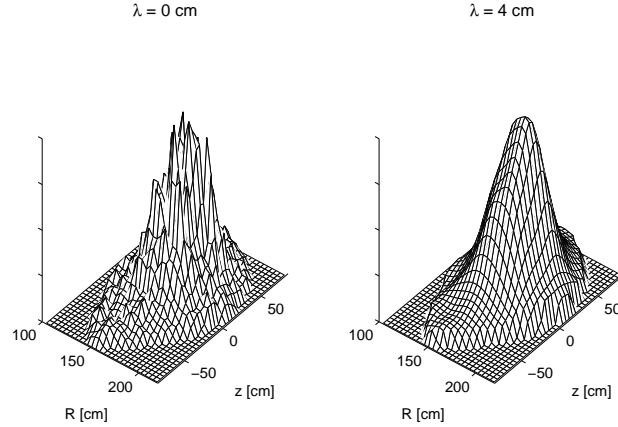


Figure 4.8: Maximum entropy reconstructions with and without additional smoothness constraint.

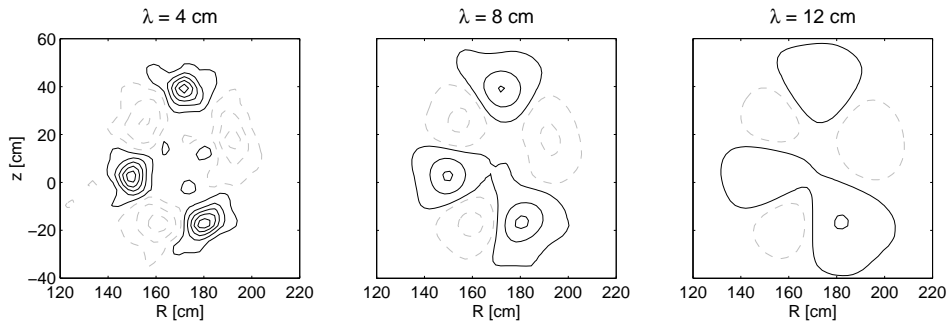


Figure 4.9: The result of an increasingly rigid smoothness condition on an MHD mode. λ is the spot-radius of the smoothing function. For $\lambda > 10$ cm the mode amplitude is greatly diminished, and mode position becomes unclear.

4.6 Example: Disruption Reconstructions

Using maximum entropy tomography without rotation assumption it is possible to reconstruct the loss of vertical plasma control prior to a disruption. Figure 4.10 shows such an example. Note this initial good agreement between the reconstructed emissivity and the contours of ρ_{pol} . This agreement is significant because, in this case, the tomography program has no a priori information about the equilibrium.

Over the next 13 ms there is a loss of vertical plasma control and the SXR reconstructions show the entire plasma dropping into the divertor region. After 13 ms there is a sudden loss of emissivity and the SXR cameras cease to produce physically meaningful signals.

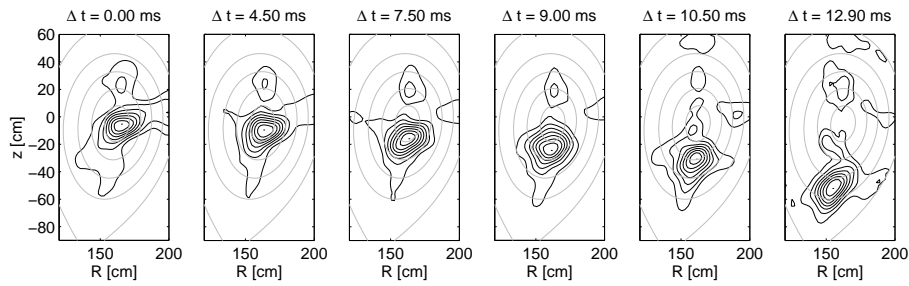


Figure 4.10: This figure shows the evolution of the plasma emissivity prior to a disruption as reconstructed by the SXR tomography program. The plasma can be observed dropping into the divertor region over ~ 13 ms. After the plasma has dropped ~ 60 cm there is a sudden reduction in the plasma emissivity. Reconstructions beyond this point are impossible as the SXR channels cease to return physical signals.

Chapter 5

MHD Instability Database

In order to study the behaviour of MHD instabilities a database was constructed consisting of time series for each type of MHD instability over the duration of the shot. These time series contain quantities such as mode frequency, and amplitude for continuous modes. In the case of fishbones only one time series exists, a boolean operator: 0 for no fishbone activity, or 1 for any time interval where fishbone bursts are observed. For the ease of comparison, all the above time series use the same time base. The sawtooth instability is an exception as for this MHD instability a special time base is used. In this case, each time point represents the midpoint of a sawtooth crash. 6 time series were recorded for each discharge: pre/post-crash core temperature, normalised sawtooth amplitude, inversion radius, envelope, and the inter-sawtooth period.

In addition to the continuous time series, over 500 time slices were selected for which plasma profiles for ion/electron temperature, and electron density were fitted. The position and island size of any instabilities present in these time slices were also determined, wherever possible. The following sections will explain the identification and quantification process with the available plasma diagnostics.

5.1 Correlated Spectrogram Analysis

A new spectrogram algorithm has been developed to aid in the identification and analysis of MHD instabilities. The correlated spectrogram algorithm

simultaneously achieves smoother spectral and temporal resolution than a traditional spectrogram. This smoothing aids in the identification of MHD modes, which often show significant variation in both time and frequency.

In this method, many spectrograms are calculated for the same time window using sliding Fourier transform windows of different lengths, $k\Delta t$, for $k = 1, 2, 3, \dots, N$. The transform for spectral amplitude, F , as a function of time, t , and frequency, ω , is shown below,

$$F(\omega, t) = \frac{1}{N\sqrt{2\pi}} \sum_{k=1}^N \int_{t-k\Delta t}^{t+k\Delta t} f(t') e^{-i\omega t'} dt' \quad (5.1)$$

In practice the integral above is approximated using a discrete Fourier transform [51]. Those spectrograms with a large $k\Delta t$ will achieve a greater spectral resolution at the cost of temporal resolution, while the opposite is true for spectrograms calculated with a short $k\Delta t$. All spectrograms are mapped onto a common grid using linear interpolation. This common grid is chosen to have the temporal resolution of the shortest $k\Delta t$ spectrogram and the spectral resolution of the longest $k\Delta t$. All mapped spectrograms are then averaged together, grid point for grid point. This cross correlation between different spectrograms reinforces regions of overlap while averaging over features that are present only on a few of the spectrograms. Figure 5.1 compares one such correlated spectrogram (bottom) with a traditional spectrogram calculated for the same overall time window (top).

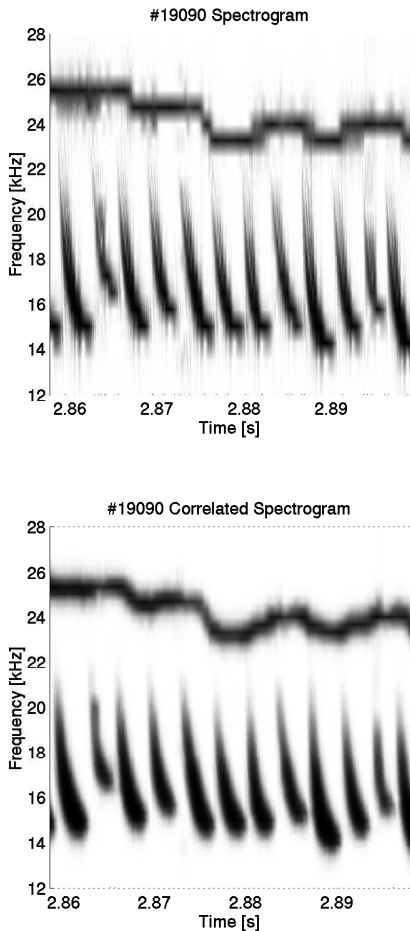


Figure 5.1: The correlated Mirnov coil spectrogram (bottom) simultaneously achieves a higher spectral and temporal resolution than the traditional spectrogram (top).

Furthermore it is possible to separate even and odd toroidal mode number MHD instabilities by taking either the sum or difference of the signals

from two Mirnov coils, π radians apart in the toroidal direction [42]. When this technique is combined with the correlated spectrogram algorithm, it is possible to effectively switch on or off a given type of MHD activity. This can be useful for situations such as the one illustrated by figure 5.2, where fishbone bursts and a $(3, 2)$ NTM converge into the same frequency band. At some point there is a change in the plasma conditions, and the fishbone bursts stop. The exact endpoint, however, is masked by the presence of the $(3, 2)$ NTM. When we separate this correlated spectrogram into its odd and even toroidal components we find the $n = 1$ fishbones appear only in the odd spectrogram, while their second harmonic and the $n = 2$ NTM appear only in the even plot. This makes finding the fishbone termination point a simple task.

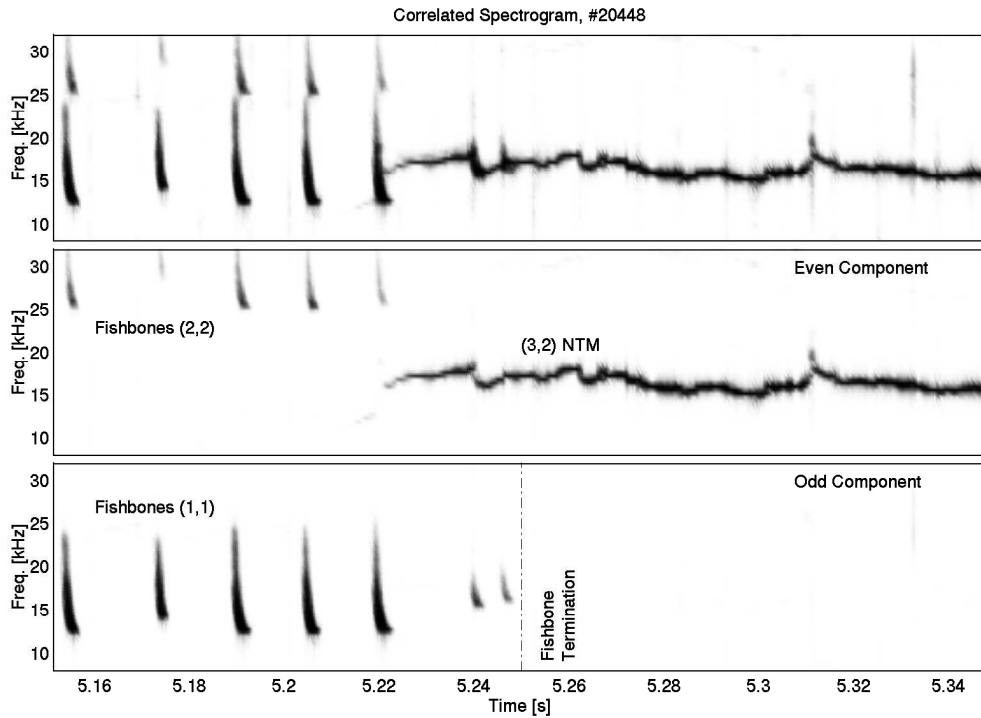


Figure 5.2: In the upper spectrogram it is difficult to determine the exact endpoint of the fishbone bursts, as both the fishbone bursts and a $(3, 2)$ NTM converge into the same frequency band. However, when we create correlated spectrograms of the even and odd toroidal components, we find the $n = 1$ fishbone bursts appear only in the odd spectrogram, while their $(2, 2)$ harmonic and the $n = 2$ NTM appear only in the even. This makes determining the endpoint of the fishbone bursts simple.

5.2 Neoclassical Tearing Modes

Neoclassical Tearing Modes (NTM) are continuous resistive MHD instabilities which form magnetic islands in the plasma equilibrium. They can be readily identified from a soft X-ray or Mirnov coil wavelet plot as they form strong continuous bands, varying slowly in frequency with time. Once identified as an NTM, each NTM is labelled by its poloidal and toroidal wave numbers (m, n) . m and n are determined using phase tracking across poloidally and toroidally separated Mirnov coils as described in chapter 3.1. Figure 5.3 shows an example of a toroidal wavenumber spectrogram resulting from this phase analysis. Here the different types of NTM can be clearly distinguished: a $(4, 3)$ NTM appears first, to be replaced by a $(3, 2)$ NTM and its 1st harmonic the $(6, 4)$.

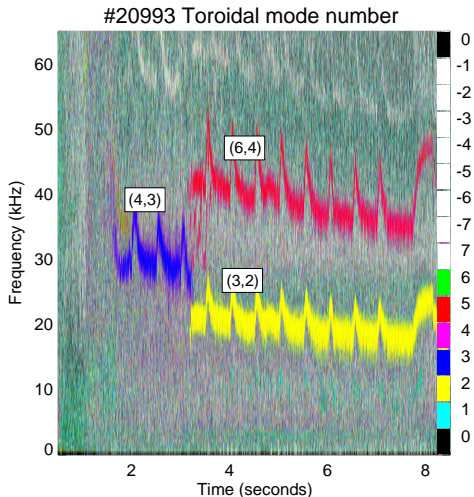


Figure 5.3: This figure shows an example of a toroidal wavenumber spectrogram obtained using phase tracking with the Mirnov coil diagnostic. Here 3 NTMs can be clearly distinguished. First a $(4, 3)$ NTM grows to be replaced by a $(3, 2)$ NTM and its 1st harmonic, $(6, 4)$.

temperature. This fluctuation is zero at the island centre, where the phase of the fluctuation also changes by π radians. The fluctuation amplitude increases with distance from the island centre to two local maxima at either extreme of

Once each NTM has been identified its frequency is tracked in the Mirnov coil spectrogram. This gives us a time series of mode frequency and spectral amplitude, which can be integrated to give the relative NTM amplitude with time. If we assume $B_r \approx B_\theta$ then the magnetic signal can be related to the NTM island width, w , by the following expression [45],

$$w \propto \sqrt{B_r} \quad (5.2)$$

For a number of select time windows the electron temperature profile is analysed in this frequency range using the ECE diagnostic. Figure 5.4 shows an example of such an electron temperature profile. As the island rotates in the plasma it causes a local fluctuation in the electron temperature

the islands O point [52]. The island centre is taken to be the local minimum between two maxima in spectral amplitude, where a phase jump of $\sim \pi$ is also observed. The island width is taken to be the distance between these two maxima. Often only one of the two maxima is clearly identifiable. In such cases the distance between the minimum and one available maximum is taken to be half the island width, $w/2$. This is only a rough approximation as the island width, w , is typically asymmetric about the rational surface. In the example below the inner maximum cannot be resolved due to coupling with a (n, n) instability further inside the plasma. This coupling gives rise to the large smeared peak spanning $\rho_{pol} = 0.0 \rightarrow 0.6$.

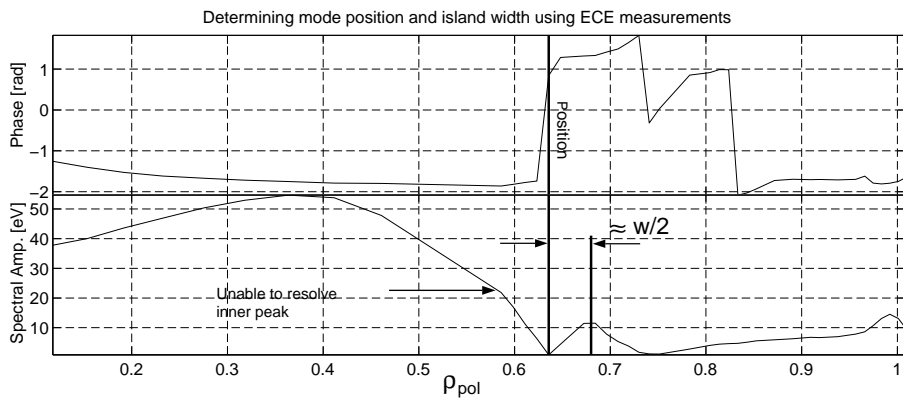


Figure 5.4: This figure shows a typical NTM T_e fluctuations profile. The indicated maxima correspond to the outer extent of the islands O point. The distance between them can therefore be taken as the island width, w . The island centre can be taken as the local minimum between these two maxima. This minimum in the spectral amplitude should coincide with a phase shift of $\sim \pi$. In this example only one of the outer maxima is visible. The inner maximum cannot be resolved due to mode coupling with an (n, n) instability located further inside the plasma at the $q = 1$ surface. In such cases we take the distance between the minimum and maximum as an approximation for $w/2$. This is only an approximation as the island width is often asymmetric about the rational surface.

The Nyquist frequency of the ECE diagnostic is $16kHz$ for all of the discharges in the database. This restricts ECE analysis to low n MHD modes, $n = \{1, 2\}$, as modes with $n > 2$ typically have a frequency in excess of $16kHz$. The radial resolution of the ECE diagnostic was high towards the plasma edge for the discharges studied in this thesis. Therefore the

mode position information is best for instabilities with a high m/n ratio, e.g. $(2, 1)$, $(3, 2)$, and not well suited for core MHD modes such as $(1, 1)$, $(2, 2)$, \dots

The soft X-ray diagnostic can also provide information about the NTM poloidal mode number and approximate radial position, see figure 3.7. While in some cases it is possible to correlate these position measurements with the ECE diagnostic, very often the modes in question are above the $16kHz$ ECE Nyquist frequency.

Additionally, the information from several SXR cameras can be combined to give a tomographic reconstruction of the plasma emissivity cross section,

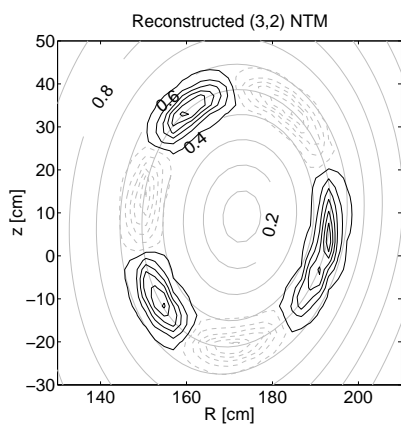


Figure 5.5: This figure shows an example of an SXR tomogram of a $(3, 2)$ NTM. Here the poloidal mode number and position can be easily identified.

as was discussed in chapter 4. An example of such a reconstruction is shown in figure 5.5. Here the NTM can easily be identified as having $m = 3$, located on the $\rho_{\text{pol}} = 0.3$ flux surface.

(top) where a potential precursor event has been clearly identified in the ECE time series, and an SNTM (bottom) where no precursor is present.

It is also necessary to distinguish between those NTM whose onsets are triggered by sawtooth or fishbone precursor modes, and spontaneous NTM onset. This is done manually by identifying potential precursors. If an NTM does not appear to have any potential precursor it is labelled as a Spontaneous-onset NTM (SNTM). All NTMs with a potential precursor are in turn grouped together as Precursor-triggered NTMs (PNTM). Figure 5.6 shows an example of a PNTM

SNTMs can also be positively identified using the relative mode amplitude as measured by the Mirnov coils. We take the ratio of the mode amplitude during the NTM onset to the saturated mode amplitude to be equal to the ratio $w_{\text{seed}}/w_{\text{sat}}$ by making the assumption that the radial location of the NTM rational surface remains essentially unchanged from mode onset to saturation. This ratio is then compared to the ratio $w_{\text{min}}/w_{\text{sat}}$ predicted by the Rutherford equation (2.34). We find that for SNTMs the two ratios match almost exactly, while for PNTMs we find $w_{\text{seed}}/w_{\text{sat}} \geq w_{\text{min}}/w_{\text{sat}}$. This result is discussed in more detail in chapter 6.1.

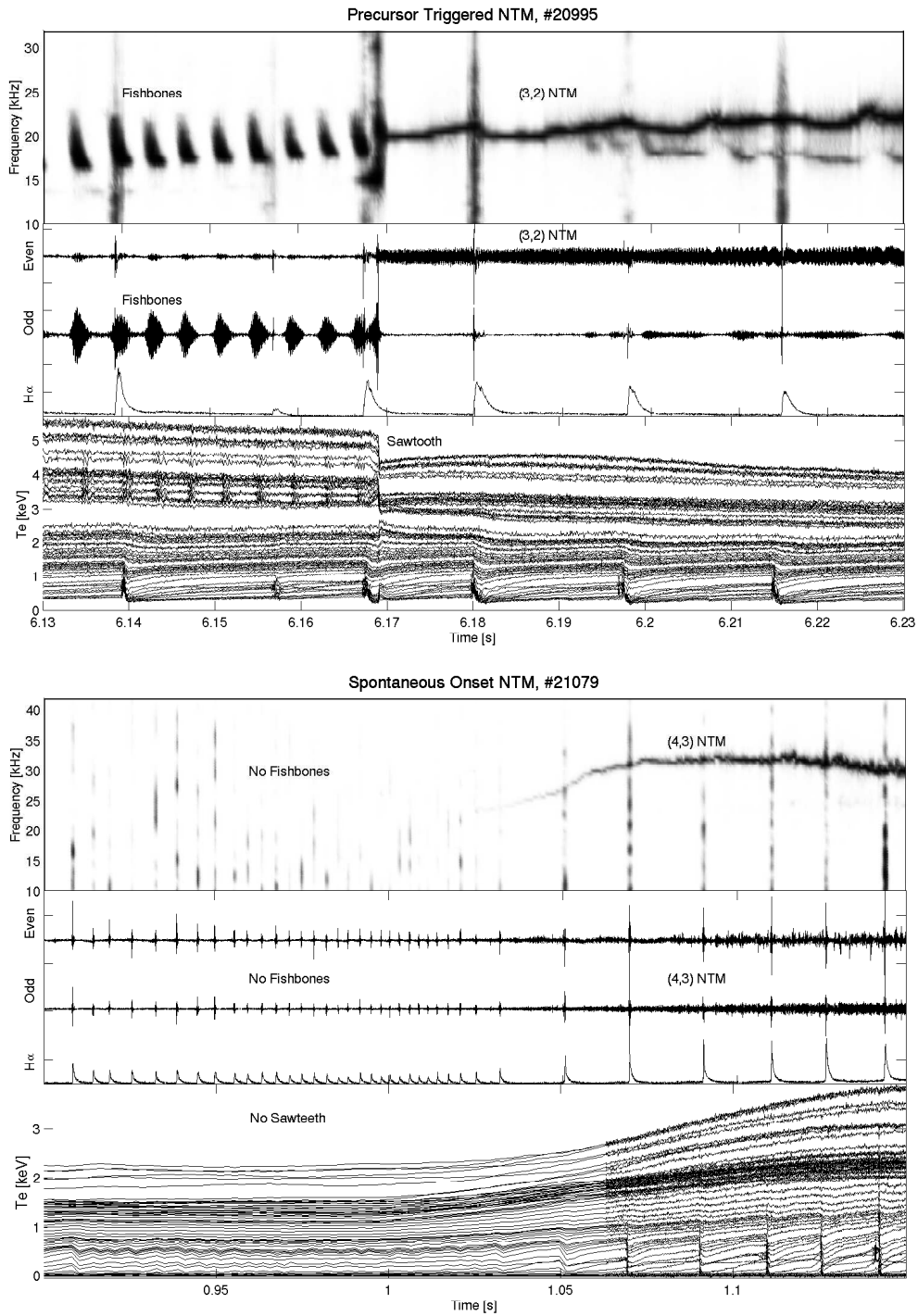


Figure 5.6: The upper figure shows an example of an NTM that has been potentially triggered by a sawtooth crash. The sawtooth crash is visible in the ECE time series and the NTM begins to grow immediately afterwards. The lower figure shows an example of spontaneous NTM onset. The NTM begins to grow without the presence of a sawtooth or fishbone precursor.

5.2.1 Frequently Interrupted Regime NTMs

The techniques used to study Frequently Interrupted Regime NTMs (FIR-NTMs) are the same as for the standard regime NTMs discussed above. When the relative mode amplitude is obtained from the frequency tracking routine it is possible to manually spot and label FIR-NTM as those NTM which show sharp periodic drops in mode amplitude. An example of a relative amplitude time series for a FIR-NTM is shown in figure 5.7. The upper time series is the relative amplitude of a (3, 2) NTM. At the point where it enters the frequently interrupted regime the lower time series begins.

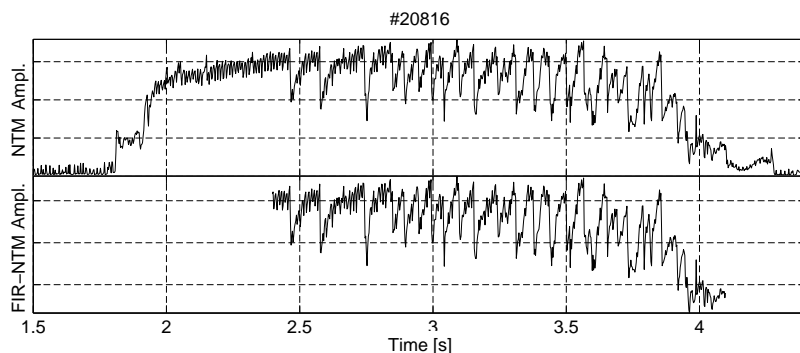


Figure 5.7: The uppermost time series belongs to a standard regime (3, 2) NTM. At the point where this NTM becomes a FIR-NTM the bottom time series begins.

5.3 Fishbones

The fishbone instability has a characteristic downward sweeping frequency progression that is easily recognised in a Mirnov or SXR spectrogram. Fishbones often occur in succession. For the entire time interval where the fishbones are observed the database will record the fishbone amplitude to be 1. This detection is done manually using the correlated spectrogram method introduced at the beginning of this chapter.

5.4 Sawteeth

The sawtooth instability results in a sudden loss of core temperature corresponding with a sharp rise in temperature outside of the core. Figure 5.8 shows an example of a sawtooth crash observed by the ECE diagnostic. The normalised sawtooth amplitude is taken as the difference in core electron temperature immediately preceding and after the crash event, divided by the initial temperature. The inversion radius is indicated on the right hand side of figure 5.8, defined as the point where the gradient of temperature change goes from negative to positive.

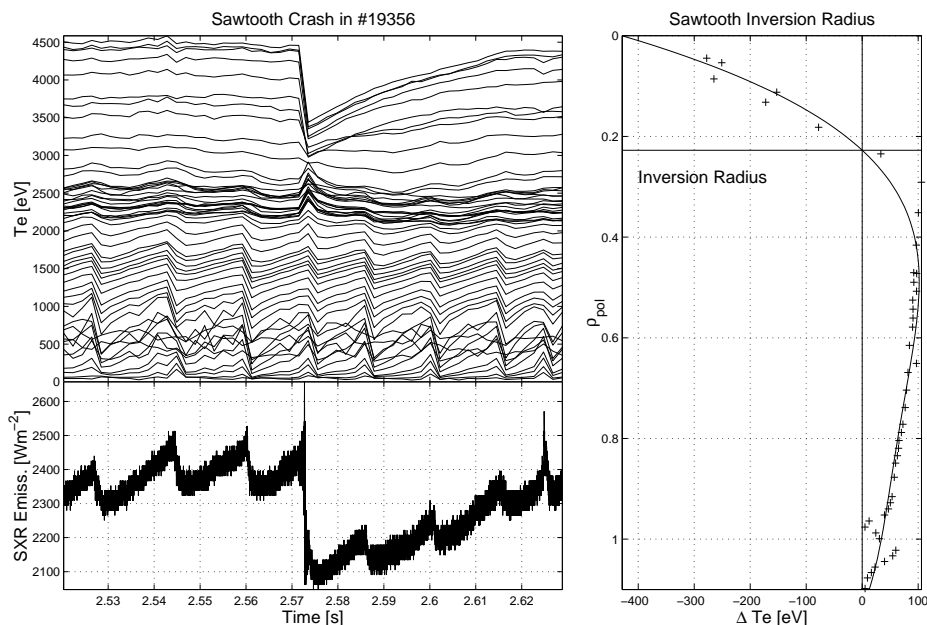


Figure 5.8: The sawtooth instability results in a sharp drop in core temperature coinciding with a sudden rise in temperature outside of the core. This is shown here (left) where the upper line is the core ECE channel, and the lower line shows a time series of an ECE channel outside of the core. The right plot shows the inversion radius. Defined as the point where the temperature change makes the transition from negative to positive gradient.

This analysis is time consuming if it is to be repeated for all sawtooth events in the database. For this reason a sawtooth analysis routine was developed using singular value decomposition (SVD) and a set of empirically

determined parameters to identify and quantify sawtooth events in an automatic fashion.

5.4.1 Sawtooth Detection Algorithm, SAWSCAN

We can treat the different channels of the ECE diagnostic as a matrix, \mathbf{X} , of size $(n \times n_t)$, where n is the number of channels and n_t is the number of

time points. Singular value decomposition was used to filter the T_e profiles [54],

$$\mathbf{X} = \mathbf{U}^T \mathbf{S} \mathbf{V} \quad (5.3)$$

$$x_{ij}^{(k)} = u_{ki} s_k v_{kj} \quad (5.4)$$

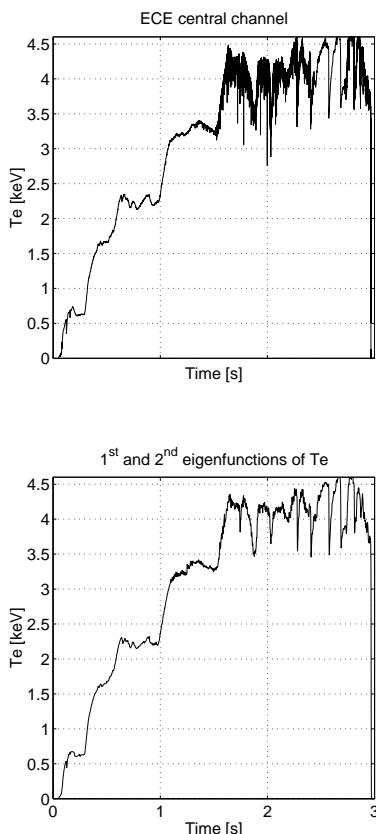
$$\mathbf{X}^{(k)} = (x_{ij}^{(k)}) \quad (5.5)$$

where $\mathbf{X}^{(k)}$ is the k^{th} eigenfunction of \mathbf{X} , and $n_t \geq n$. Figure 5.9 shows the ECE channels overplotted (top), and the same data taking only the sum of the 1st and 2nd SVD eigenfunctions (bottom). It can be seen that SVD has the effect of filtering the data to the sawtooth instability.

The ECE time series are further low-pass filtered to 4 kHz by a Butterworth filter. A sliding time window of data, length $\Delta t = 6.25 \times 10^{-4}$ s is then analysed to determine if it matches the following empirical parameters for a sawtooth crash. This window was chosen to be significantly shorter than the sawtooth envelope so that we have a number of points during the crash and recovery. This is to ensure that

Figure 5.9: The upper figure shows the T_e time series of the central ECE channel. The lower plot shows the same data after SVD, taking only the sum of the 1st and 2nd eigenfunctions.

subtle features such as the increase in T_e outside $q = 1$ are not averaged over and lost. In order to avoid registering different phases of the same event more than once, a criterion is put on the inter-sawtooth period, $\tau_{saw} \geq 0.01$



s. We take the core ECE channel of \mathbf{X} , measuring $T_e(t)$, and the core ECE channel of $\mathbf{X}^{(2)}$, measuring $T_e^{(2)}(t)$. The time derivative of T_e is evaluated to find

the minimum and maximum gradients within the Δt , and their respective time points t_{min} , t_{max} . The following empirical conditions must be met for this time window to be labelled as a sawtooth crash,

$$\min \left[\frac{dT_e}{dt} \right] \leq \begin{cases} -\frac{3}{2} \left[\frac{dT_e}{dt} \right]_{max} \\ 2 \left\langle \frac{dT_e}{dt} \right\rangle \\ -\frac{T_e(t_{min})}{100} \end{cases} \quad (5.6)$$

$$\min \left[\frac{dT_e^{(2)}}{dt} \right] \leq 4 \times 10^6 \text{ eV s}^{-1} \quad (5.7)$$

$$\max \left[\frac{dT_e}{dt} \right] > 0 \quad (5.8)$$

$$\Delta T_e \leq -20 \text{ eV} \quad (5.9)$$

$$t_{min} < t_{max} \quad (5.10)$$

Although the SAWSCAN code can reliably distinguish sawtooth crashes from other events, no set of empirical laws could be found to consistently distinguish a sawtooth crash from the crash features observed during a FIR-NTM. Figure 5.10 shows an example of a sawtooth crash and a FIR-NTM crash. Figure 5.11 shows the result of the SAWSCAN algorithm. Here the ECE channels are over plotted. The dark vertical lines indicate time windows that have satisfied the above conditions.

Sawtooth FIR-NTM disambiguation is done manually by relating suspected sawtooth events to the normalised amplitude of any NTMs present in the same time window. If a rapid loss in NTM

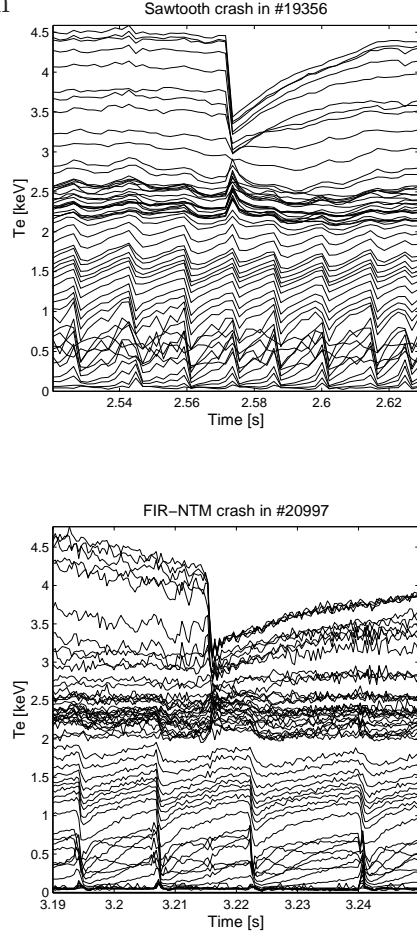


Figure 5.10: This figure shows the crash features observed during a sawtooth and FIR-NTM. No set of empirical laws could be found to consistently distinguish between the two classes of event.

amplitude coincides with the suspected sawtooth crash then it is relabelled as a FIR crash instead.

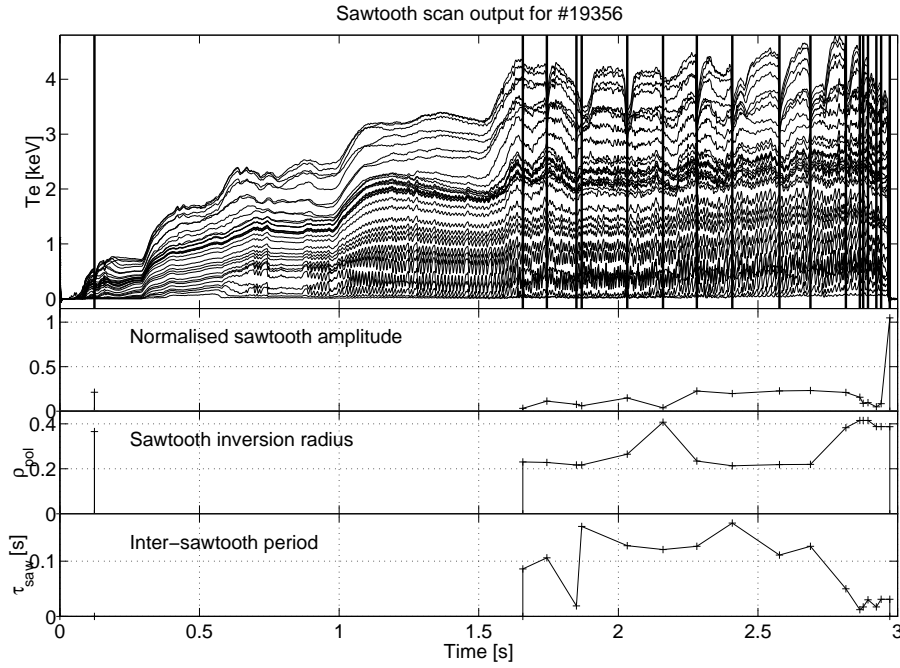


Figure 5.11: This figure shows an example of the SAWSCAN algorithm for sawtooth detection. The ECE channels are over plotted. The dark vertical lines indicate time points that have satisfied the empirical conditions for a sawtooth crash.

In principle there are two distinct classes of sawtooth: Those with and intersawtooth period $\tau_{saw} \gg \tau_E$ and those with $\tau_{saw} \leq \tau_E$. In practice we find that sawteeth in improved H-mode discharges always have $\tau_{saw} \gg \tau_E$ after the L to H transition. In chapter 2.3.6 we discussed the significance of the two classes. Sawteeth with $\tau_{saw} \leq \tau_E$ will interrupt the recovery of the plasma kinetic profiles, thereby limiting the maximum achievable plasma pressure. This is not the case for sawteeth with $\tau_{saw} \gg \tau_E$.

The database defines two types of sawtooth time slice. The first is a time slice within the sawtooth envelope, i.e. after the crash but before the recovery of the plasma kinetic profiles. The second type includes time slices that do not necessarily contain a sawtooth crash but which are between two subsequent sawtooth events. These events can be up to 500 ms apart.

Chapter 6

Onset Criteria and Characterisation of MHD Instabilities in Improved H-Mode

The goal of this thesis is to better understand the mechanisms giving rise to MHD instabilities, to characterise their behaviour, and ultimately to determine their role in the improved H-mode scenario. In this chapter we will discuss the conditions under which the NTM, FIR-NTM, fishbone and sawtooth instabilities appear. We will then use the improved H-mode database, described in the previous section, to quantitatively test and constrain the existing models for these instabilities. Additionally, we will use the newly implemented SXR tomography program to study and characterise the sawtooth instability.

6.1 Neo-classical Tearing Modes

In this section we will investigate the onset conditions of NTMs in improved H-mode plasmas. The goal is to use the NTM onset conditions to learn about the background plasma and to test the Rutherford equation (2.34). In

chapter 2.3.3 and 5.2 we discussed the distinction between P and SNTMs.

PNTMs are triggered by sawtooth or fishbone precursor event, which forms large seed islands in the plasma. These seed islands are typically larger than w_{min} (defined as the minimum island size to result in a positive dw/dt).

SNTMs are triggered without the aid of a precursor event, growing from much smaller seed island sizes at the detection limit of the Mirnov coil diagnostic. SNTM onset occurs for relatively high values of poloidal β , when the value of w_{min} matches the seed island size, w_{seed} , i.e. $w_{seed} \approx w_{min}$, see figure 2.5. In chapter 5.2 we used this relationship to positively identify SNTM modes using by comparing the measured ratio of seed to saturated island size w_{seed}/w_{sat} with the ratio predicted by the Rutherford equation. It was found that the measured and expected ratios matched well for (3,2) SNTMs.

Experimentally it is rarely possible to determine absolute island sizes for NTMs due to the limited temporal and core-spatial resolution of the ECE diagnostic. This becomes especially difficult for measuring w_{seed} as, for SNTMs, it is expected to be significantly smaller than the inter-channel spacing. However, it is still possible to measure the relative island width $w/w_{sat}(t)$ using the integrated Mirnov coil signals, i.e. if we can assume that the radial location of the rational surface is constant with time, then $\int U_{coil} dt \propto B_{pert}$, see equations (3.1, 3.2). We take the maximum achieved island size to be w_{sat} , while w_{seed} is the island size when the mode first appears. We expect the following relations for P and SNTMs,

$$\frac{w_{seed}}{w_{sat}} = \frac{w_{min}}{w_{sat}}, \text{ for SNTM} \quad (6.1)$$

$$\frac{w_{seed}}{w_{sat}} \geq \frac{w_{min}}{w_{sat}}, \text{ for PNTM} \quad (6.2)$$

where we obtain the ratio w_{min}/w_{sat} by solving the Rutherford equation using kinetic profiles and equilibrium reconstructions at the time of the mode onset.¹ Figures 6.2 and 6.3 show two examples of this procedure for a P and SNTM. Here we see that the ratio w_{seed}/w_{sat} almost exactly matches the ratio w_{min}/w_{sat} from the Rutherford equation for the SNTM case. As expected, this relationship does not hold for the PNTM whose initial seed

¹Note that here we are using the Δ' definition from equation (2.36), meaning that this analysis is only strictly valid for (3,2) NTMs as currently no fitting is available for other combinations of (m, n) .

island size is nearly 3 times greater than the value of w_{min} predicted for this time point, presumably growing from a large seed island generated by the sawtooth precursor. This result is significant as it not only allows us to positively identify SNTMs, as discussed in chapter 5.2, but also to estimate the size of naturally occurring seed islands in improved H-mode plasmas using the Rutherford equation.

At this point it may seem reasonable to directly measure the NTM island width during the mode onset using ECE measurements. Unfortunately a direct measurement is not possible due to the limited temporal and spatial resolution of the ECE diagnostic (16 kHz Nyquist and $\simeq 2 \rightarrow 3$ cm inter-channel spacing). Many of the NTMs being studied have frequencies well in excess of 16 kHz and w_{seed} is expected to be much smaller than the inter-channel spacing.

While a direct measurement of w_{seed} may not be possible, it is possible to infer the seed island size using the relationship $w_{seed} \approx w_{min}$ and solving the Rutherford equation for w_{min} using experimental kinetic profiles and equilibrium reconstructions during the SNTM onset phase. Figure 6.1 shows an example of how w_{min} is estimated during the onset of a (4, 3) NTM. Here we find that $w_{seed} \approx w_{min} = 1.07 \pm 0.13$ cm.

Error Analysis

The uncertainty in w_{seed} comes from the uncertainty in a_0 ; the kinetic profiles, the position of the rational surface, and the equilibrium profiles. We generate distribution functions for each of the above terms based on these uncertainties and solve the Rutherford equation for w_{seed} several times using different values within the distribution functions. This results in a mean and standard deviation of w_{seed} values for any given NTM onset.

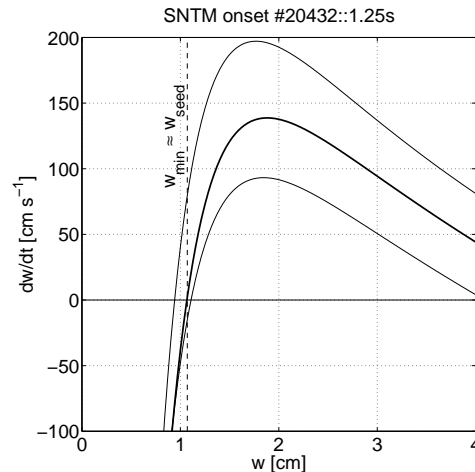


Figure 6.1: This figure shows $dw/dt(w)$ calculated using kinetic profiles and equilibrium reconstructions from the SNTM onset phase. The 3 solid lines show the confidence band in dw/dt due to uncertainties in the equilibrium and kinetic profiles. w_{min} , defined as the minimum island size to give a positive value for dw/dt , is approximately 1.07 ± 0.13 cm.

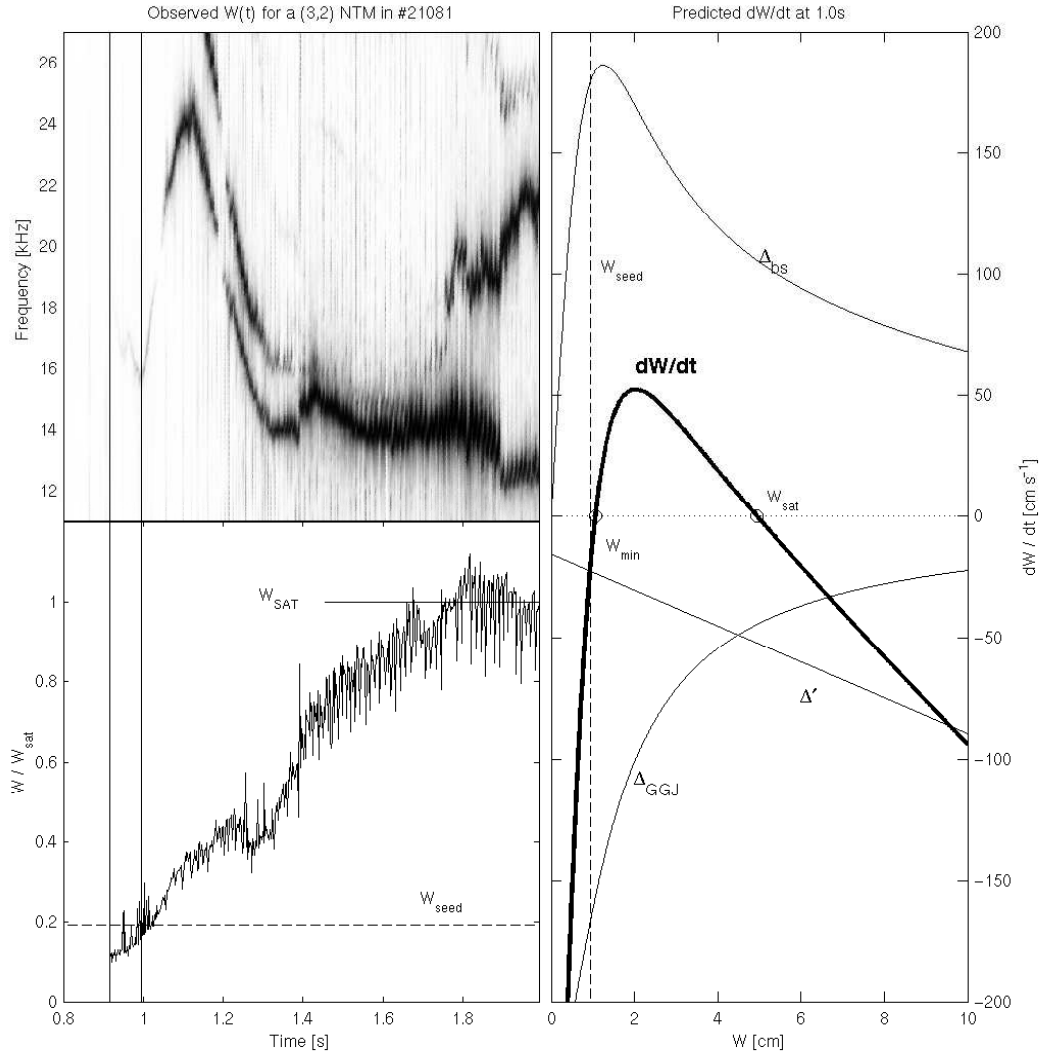


Figure 6.2: The ratio of seed to saturated island size for an SNTM. Note that this ratio almost exactly matches the predicted ratio w_{min}/w_{sat} from the Rutherford equation. This indicates, as we suspected, that the SNTM begins to grow with an island size roughly equal to w_{min} .

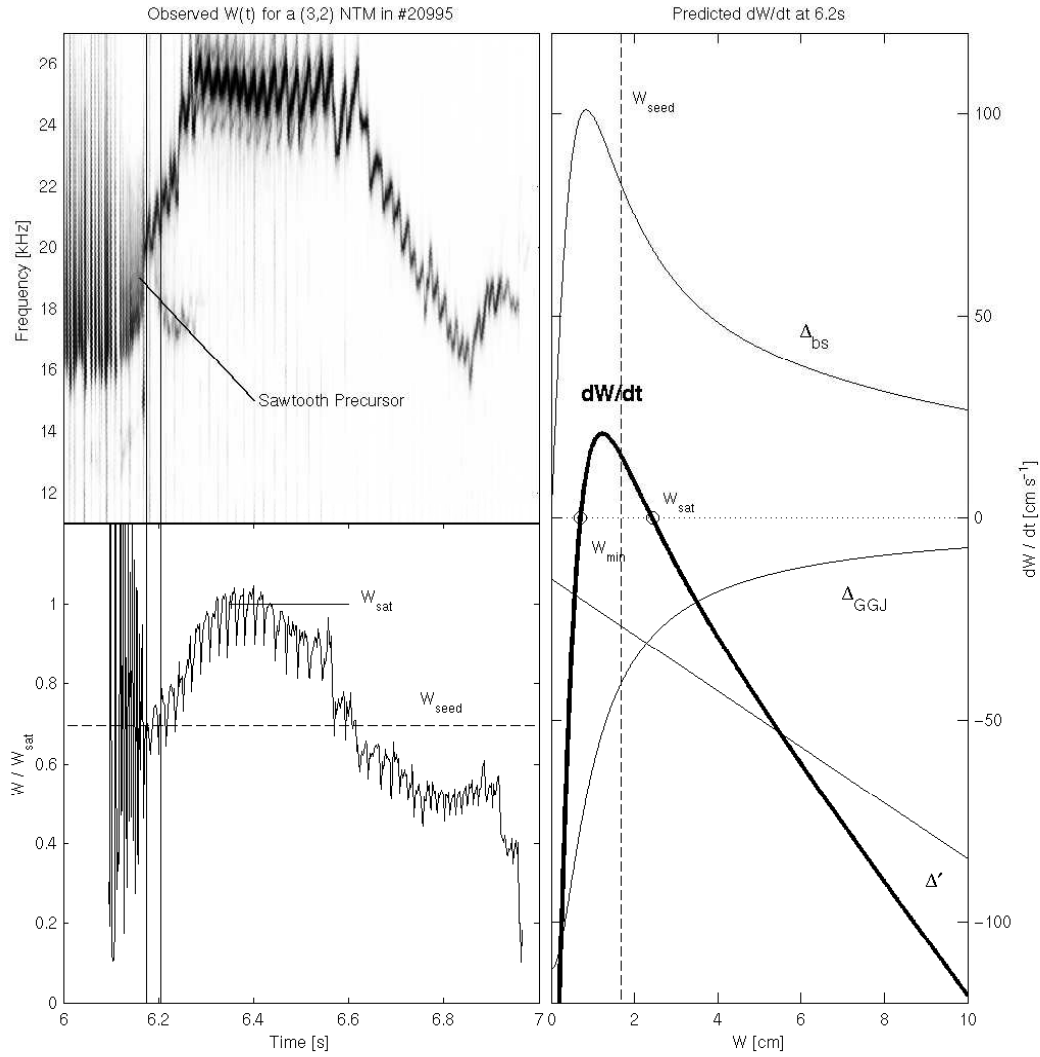


Figure 6.3: The ratio of seed to saturated island size for a PNTM. Unlike the SNTM above, the PNTM begins with a seed island size nearly 3 times greater than the w_{min} predicted by the Rutherford equation. This large w_{seed} is presumably created by the sawtooth precursor.

Figure 6.4 shows the values of w_{seed} found for SNTMs in the improved H-mode scenario. This suggests a mean seed island size of $w_{seed} = 0.95 \pm 0.40$ cm

in the absence of sawtooth or fishbone precursor events. This result has been confirmed for a small number of shots using ECE and integrated Mirnov coil measurements to infer the seed island size. An example is shown in figure 6.5. SNTMs were chosen with saturated island sizes large enough to be visible for the ECE diagnostic and mode frequencies less than 16 kHz, for example the (3, 2) NTM in #21081:

A saturated island size of $w_{sat} = 6.5 \pm 2.4$ cm was measured with the ECE diagnostic. The integrated Mirnov coil signal for this mode shows that the seed island is between 15% \rightarrow 23% of the saturated island size.² This gives a seed island size of $w_{seed} = 1.3 \pm 0.7$ cm, which is in good agreement with the study above.

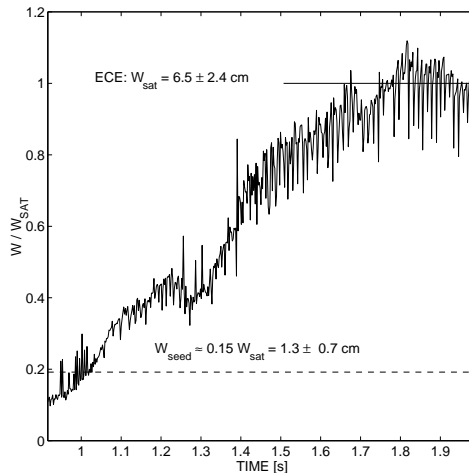


Figure 6.5: This figure shows the seed island size for a (3, 2) SNTM in shot #21081 inferred using the relative island size from the magnetics and a measurement of the saturated island size using the ECE diagnostic. We find $w_{seed} = 1.3 \pm 0.7$ cm.

6.2 The Frequently Interrupted Regime

The Rutherford equation can be fit to predict the onset of normal regime NTM. However, for the Frequently Interrupted Regime NTM an additional β_N threshold must be reached to destabilise the infernal mode. Figure 6.6 shows the distribution of NTM/FIR-NTM onsets with respect to the plasma β_N . Here it can be seen that unlike normal regime NTM, FIR-NTM have a sharp onset threshold at $\beta_N > 2.00$. Figure 6.8 shows an example of a $\beta_N > 2.0$ FIR-NTM onset. The upper plot shows a correlated spectrogram featuring (1, 1) fishbones, an intermittent (4, 3) mode and a (3, 2) NTM going into the FIR regime. The lower plot shows time series of normalised NTM amplitude and β_N .

²We can only use the integrated Mirnov signal to infer relative island sizes if we assume that the position of the rational surface remains constant, see chapter 2.3.3.

This value is slightly lower than the β_N threshold found in previous studies [17]. This can be explained by the characteristic improved H-mode q profile. The central magnetic shear is low compared to standard H-mode discharges and low magnetic shear at the $(m+1, n+1)$ surface reduces the plasma stability against the ideal infernal mode. However, this alone does not necessarily lower the threshold of the FIR transition, as a low global magnetic shear would also increase the separation of the (m, n) and $(m+1, n+1)$ rational surfaces, see figure 6.7 (left).

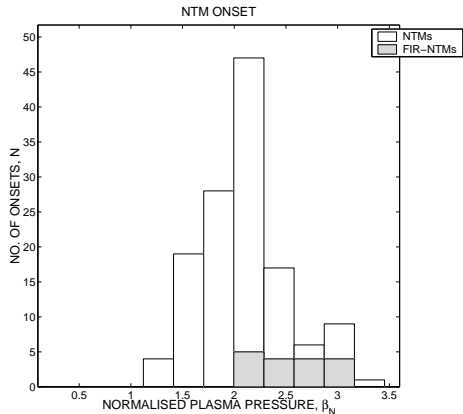


Figure 6.6: This figure compares the distribution of NTM and FIR-NTM onsets with respect to the plasma β_N . FIR-NTMs have a sharp onset threshold $\beta_N \gtrsim 2.0$.

This not only increases the perturbation amplitude required for the modes to overlap and interact stochastically, but it has also been shown that the plasma stability against the ideal ballooning mode is significantly reduced in the presence of a magnetic island, [55].

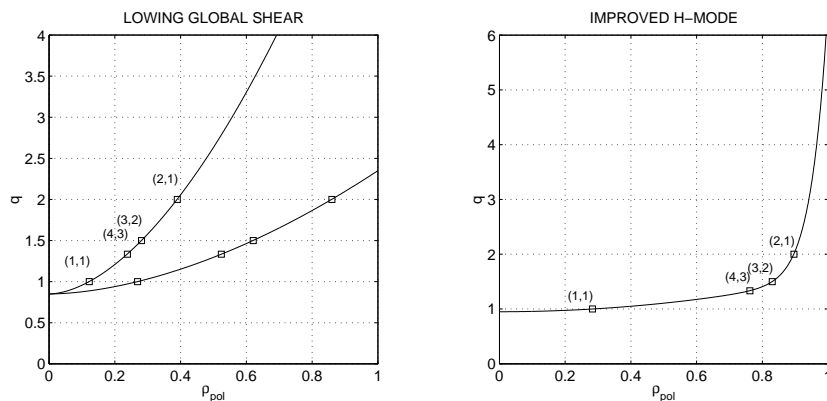


Figure 6.7: Lowering the global magnetic shear increases the separation between the (m, n) and $(m+1, n+1)$ resonant surfaces (left). However, for the characteristic improved H-mode q profile it is possible to have a low magnetic shear at the $(m+1, n+1)$ surface without necessarily increasing the radial separation between it and the (m, n) rational surface (right). Note that these profiles are only illustrative. While the righthand profile is realistic, the lefthand profiles would not have such high shear, but would nevertheless show the same trend in ohmic and standard H-mode discharges.

Although this not exactly same kind of ideal instability, we assume that this effect will hold true for the infernal mode as well. As the radial separation of the two rational surfaces increases, the plasma becomes effectively more stable against the infernal mode. Now consider the characteristic improved H-mode q profile, with low central magnetic shear, rising sharply in the outer half of the minor radius to the separatrix. In this scenario it is possible for the magnetic shear at $q = (m + 1)/(n + 1)$ to be low without increasing the separation between the two resonant surfaces, see figure 6.7 (right). For this reason we expect, and indeed observe, a lower β_N threshold for the FIR transition in the improved H-mode scenario compared to standard H-mode discharges.

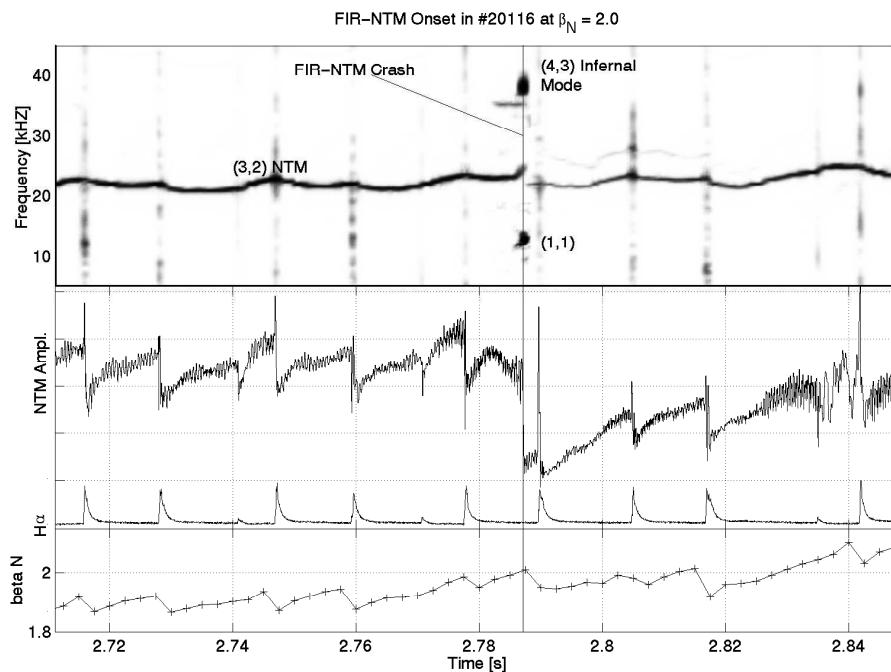


Figure 6.8: This figure shows a FIR-NTM onset occurring at $\beta_N \simeq 1.75$. The characteristic features are labelled in the correlated spectrogram (top). Here (1, 1) fishbones, an intermittent (4, 3) instability, and a (3, 2) NTM enter into the phase locking condition as the FIR crash occurs, i.e. $\omega_{(3,2)} = 2\omega_{(1,1)}$, $\omega_{(4,3)} = 3\omega_{(1,1)}$. Coinciding with this convergence is a sharp drop in the normalised NTM amplitude. The NTM has entered the FIR regime. The other smaller crash features can be attributed to ELM events, visible as spike-like features in the H_α signal, shown at the bottom of the second plot.

6.3 The Fishbone Instability

The fishbone instability requires the presence of the $q = 1$ rational surface, and a sufficient fast particle pressure, β_{fast} , in the core. It has been observed that this threshold is $\beta_{fast} \geq 0.009$ for H mode discharges [56]. We estimate β_{fast} due to neutral beam ions using the *ion slowing down time*, τ_{sd} ,

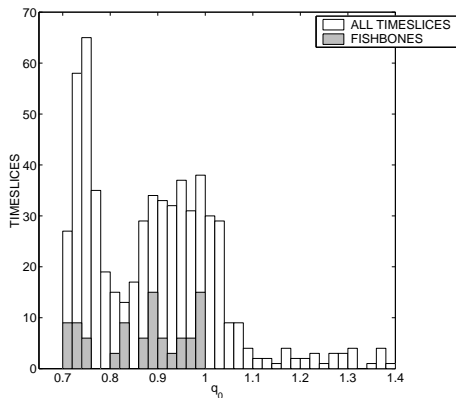


Figure 6.9: The occurrence of the fishbone instability in terms of q_0 .

$$\beta_{fast} = \frac{\beta_{tor}}{1 + \frac{\tau_E}{\tau_{sd}}} \quad (6.3)$$

$$\tau_{sd} = 6.2 \times 10^8 \frac{T_e^{3/2}}{n_e \ln \Lambda} \quad (6.4)$$

where $\ln \Lambda = 17$ for ASDEX Upgrade. τ_E is the appropriate confinement time scaling. In [56] an H mode scaling was used. The central q value, q_0 , is typically an unreliable quantity as there is often very little information with which to constrain the CLISTE equilibrium code in the plasma core. Therefore, only time slices for which the MSE diagnostic was

available were used for determining the fishbone onset conditions. Figures 6.9 and 6.10 show that fishbones are only observed for, $q_0 < 1.0$ and $\beta_{fast} > 0.0075$. This β_{fast} onset condition is slightly lower than the value found for standard H mode discharges.

In [56] a destabilisation regime was calculated using the above β_{fast} threshold. This regime is shown as the shaded regions in figure 6.11. Each region has been calculated keeping $B_{tor} = -2$ T (right figure) and $n_e = 5 \times 10^{19} \text{ m}^{-3}$ (left figure). The boundary of this region represents the $\beta_{fast} = 0.009$ threshold at $I_P = 0.6$ MA. Timeslices with $n_e \approx 5 \times 10^{19} \text{ m}^{-3}$ and $B_{tor} \approx -2$ T from the improved H-mode database are shown overlaid. Note that fishbones are found at slightly lower core temperatures than predicted for the standard H-mode regime. This is consistent with the lower β_{fast} threshold.

6.3.1 Suppression by NTMs

It has been observed that the presence of an NTM in the plasma can suppress (1, 1) activity, such as a reduction in the rate of Sawtooth reoccurrence and,

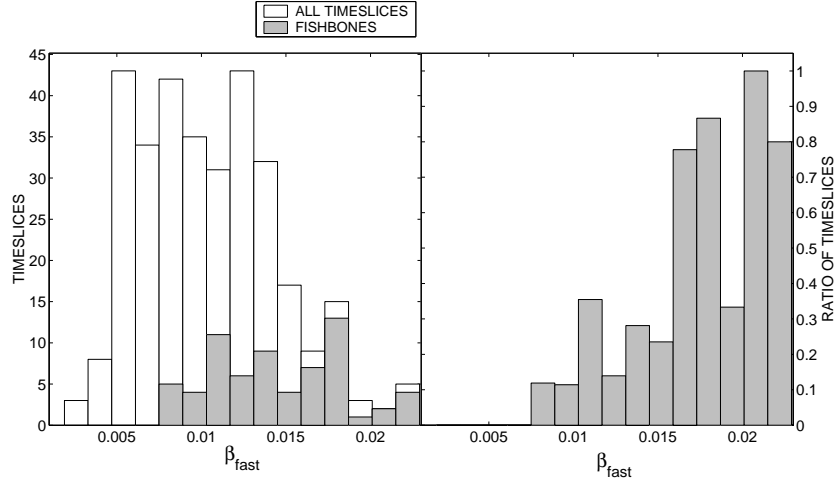


Figure 6.10: The occurrence of fishbones in terms of the core β_{fast} .

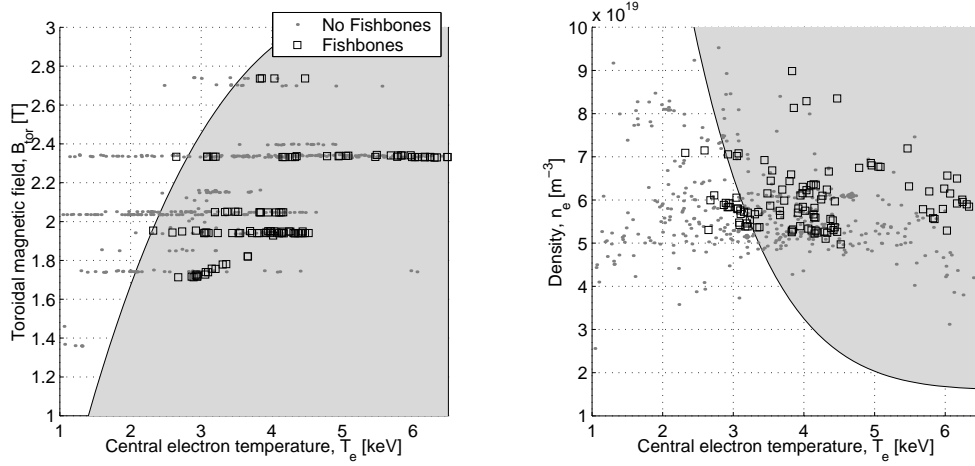


Figure 6.11: The shaded regions represent the fishbone destabilisation regime found for the standard H-mode. The boundary of this region represents the β_{fast} threshold. The Timeslices from the improved H-mode database are shown overlaid. Note that fishbones are found at slightly lower core electron temperatures than predicted by this regime. This suggests a lower β_{fast} threshold.

in some cases, total suppression of the fishbone instability [35].

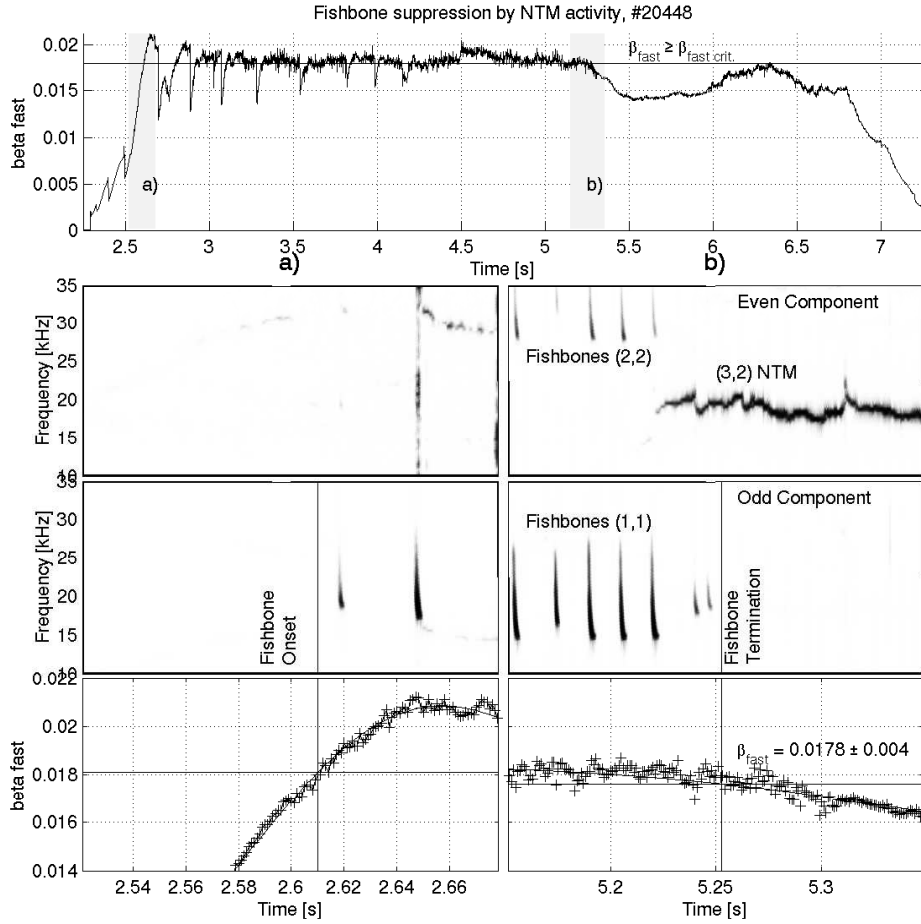


Figure 6.12: Fishbone bursts are observed after 2.7 s as the core β_{fast} exceeds the threshold value β_{fast}^{crit} . They continue until 5.2 s, when the onset of a (3, 2) NTM causes a rapid drop in β_{fast} , bringing it below β_{fast}^{crit} for this shot.

One theory suggests that a rotating NTM island acts as an antenna which, through the emission of Alfvén waves, drives a negative current through the plasma. This current drive could in turn prevent the central q value dropping below unity [35]. However, the following observations suggest that the NTM suppression of the fishbone instability is due only to the impact of the NTM on the core β_{fast} . Note, the NTM impact on β_{fast} is calculated using profiles

of T_e in equations (6.3, 6.4). This makes the assumption that the NTM affects the fast and thermal particles in the same way. Figure 6.12 shows an example where, as a result of the onset of a (3,2) NTM, the value of the core β_{fast} drops below the threshold value of β_{fast} at which the fishbone instability was first observed in this discharge. At the same time point the fishbone instability vanishes.

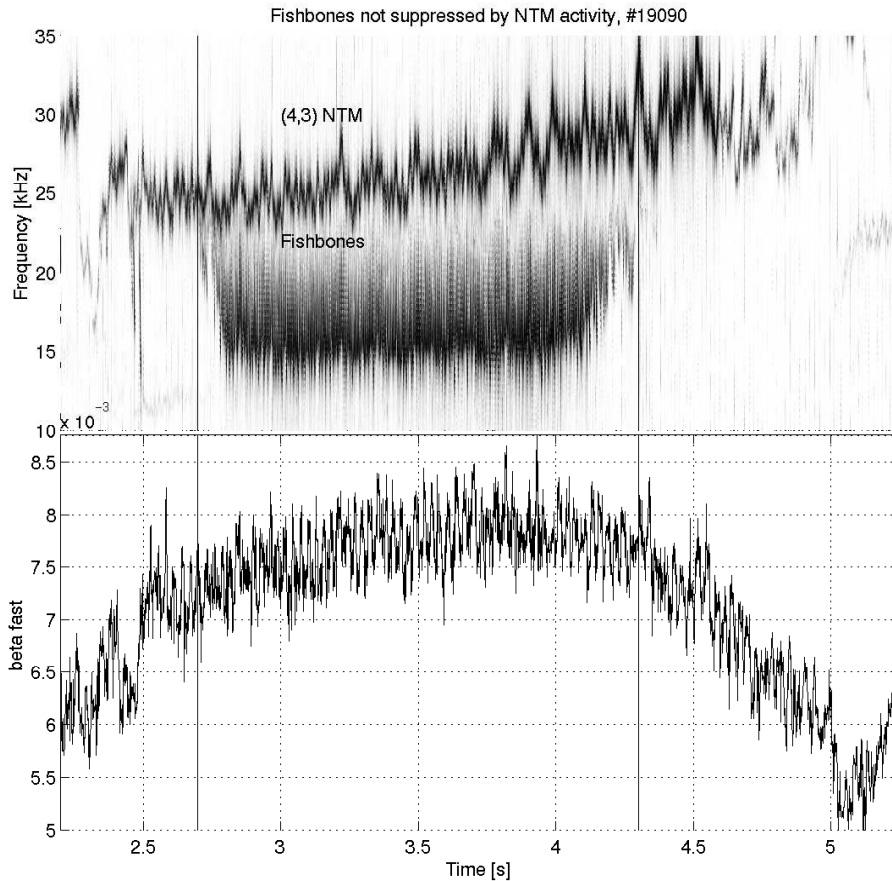


Figure 6.13: In this example fishbone bursts continue throughout the onset and much of the duration of a (4,3) NTM as this NTM fails to sufficiently degrade the core β_{fast} value. This allows the NTM and fishbone activity to coexist until roughly 4.3s when the core β_{fast} drops below the critical value for this discharge. At this point the fishbone bursts stop abruptly.

This matches observations by the Fast Ion Loss Detector (FIL) on ASDEX Upgrade, where NTMs have been shown to have a strong impact on

the fast particle population [57]. In cases where the NTM does not have a significant impact on the core β_{fast} , such as the (4, 3) NTM shown in figure 6.13, the fishbone instability is not suppressed.

6.3.2 Suppression by a Sawtooth Crash

Observations show that a sawtooth crash temporarily suppresses fishbone activity. In the *total reconnection sawtooth model* this is explained by the central q_0 being raised above unity as a result of the crash [23]. This loss of the $q = 1$ surface effectively suppresses the fishbone instability. The q profile can return below unity after a time interval Δt . This is of the order of the current diffusion time, τ_{diff} . The radius of the $q = 1$ surface during this time window is approximately 12.5 cm. This gives a current diffusion time of $\tau_{diff} \approx 0.5$ s, from equation (2.33).

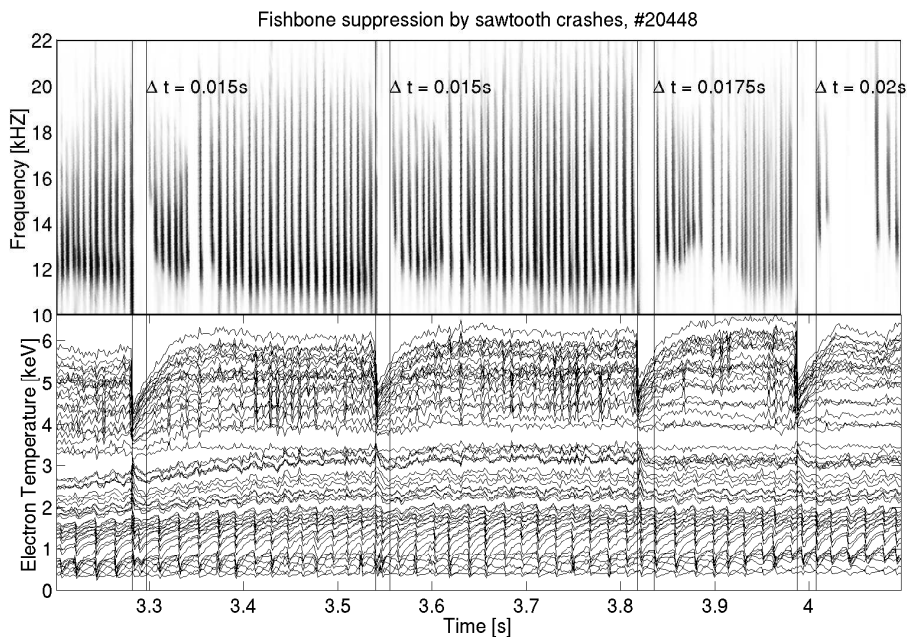


Figure 6.14: Fishbone recovery times after a sawtooth crash are nearly 2 orders of magnitude less than the current diffusion time. This suggests that the q_0 did not raise above unity as a result of the sawtooth crash.

However, in the improved H-mode database, fishbone bursts are regularly observed after a sawtooth crash within 0.015 s, as shown in figure 6.14, which

is nearly 2 orders of magnitude less than τ_{diff} . This suggests that if the q_0 was raised above unity, it has returned nearly 100 times faster than expected.

In the *partial reconnection sawtooth model* the $q = 1$ surface remains in the plasma after the sawtooth crash [27]. This would explain not only why the fishbone instability is able to recover so quickly after the crash, but also why in many cases (1,1) activity is observed before, during, and after the sawtooth crash. In this model the temporary cessation of the fishbone bursts is explained by the sawtooth impact on the core fast particle population. The sawtooth crash reduces the core β_{fast} below the fishbone threshold value and the fishbone bursts cease. Figure 6.15 shows that fishbone bursts are observed as soon as the β_{fast} recovers to the $\beta_{\text{fast}}^{\text{crit}}$ value for this discharge.

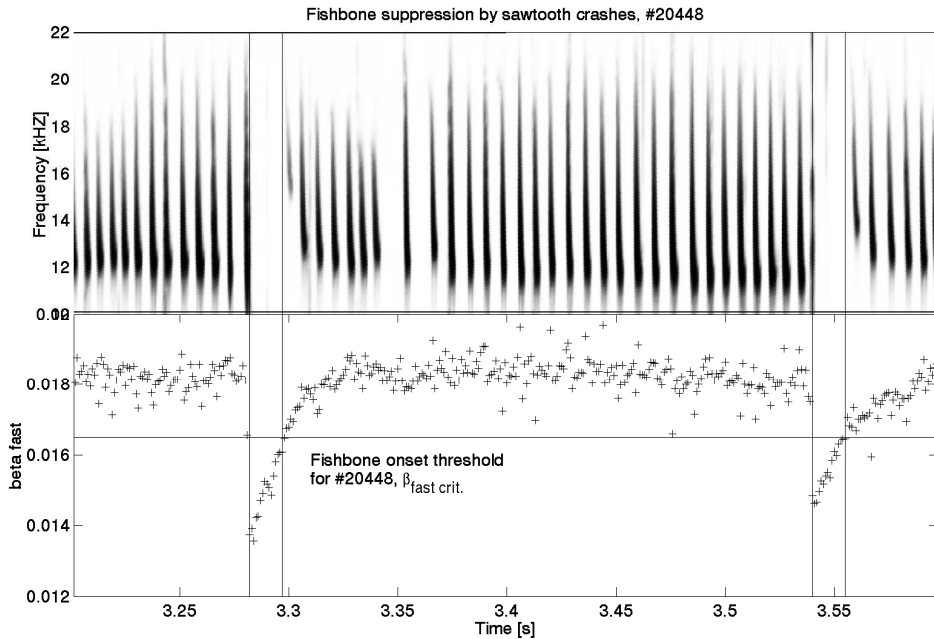


Figure 6.15: In the scenario where the $q = 1$ surface survives the sawtooth crash, the temporary cessation of the fishbone instability can be explained purely by the loss of core β_{fast} . The crash causes a sharp loss in the core β_{fast} which brings it below the threshold value required for the fishbone instability in this discharge, $\beta_{\text{fast}}^{\text{crit}}$. Fishbone bursts are observed again as soon as the core β_{fast} recovers to $\beta_{\text{fast}}^{\text{crit}}$.

It is important to note that the initial loss in β_{fast} is not due to the τ_{sd} dependence on the electron temperature (6.4), but that the sawtooth crash

ejects fast particles from the core. In this discharge the flat-top $T_e = 3$ keV, and $n_e = 6 \times 10^{19} \text{ m}^{-3}$ which gives $\tau_{sd} \approx 10$ ms. In order to see the effect of changing T_e on β_{fast} we must wait for at least a time interval of τ_{sd} in order to calculate β_{fast} with equation (6.3). This means we cannot calculate β_{fast} for the crash phase or for 10 ms afterwards. Equation (6.3) becomes valid again for the recovery phase, which lasts roughly 30 ms, and accurately predicts the reappearance of the fishbone instability.

6.4 The Sawtooth Instability

The sawtooth instability requires $q_0 < 1.0$, and magnetic shear at the resonant surface, $s \geq s_{crit}$, from the Porcelli criterion, equation (2.49). Figure 6.16 shows the evolution of the local shear at the $q = 1$ surface with respect to the critical shear required to destabilise sawteeth. As soon as $s(r_s)$ increases above $s_{crit}(r_s)$ sawteeth are observed.

In chapter 2.4 we discussed the hypothesis that sawtooth and fishbone reconnection may play a role in maintaining the flattened q profile characteristic of improved H-mode discharges. In figure 6.16 there is an indication that such an interaction may be taking place. Note that the evolution of the local magnetic shear stops abruptly as soon as the sawtooth instability is observed, with $ds(r_s)/dt \approx 0$. This discussion will be carried further in chapters 7.2 and 8.1.

The left hand side of figure 6.17 shows sawteeth have only been observed for $q_0 < 1.0$, as expected, while the right hand figure shows a scatter plot of time slices containing a $q = 1.0$ surface, and the difference between the local and critical shear at the resonant surface, $s_1 - s_{crit}$. Here it can be seen that sawteeth are only observed when the local shear exceeds s_{crit} . Only those time slices for which the MSE diagnostic was available were used in this analysis.

This figure clearly shows that sawteeth are not observed for local shear below the onset criterion $s_1 > s_{crit}$. However, not all timeslices which satisfy the Porcelli criterion contain sawteeth. It has been proposed that reconnection is triggered only when the following additional criterion is satisfied [58],

$$c\rho \frac{s_1}{r_s} > \delta W \quad (6.5)$$

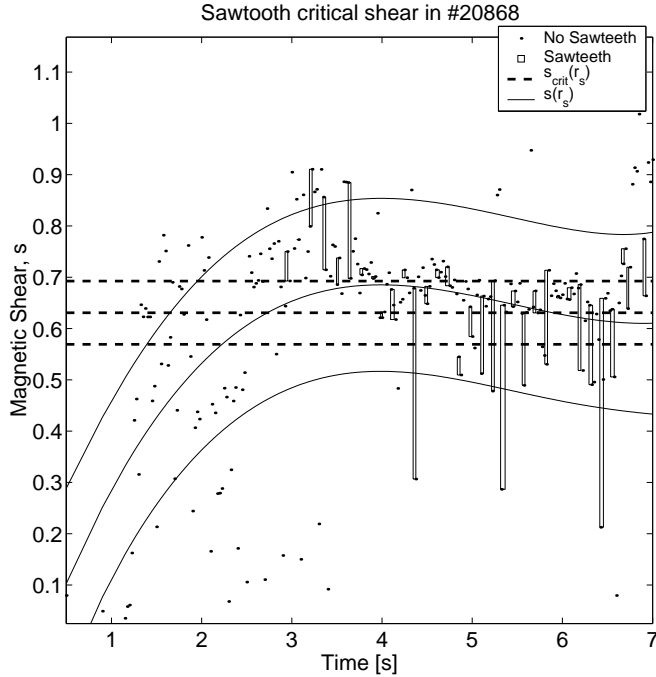


Figure 6.16: This figure shows the evolution of the local magnetic shear at the $q = 1$ surface with respect to the critical shear required to destabilise sawteeth. The critical shear has been averaged over the discharge. For both the critical and local shear the 3 lines represent the mean and \pm standard deviation. As soon as $s(r_s) \geq s_{crit}(r_s)$ sawteeth are observed. It is interesting to note that $ds(r_s)/dt$ drops abruptly to $ds(r_s)/dt \approx 0$ as soon as sawteeth are observed. The 3 solid lines show the confidence band based on uncertainties in the equilibrium reconstruction.

where c is a normalisation coefficient, s_1 is the local shear at the $q = 1$ surface with radial location r_s . δW represents the ideal potential energy. Both energetic ions and toroidal rotation act to increase δW thereby increasing the plasma stability against the sawtooth [59, 60]. A full quantitative model for sawtooth stabilisation is still the subject of ongoing research.

6.4.1 Compound Sawteeth

The *compound sawtooth crash* is a variant of the typical sawtooth crash, where a sudden relaxation of the temperature profile is observed preceding the main crash. This initial relaxation does not result in a drop in the central

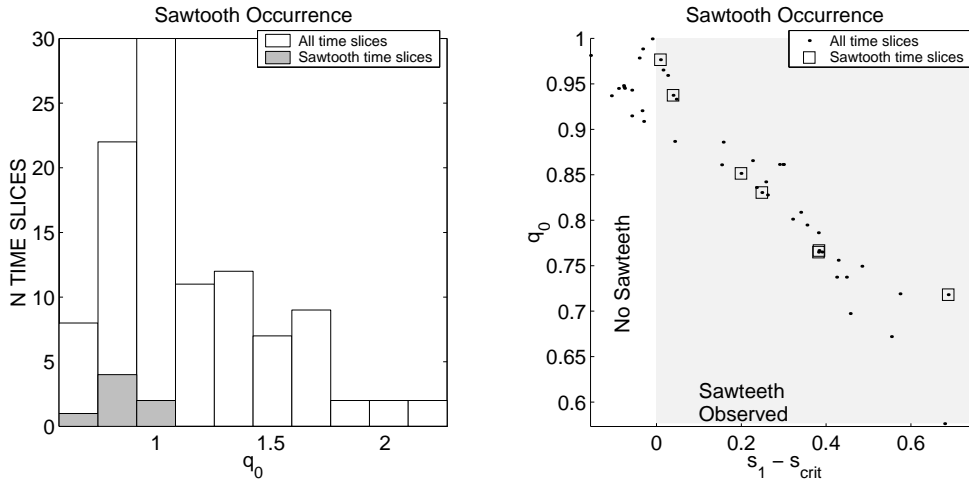


Figure 6.17: The left hand side compares two histograms of q_0 . The white histogram shows all improved H mode containing MSE information, while the grey shows the subset of those time slices which contain sawteeth. Here it can be seen that sawteeth are only observed for $q_0 < 1.0$. The right hand side shows a scatter plot of q_0 and the difference between the local and critical shear at the $q = 1.0$ surface, $s_1 - s_{crit}$. Here it can be seen that sawteeth are only observed for $s_1 > s_{crit}$.

temperature, but occurs in a localised region just outside of the core. In the compound sawtooth crash model the initial crash is caused by a reconnection between two $q = 1$ surfaces in the plasma, i.e. there must be an inversion in the q profile close to $q = 1$ [61]. This inversion requirement suggests a low shear in the central q profile with a q_0 close to unity. The upper plot in figure 6.18 shows an example of several successive compound sawteeth, where the initial crashes have been highlighted in grey. The lower part of figure 6.18 shows how the electron temperature profiles change as a result of both the initial and main crash events. Such events are observed regularly in the improved H mode database, which suggests that many improved H mode discharges have a flat central q profile close to unity.

The compound sawtooth crash is seen most clearly on the ECE diagnostic. However, it is also faintly visible on the SXR diagnostic. A simple model of the compound sawtooth was compared with the observed SXR signals using the SXR tomography program described in chapter 4. The equations below give the perturbed emissivity profiles as a result of the initial crash, $\varepsilon_{init}(r)$,

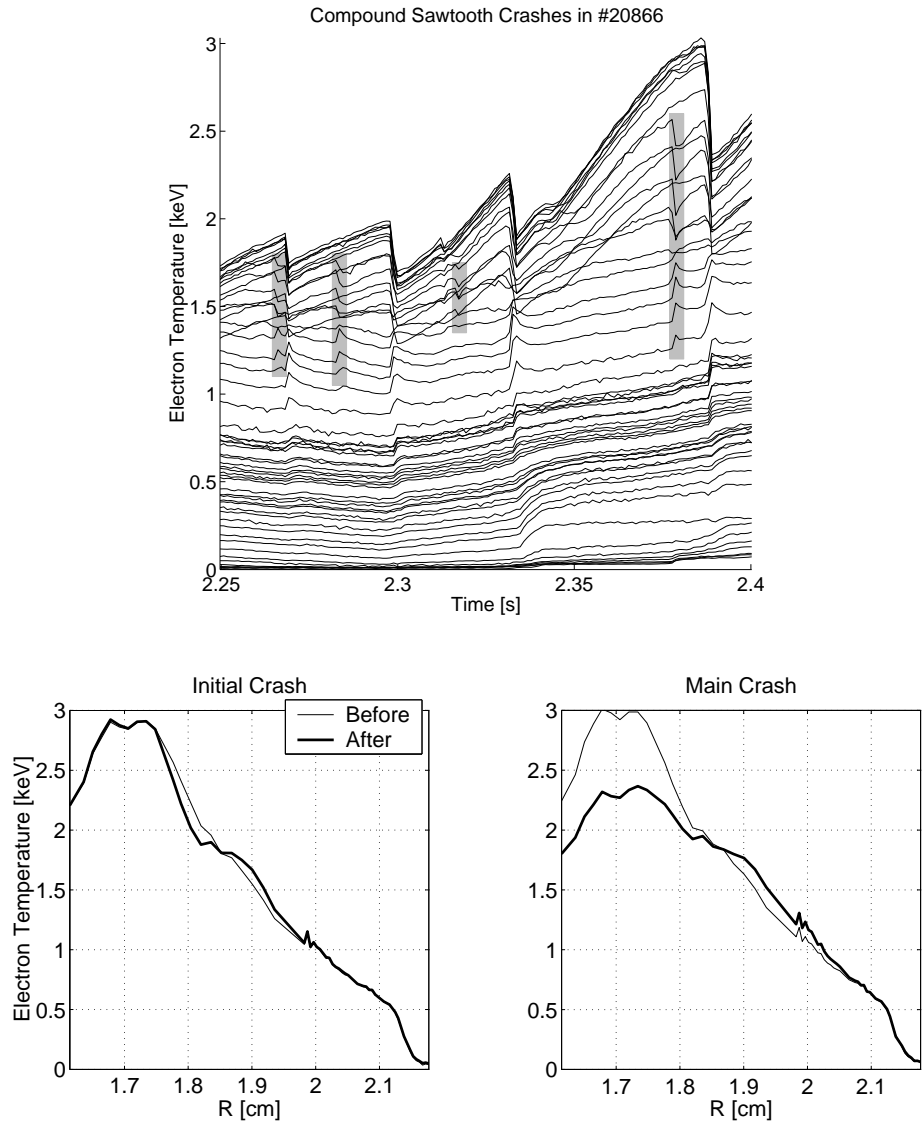


Figure 6.18: An example of compound sawteeth observed during an improved H mode discharge on ASDEX Upgrade. The initial crash features have been highlighted in grey. The initial crash occurs close to the inversion radius of the main crash. This initial relaxation is relatively localised and does not have an impact on the central plasma temperature.

and the main sawtooth crash, $\varepsilon_{main}(r)$,

$$\varepsilon = \varepsilon_0 e^{-(r/a)^2}, \text{ before crash} \quad (6.6)$$

$$\varepsilon = \varepsilon_0 \left[e^{-(r/a)^2} - c_i e^{-\left(\frac{r/a - r_0/a + \lambda_i}{\lambda_i}\right)^2} + c_i e^{-\left(\frac{r/a - r_0/a - \lambda_i}{\lambda_i}\right)^2} \right], \text{ initial crash} \quad (6.7)$$

$$\varepsilon = \varepsilon_0 \left[e^{-(r/a)^2} - c_1 e^{-\left(\frac{r/a}{\lambda_1}\right)^2} + c_2 e^{-\left(\frac{r/a - r_0/a - \lambda_2}{\lambda_2}\right)^2} \right], \text{ main crash} \quad (6.8)$$

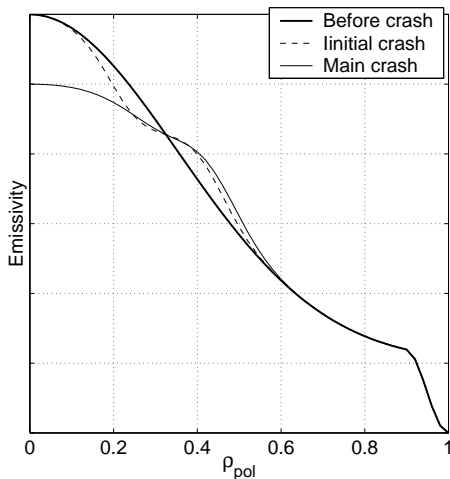


Figure 6.19: This figure shows a basic model of the compound sawtooth crash using equations (6.6) to (6.8).

where $c_2 < c_1$ and $\lambda_2 < \lambda_1$. The resulting emissivity functions are shown in figures 6.19 and 6.20. This simple poloidally symmetric model is based on the observed evolution of the T_e profile shown in figure 6.18, using the assumptions $dn_e/dt \approx 0$, and $dZ_{eff}/dt \approx 0$, $\Rightarrow P_{rad,SXR} \propto \sqrt{T_e}$.

The signals predicted by the SXR tomography program, given the above model, qualitatively match the observed SXR signals. One such comparison is shown in figure 6.20. This could not be verified using a full reconstruction due to the low number of SXR sight lines available for these shots. In the future it will be possible to reconstruct a compound sawtooth crash with maximum entropy tomography.

6.4.2 Reconstructions Using SXR Tomography

In the past the low number of SXR sight lines made it impossible to reconstruct MHD activity using maximum entropy regularisation alone. Additional virtual sight lines were generated by assuming we are observing a single perturbation rotating with angular frequency, ω , see chapter 4.3.

While this assumption can be used to reconstruct MHD activity preceding and following the sawtooth crash, it cannot be used to reconstruct the crash

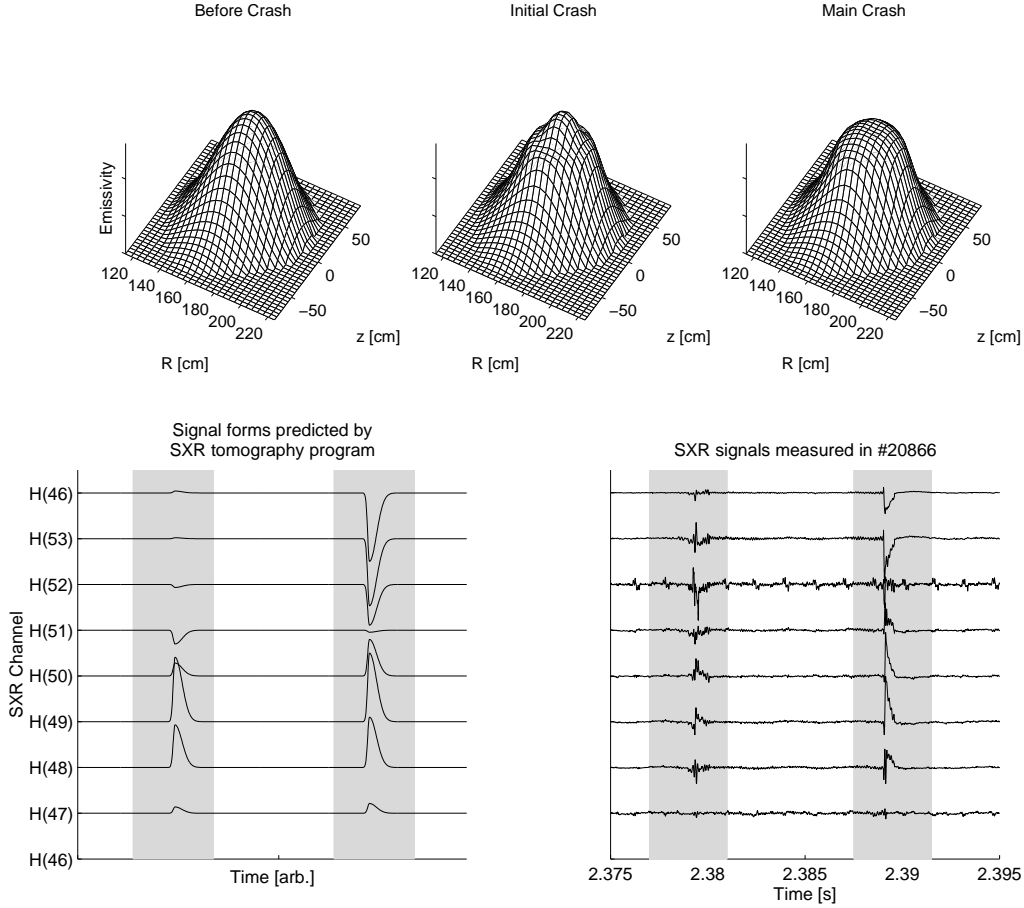


Figure 6.20: The upper plots show a simple model for the perturbed SXR emissivity profiles resulting from a compound sawtooth crash. The initial crash is a relaxation outside of the core, and does not result in a significant loss of emissivity in the core. The main sawtooth crash results in a sharp drop in core emissivity. These models were generated for the SXR tomography program using equations (6.6) to (6.8) with $r_0/a = 0.4$, $c_i = 0.05$, $\lambda_i = 1/12$, $c_1 = 0.1$, $\lambda_1 = 1/4$, $c_2 = 0.05$, and $\lambda_2 = 1/10$.

The lower plots show the compound sawtooth signals predicted by the SXR tomography program compared with the observed SXR signals. There is a good qualitative agreement. At most a very weak drop is observed in the central SXR channels during the initial crash, but a noticeable increase in emissivity is seen in channels $H(49)$ to $H(47)$. The main crash has the same form as predicted by the tomography program.

event itself. Some reconstructions were carried out by taking $\omega = \infty$, i.e. by assuming the crash to be poloidally symmetric. This, as it will be shown later, was not a valid assumption.

The recent addition of 3 new cameras to the soft X-ray diagnostic has increased the sight line coverage from an average of 50 working sight lines to over 160. With this increased coverage it is no longer necessary to generate virtual sight lines using rotation assumptions. Figure 6.21 shows reconstructions of the plasma emissivity before and after a sawtooth crash in shot #23074. The peaked central emissivity leaks, by some mechanism, into the plasma outside of the $q = 1$ surface, resulting in a flattened central emissivity profile.

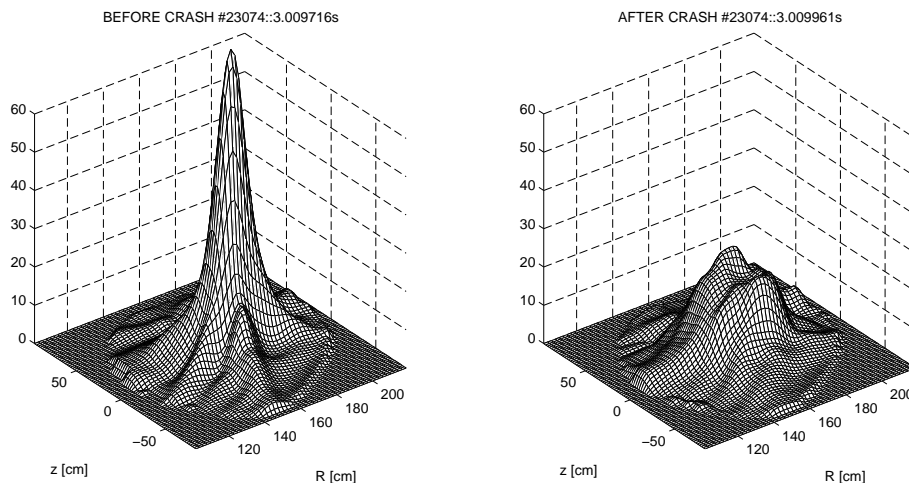


Figure 6.21: A sawtooth crash observed by the SXR diagnostic, reconstructed using maximum entropy tomography.

This process has been repeated for many sawteeth across a range of shots. In each case the signals were low-pass filtered to remove the influence of other MHD activity, including the (1,1) kink instability. What remains is the behaviour of the background plasma emissivity. Reconstructions were made for a time window of 1.5 ms centred on the crash with each frame $25 \mu\text{s}$ apart. Figure 6.22 shows a selection of frames taken from shot #23074: Point a) shows the initial state of the plasma emissivity before the crash. At point b) the central emissivity appears to relax slightly. It will be later shown that this is due to the rapidly increasing displacement of the internal kink instability. After this the crash occurs resulting in the loss of the peaked core emissivity and a rise in emissivity immediately outside of the $q = 1$

surface. However, rather than observing a flattened poloidally symmetric profile we find a noticeable concentration forming on the low-field side, which results in a crescent shaped plume, as seen in c). This feature does not rotate and appears to be independent of the (1, 1) kink mode which continues to rotate through the same region for many periods after the crash. The plume persists for roughly $300 \rightarrow 700 \mu s$ before relaxing into a flattened poloidally symmetric emissivity profile, as seen in d).

Such plume features were observed following all sawteeth reconstructed using SXR tomography across 10 improved H-mode discharges. Though varying in amplitude and radial location, all were located on the low-field side of the plasma and had the same crescent shape.

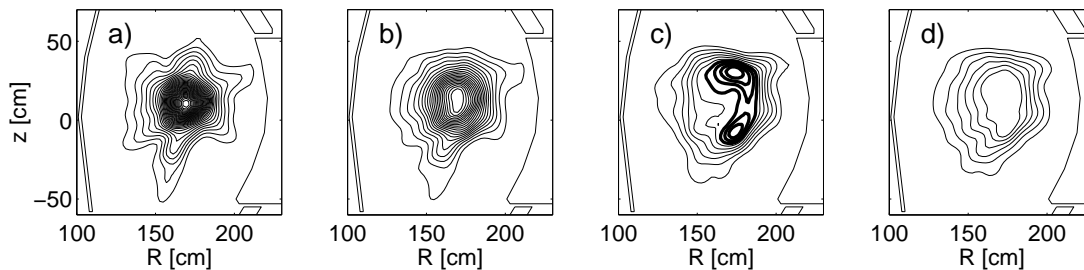


Figure 6.22: This figure shows features observed during a sawtooth crash using SXR tomography. Frame *a*) shows the plasma emissivity before the sawtooth crash. *b*) shows a phase immediately prior to the crash event. Notice how the previously peaked central emissivity has flattened slightly. *c*) shows a phase immediately after the sawtooth event. Notice the pronounced poloidal asymmetry in this frame. A crescent shaped plume of relatively high emissivity can be observed on the low-field side of the central plasma. *d*) this feature relaxes after roughly $300 \rightarrow 700 \mu s$ into a flattened poloidally symmetric emissivity profile.

To better understand these features a series of relatively high time resolution reconstructions ($5 \mu s$) were carried out for sawteeth in shot #23074. No filtering was applied to the data so that the behaviour of the internal kink and its harmonics could be observed. Figure 6.23 *a*) shows the motion of the central plasma column during pre-crash flattening observed in figure 6.22 *b*). Notice that the displacement of the (1, 1) kink increases sharply, resulting in the central plasma column spiralling outwards from $\rho_{pol} \simeq 0.1 \rightarrow \rho_{pol} \simeq 0.4$ within $50 \mu s$. The result is that channels originally observing the central plasma column will now observe the column moving back and forth through

the line of sight. If the signals are time averaged or low-pass filtered below the frequency of the internal kink mode then this oscillatory motion will result in a net decrease in the core signal amplitude. This can be directly observed in the time series of a core SXR channel, see figure 6.23 b). Notice how the maximum value in the unfiltered signals remains more or less constant, while the filtered signals decrease as the kink amplitude increases. It is this decrease in signal amplitude which is responsible for the apparent initial relaxation.

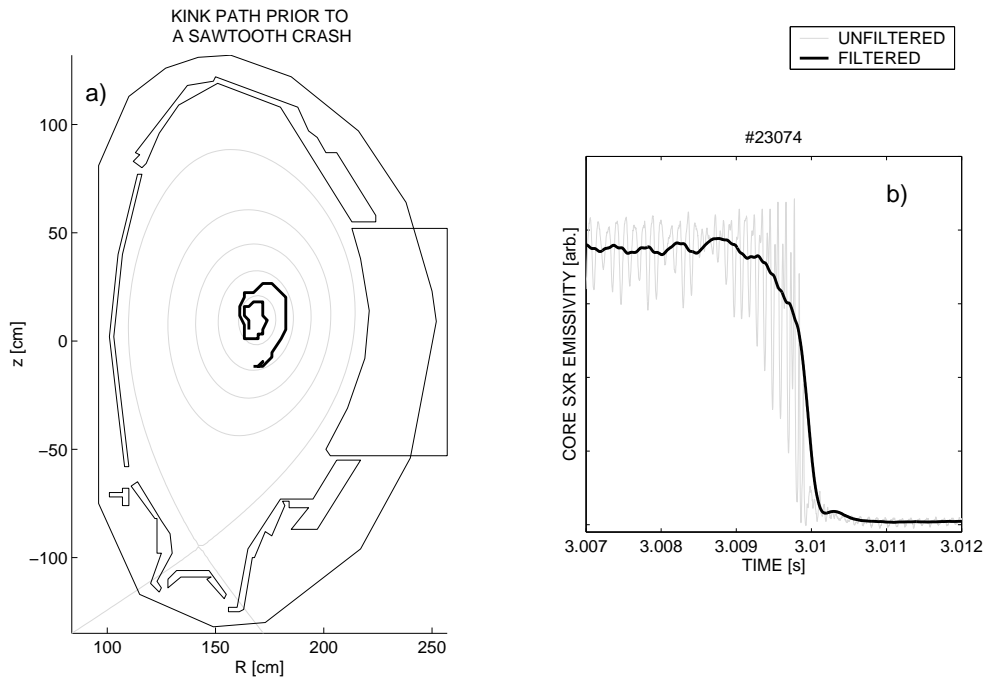


Figure 6.23: This figure shows the path of the central plasma column as the kink displacement increases immediately prior to the sawtooth crash *a*). The central plasma column rapidly spirals outwards. *b*) shows the effect of this increasing displacement on one of the core SXR channels. While the maximum of the unfiltered signals does not decrease, time averaged or low-pass filtered signals will show an apparent reduction in signal amplitude.

As the kink displacement increases, a point is reached where the central plasma column suddenly loses amplitude. This is the crash phase of the sawtooth cycle. The plume feature visible in figure 6.22 c) is first identifiable roughly $80 \mu s$ after the crash. It becomes a stable and prominent feature $300 \mu s$ after the crash, and relaxes over a further $300 \rightarrow 700 \mu s$ into

a poloidally symmetric emissivity profile as shown in 6.22 d).

The existence of the plume feature has been verified using the ECE diagnostic. Electron temperature profiles taken before and after the crash show the same initial shift towards the low field side. The profile is initially asymmetric about the magnetic axis, but this asymmetry relaxes into a flattened symmetric profile after roughly $300 \rightarrow 700 \mu\text{s}$, see figure 6.24.

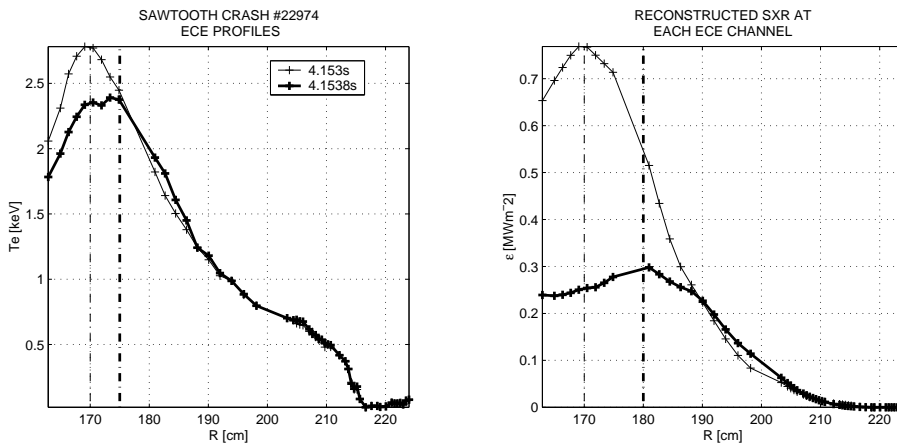


Figure 6.24: The plume feature is also visible on the ECE diagnostic. Note the slight displacement of the ECE temperature profile towards the low field side after the crash (left). Both the crash and plume are more pronounced in the SXR emissivity profile (right).

To explain this feature we look at the power emitted due to Bremsstrahlung radiation,

$$P_{rad,brems.} = c_{brems.} n_e^2 Z_{eff} \sqrt{T_e} \quad (6.9)$$

We can immediately rule out a poloidal gradient in the electron density n_e as density profiles in standard and improved H-mode discharges are characteristically flat [62]. Therefore, we expect no net change in density due to the ejection of the central plasma column. High Z impurities ejected with the plasma column could explain the feature as they would be gyroscopically thrown to the low-field side due to their higher mass. However, the plume feature is also present on the ECE temperature profile which is not sensitive to Z_{eff} .

A poloidal gradient in the electron temperature T_e could be produced by the sawtooth crash as the central T_e profile is always strongly peaked prior to the crash. Classically we expect any gradient along a flux surface to relax on the time scale of the ion sound speed. If this were the case we would expect such a feature to relax within $1 \rightarrow 10 \mu s$. However, if the temperature gradient is carried by the trapped particle population then the feature can only relax via collisions: Either by transferring energy to cold passing particles or by scattering out of the trapping velocity space [1],

$$\left| \frac{v_{\parallel}}{v_{\perp}} \right| < \sqrt{2 \frac{r}{R}} \quad (6.10)$$

$$\text{after, } \tau_{detrapp.} = 2 \frac{r}{R} \tau_{coll.} \quad (6.11)$$

for $R = 1.65$ m, $r \approx 0.15$ m, we find $\tau_{detrapp.} \approx 200 \mu s$. This value agrees with the $300 \rightarrow 700 \mu s$ plume relaxation times observed by the SXR tomography.

The hypothesis is as follows: a fraction of the hot particles ejected from the core and become trapped by a magnetic mirror on the low-field side of the plasma. These trapped particles follow so called "Banana" orbitals, which are crescent shaped features located on the low-field side of the plasma, see chapter 2.5. This is consistent with the shape of the plume. The width of this feature (≈ 1 cm) suggests that the particles are trapped in many orbitals at different minor radii. The outflux of hot particles occurs within $50 \mu s$, which means that a significant number of deeply trapped particles at the beginning of the crash will still be trapped at the end i.e. $\tau_{crash} \ll \tau_{detrapp.}$. This results in a finite poloidal temperature gradient which can only relax on a time scale of $\tau_{detrapp.}$. Although this hypothesis can qualitatively account for the plume, a full quantitative model requires sophisticated particle simulations and passes beyond the scope of this thesis.

Chapter 7

MHD Modes and Confinement

The improved H-mode scenario is characterised by high confinement and stability. This is due, in part, to the increased pedestal top pressure with respect to standard H-mode discharges. Interestingly, no improved H-mode has been observed without MHD activity. One would expect large scale plasma instabilities to degrade the plasma energy confinement through increased transport. However, observations show that the confinement is higher with MHD activity. This suggests that either the impact MHD instabilities on the energy confinement is in some way mitigated in the improved H-mode, or that MHD activity plays a role in establishing and/or maintaining the high confinement scenario.

In this chapter we will analyse the impact of MHD instabilities on the energy confinement in order to understand why the confinement is not significantly degraded by their presence. We will then show statistical evidence linking particular types of MHD activity to high confinement and examine the possible causes.

7.1 Testing The Belt Model for Confinement Loss

The impact of NTM on the plasma confinement, H , is predicted by the Belt Model, which relates the saturated island width w_{sat} and radial position of the mode, r_s , to the change in energy confinement, ΔH , [9, 10],

$$\frac{\Delta H}{H} = -\frac{15}{2} \frac{w_{\text{sat}}}{a} \left(\frac{r_s}{a}\right)^3 \sqrt{1 - \left(\frac{r_s}{a}\right)^2} \quad (7.1)$$

One of the consequences of this model is that NTMs closer to the plasma core will have less impact on the confinement. Typical q profiles are monotonically increasing from the plasma core outwards. It follows that NTMs with low values of q have less impact on the confinement. If we consider the most commonly occurring NTMs $(n+1, n)$ for a given q profile we find,

$$r_{(2,1)} \propto q_{(2,1)} = \frac{2}{1} > \frac{3}{2} > \frac{4}{3} > \frac{5}{4} \dots \quad (7.2)$$

This leads to the general expectation that the average confinement will be lower when low m number NTMs are present than when only high m number NTMs are present. Figure 7.1 confirms this statistically with super-imposed histograms of the time slice ratio, Λ ,

$$\Lambda = 100\% \frac{N_{\text{MHD}}}{N} \quad (7.3)$$

where N is the total number of time slices in each histogram bar, and N_{MHD} is the number of time slices containing a particular type of MHD mode. In this case $(5, 4)$, $(4, 3)$, $(3, 2)$, and $(2, 1)$ NTMs. Here it can be seen that the confinement is generally lower in the presence of low n NTMs than for high.

From equation (7.1) we expect $\Delta H/H \propto w_{\text{sat}}$. FIR-NTMs have their saturated island size limited due to stochastic interaction with an ideal infernal mode. This suggests that the confinement should be better in time slices containing FIR-NTMs than for the standard NTM regime. This improvement can be seen in figure 7.2 where the confinement for time slices containing $(4, 3)$ and $(3, 2)$ standard regime NTMs is compared with the confinement for $(4, 3)$ and $(3, 2)$ FIR-NTMs.

These observations qualitatively confirm equation (7.1). To test the Belt Model quantitatively it was necessary to find a number of time slices for which ΔH , w_{sat} , and r_s could be measured. The mode positions and island widths were obtained using the ECE diagnostic. The 16 kHz Nyquist frequency of this diagnostic limited the observations to $(2, 1)$ and $(3, 2)$ NTMs as these

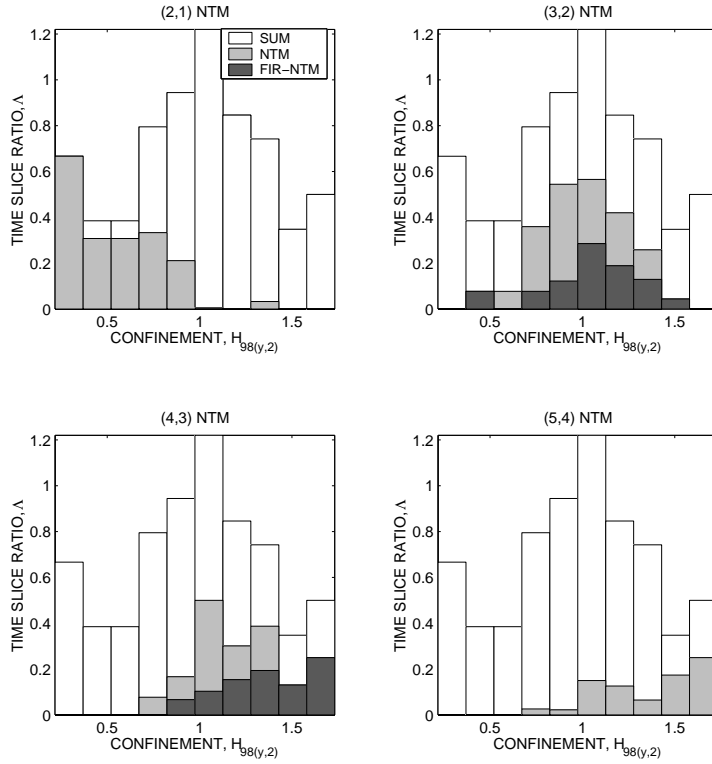


Figure 7.1: This figure shows two super-imposed histograms of confinement for time slices containing (3, 2) and (4, 3) NTMs. It can be seen that (4, 3) NTMs appear to have less impact on the confinement. (Note: the legend for the figures can be found in the top left plot)

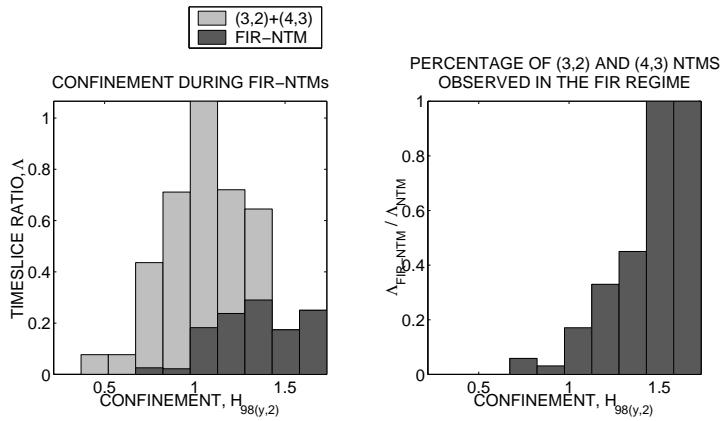


Figure 7.2: This figure compares the confinement for time slices containing NTMs in the standard and FIR-NTM regimes. The ratio of these two histograms gives us the lower plot where it can be seen that FIR-NTMs appear to have less impact on the confinement than standard regime NTMs.

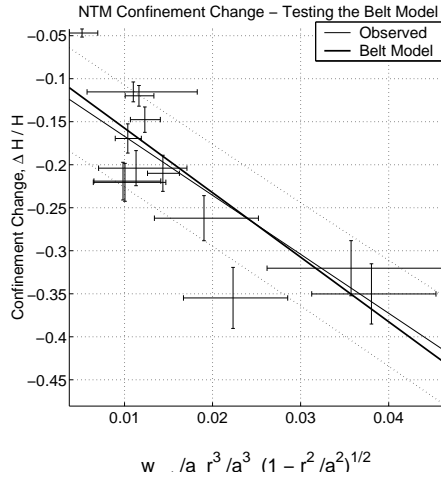


Figure 7.3: The measured confinement loss due an NTM compared with the value predicted by the Belt Model. The slope is in good agreement with the predicted value (-7 ± 3 compared to -7.5). The overall uncertainty is high due to the non-negligible uncertainty in r_s .

instabilities typically have a frequency < 16 kHz. In order to measure ΔH it is necessary to find time slices where the confinement signal before the NTM onset was stable and has a high signal to noise ratio. ΔH is taken to be the difference in H immediately before and after the NTM onset. The resulting $\Delta H/H$ is shown compared with the predicted confinement loss due to (7.1) in figure 7.3. The measured slope is in good agreement with the predicted value of $-\frac{15}{2}$ within the uncertainty. This uncertainty is high due to the non-negligible uncertainty in r_s arising from the ECE measurements, Δr_s . Δr_s is of critical importance as the term containing r_s is to the power of 3. In the future the ECE diagnostic will be upgraded to a 1 MHz Nyquist frequency and improved radial resolution. This combined with q profile reconstructions using the MSE diagnostic will greatly reduce Δr_s .

Summary

We have shown that NTMs in the improved H-mode scenario have the same impact on confinement for a given island size and radial position as they do in other regimes. If NTM activity was in any way directly beneficial to the energy confinement then one would expect this benefit to offset the confinement loss predicted by the Belt model. This does not rule out the possibility that NTMs could play a role in establishing and/or maintaining the characteristic improved H-mode current profile, thereby indirectly improving the

energy confinement. This claim will be investigated in chapter 8.

FIR-NTMs have a significantly reduced impact on energy confinement because they are unable to achieve their full saturated island size. As we discussed in chapter 6.2, the characteristic shape of the improved H-mode current profile reduces the threshold for the FIR transition. This, combined with the high β_N and $q \lesssim 1$, means that many of the NTMs in improved H-mode are FIR-NTMs.

Observations on JET suggest a reduced drive for NTMs in the low shear region, typically those with $m \geq 3$. This may seem counter intuitive as the Bootstrap term in the Rutherford equation, Δ_{bs} , is directly proportional to the scale length of the q profile, L_q , see equation (2.42). It is believed that the drive is reduced due to the global change in the current profile required to achieve a flattened central shear profile [17]. This ultimately limits the saturated island size, thereby mitigating their impact on the energy confinement.

In conclusion, there is no evidence to suggest that NTMs improve the plasma energy confinement, but rather their detrimental impact is mitigated by the improved H-mode scenario. We can tolerate the presence of (5, 4), (4, 3) NTMs, and (3, 2) FIR-NTMs, but not the (2, 1) NTM. (2, 1) FIR-NTMs are never observed, and this instability often serves as a precursor to a plasma disruption.

7.2 Sawteeth, Fishbones and Confinement

Sawteeth during the flat-top phase of improved H-mode discharges always have $\tau_{saw} \gg \tau_E$. This means that while they have a strong impact on the central kinetic profiles, the plasma quickly recovers and is not limited in terms of maximum stored energy as a result of the sawtooth activity. Figure 7.4 shows the impact of sawteeth on the energy confinement during the sawtooth envelope (from the time of the crash until the plasma kinetic profiles have recovered). We find the distribution of $H_{98(y,2)}$ values for time slices within the envelope of a sawtooth to be shifted by $\Delta H_{98(y,2)} \approx -0.02$ with respect to the mean flat-top distribution.

While this demonstrates a short-lived loss in confinement following a sawtooth crash, we find, surprisingly, that discharges containing sawteeth tend to have a higher overall confinement. The same is also true for fishbones. Figure 7.5 shows the fraction of time slices containing sawteeth (all with

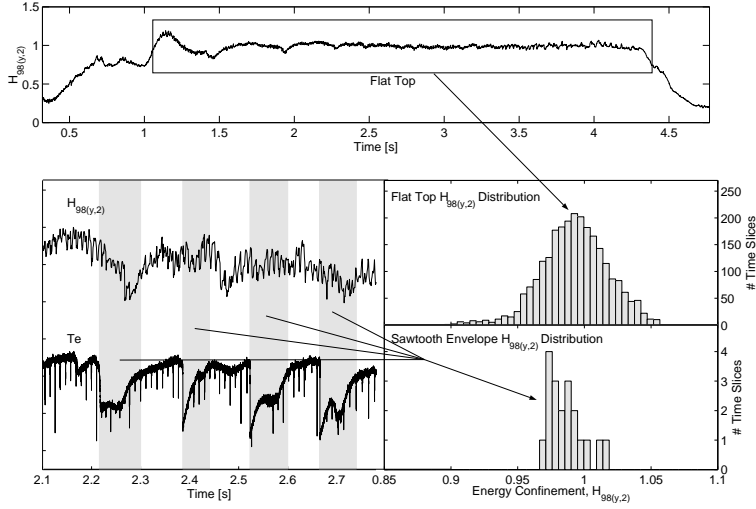


Figure 7.4: In this figure we analyse the mean energy confinement, $H_{98(y,2)}$, within the sawtooth envelope compared to the distribution of $H_{98(y,2)}$ over the flat-top region for a typical improved H-mode discharge. The sawtooth impact on the energy confinement results in a noticeable shift of $\Delta H_{98(y,2)} \approx -0.02$ in the sawtooth distribution with respect to the flat-top average.

($\tau_{saw} \gg \tau_E$) and/or fishbones as a function of the average energy confinement within that time window. There is a clear tendency for sawteeth and fishbones to be observed more often in high confinement time slices than in low. For L-mode discharges, below $H_{98(y,2)} = 0.5$, we observe many high frequency sawteeth $\tau_{saw} \leq \tau_E$ which act to significantly decrease the maximum energy confinement and plasma pressure. This would result in a sudden jump in the number of sawtooth observations below $H_{98(y,2)} = 0.5$ if L-mode discharges were included in this database.

Time slices used in this study are much longer than those used in figure 7.4, $\Delta t \sim 200$ ms, as our goal is to analyse the long time scale behaviour of the energy confinement. We also redefine a sawtooth time slice to include time slices taken between two subsequent sawtooth events less than 500 ms apart. One explanation for this apparent improved confinement is that sawteeth and fishbones directly or indirectly influence the background plasma in such a way as to improve the overall energy confinement. Another possibility is that they are symptomatic of high confinement or of another process which leads to high confinement. These explanations are not mutually exclusive. It is possible that fishbones and/or sawteeth appear as an indirect result of improved confinement, then act to maintain favourable plasma conditions.

In chapter 2.4 we discussed the importance of the characteristic flat cen-

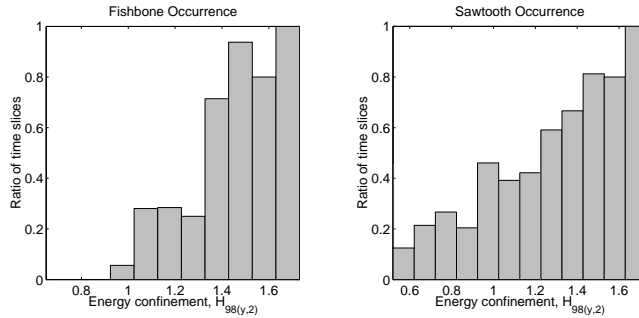


Figure 7.5: Histograms showing the fraction of time slices containing fishbones (left), sawteeth (right) as a function of the mean confinement within that time window. Both fishbones and sawteeth are found more regularly in time slices with high energy confinement than in low confinement.

tral current profile (with $q_0 \approx 1$) to the improved H-mode scenario. Achieving and maintaining this current profile is crucial to the performance of the improved H-mode. The low magnetic shear associated with a flattened q -profile reduces the plasma stability against the FIR transition, thereby mitigating the impact of NTMs on the energy confinement, see chapter 2.3.4. The observed correlation between fishbones, sawteeth and high confinement gives weight to the theory that sawtooth and fishbone reconnection periodically redistributes the central current, preventing the central q -profile from dropping below $q_0 \approx 1$. In chapter 8 we will attempt to show a direct relationship between sawtooth/fishbone reconnection and the shape of the central current profile.

Rather than directly influencing the bulk plasma, fishbones may be symptomatic of high confinement as their drive is proportional to the central fast particle pressure, β_{fast} , which shows a linear proportionality to the plasma energy confinement, $H_{98(y,2)}$. Figure 7.6 shows the near linear dependence between β_{fast} and $H_{98(y,2)}$ as observed in the improved H-mode database. Time slices with high $H_{98(y,2)}$ are more likely to have high fast particle pressure than time slices with a relatively low energy confinement. This means that if a $q = 1$ surface is present in the plasma one would expect to see fishbones more when the confinement is high than in low confinement.

As stated above, fishbone reconnection may facilitate the FIR transition by maintaining a low central magnetic shear in the plasma, thereby improving the plasma confinement by mitigating the impact of NTM activity. However, fishbones may also be purely symptomatic of the FIR-NTM in that both FIR-

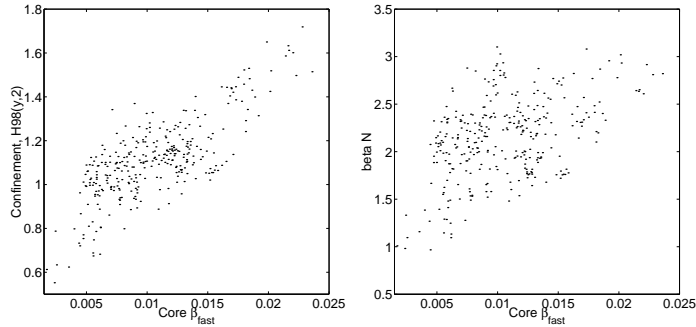


Figure 7.6: (left) Time slices observed in the improved H-mode database show a linear relationship between the plasma energy confinement, $H_{98(y,2)}$, and the core fast particle pressure, β_{fast} . (right) Time slices observed in the improved H-mode database show a rough linear relationship between, β_N , and the core fast particle pressure, β_{fast} .

NTMs and fishbones require the presence of a $q = 1$ surface in the plasma. The FIR transition occurs at high values of β_N while fishbone onset occurs for high values of β_{fast} . Figure 7.6 shows the observed linear proportionality between the two. This suggests that a time slice which satisfies the onset conditions for a FIR-NTM will also likely satisfy the onset conditions for the fishbone instability.

No such symptomatic explanation exists to explain why sawteeth are observed more regularly in high confinement time slices than in low. At least in the full reconnection model, sawteeth are destabilised at values of local magnetic shear, $s \geq s_{crit.} \propto \beta^{7/12}$, see equation (2.49). This indicates that we do not expect to see sawteeth more regularly as a result of high confinement. If anything we expect that the plasma stability against sawteeth increases slightly.

Summary

Fishbones and sawteeth do appear to be related to the improved energy confinement. It is unclear whether these instabilities are simply symptomatic of high confinement, or if they play a direct role in establishing and/or maintaining the high confinement regime. In the next chapter we will investigate the interaction between MHD instabilities and the toroidal current profile.

Chapter 8

MHD Modes and the Current Profile

In chapter 2.4 we discussed the importance of the characteristic improved H-mode scenario current profile. A number of theories exist to explain how this current profile is achieved, some of which require the interaction of MHD instabilities. In this chapter we will investigate the impact of MHD instabilities on plasma current profile. The first section is a study of fishbone and sawtooth reconnection, which potentially locks the evolution of the central current profile [21]. We then investigate the claim that NTMs can drive a current in the central plasma (in addition to the ohmic, bootstrap, and NBI current contributions) [35].

8.1 Sawtooth and Fishbone Reconnection

In chapter 7.2 it was shown that sawteeth and fishbones are observed more regularly in high confinement timeslices than in low. One possible explanation put forward was that these reconnection events are periodically redistributing the central current, thereby effectively fixing the central q . This leads to a flattening the central q profile, which in turn reduces the drive for the NTM instability, and reduces the plasma stability against the FIR transition. Both effects reduce the impact of NTMs on the energy confinement. This theory was first put forward to explain the disagreement between recon-

structured equilibria and those predicted by the ASTRA transport code [21]. ASTRA predicted that the value of q_0 would fall continuously throughout

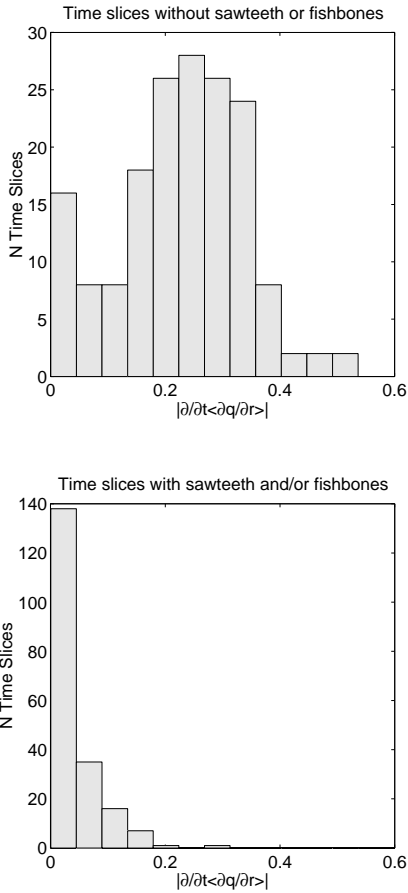


Figure 8.1: This figure shows how the time evolution of the central q profile, $|\partial/\partial t \langle dq/dr \rangle|$, reaches a near standstill in timeslices containing fishbones and/or sawteeth (bottom) compared to those without (top).

the discharge, while experimental results indicated that q_0 was remaining more or less constant. It is further supported by observations in chapter 6.4 where it was seen that the local magnetic shear at $q = 1$ rises sharply to the critical value required to destabilise the sawtooth instability, at which point the shear suddenly stops increasing and remains constant while the sawteeth are present.

Now we will show that the gradient of the entire central q profile ($r \approx 0 \rightarrow a/2$) becomes locked when fishbones and/or sawteeth appear. First we define the mean gradient of the central q profile as $\langle dq/dr \rangle \equiv [q(a/2) - q_0]/(a/2)$. We then study the evolution of $\langle dq/dr \rangle$ with time for timeslices before, during and after the appearance of sawteeth and/or fishbones. In each case $\langle dq/dr \rangle$ increases until the instability appears, then remains essentially constant. A polynomial fit was applied to each time series in order to estimate the time derivative $\partial/\partial t \langle dq/dr \rangle$. A histogram of $|\partial/\partial t \langle dq/dr \rangle|$ summarises the results of all time slices, see figure 8.1. This shows that the evolution of the central q profile becomes consistently frozen in the presence of sawtooth and fishbone reconnection.

8.2 Impact of NTMs on the Current Density Profile

There is an observed mismatch between the expected current density profiles and those resulting from the equilibrium reconstructions [35]. It is expected that the total toroidal current density, j_ϕ , is a sum of the bootstrap, $\langle \mathbf{j} \cdot \mathbf{B} \rangle_{boot}$, neutral beam driven, $\langle \mathbf{j} \cdot \mathbf{B} \rangle_{aux}$, and ohmic, $\sigma \langle \mathbf{E} \cdot \mathbf{B} \rangle$, plasma currents (8.1). The resulting discrepancy, observed on other tokamaks, is illustrated in figure 8.2. Note that there is an overall mismatch in the integral between the two curves, suggesting a discrepancy in the overall plasma current, ΔI_P .

$$\Delta j = j_\phi - [\langle \mathbf{j} \cdot \mathbf{B} \rangle_{boot} + \langle \mathbf{j} \cdot \mathbf{B} \rangle_{aux} + \sigma \langle \mathbf{E} \cdot \mathbf{B} \rangle] \quad (8.1)$$

On ASDEX Upgrade, the neutral beam driven current, $\langle \mathbf{j} \cdot \mathbf{B} \rangle_{aux}$, has been calculated by the FAFNER fast particle code.

The CLISTE equilibrium code was used to calculate $\langle \mathbf{j} \cdot \mathbf{B} \rangle_{boot}$, $\sigma \langle \mathbf{E} \cdot \mathbf{B} \rangle$, and the total current density, j_ϕ . These reconstructions were constrained by the plasma kinetic profiles, FAFNER fast particle simulations, and the MSE diagnostic. This last constraint is crucial, as little else can constrain the central current density profile.

The first goal was to confirm the existence of the toroidal current discrepancy, Δj , by calculating the 3 current components, $\sigma \langle \mathbf{E} \cdot \mathbf{B} \rangle$, $\langle \mathbf{j} \cdot \mathbf{B} \rangle_{boot}$, and $\langle \mathbf{j} \cdot \mathbf{B} \rangle_{aux}$. Figure 8.3 shows the resulting current density profiles for an arbitrary timeslice in the improved H-mode database. This matches observations reported on other tokamaks. A current discrepancy found by subtracting the reconstructed, j_ϕ , from the expected sum of the 3 current contributions. This discrepancy is almost exclusively negative with respect to the toroidal current direction.

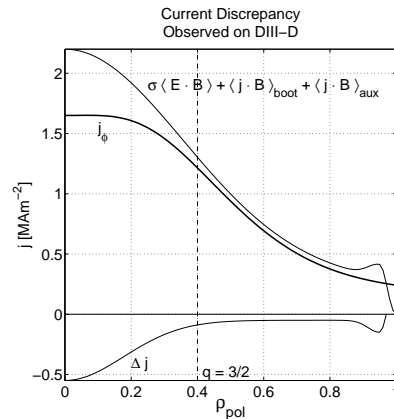


Figure 8.2: The three current density profiles $\langle \mathbf{j} \cdot \mathbf{B} \rangle_{boot}$, $\sigma \langle \mathbf{E} \cdot \mathbf{B} \rangle$, and $\langle \mathbf{j} \cdot \mathbf{B} \rangle_{aux}$ fail to account for the observed j_ϕ resulting from equilibrium reconstructions. There remains a discrepancy current, Δj [35].

Δj has been found for all time slices in the improved H-mode database. Figure 8.4 shows a histogram of the mean core averaged value of the Δj profile between $\rho_{pol} = 0 \rightarrow 0.2$, $\langle \Delta j \rangle_{core}$, for all time slices, compared with a histogram for only those timeslices containing NTM activity. It can be seen that there is no apparent statistical relationship between NTM activity and

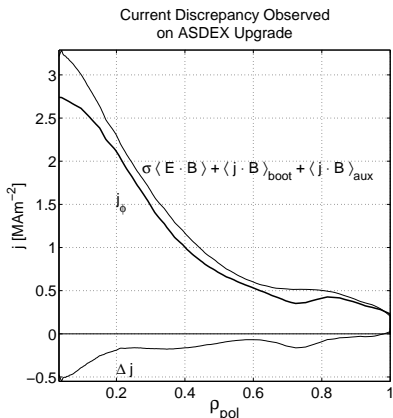


Figure 8.3: The existence of a current discrepancy has been confirmed on ASDEX Upgrade. A predominately negative difference between the observed j_ϕ and the sum of the 3 contributions $\sigma \langle \mathbf{E} \cdot \mathbf{B} \rangle, \langle \mathbf{j} \cdot \mathbf{B} \rangle_{boot}, \langle \mathbf{j} \cdot \mathbf{B} \rangle_{aux}$ has been observed for many time slices in improved H-mode database.

of the mean core current densities for the experimental and theoretical current densities we can produce a time series of $\langle \Delta j \rangle_{core}$, see figures 8.6 and 8.7. In both cases, the value of $\langle \Delta j \rangle_{core}$ varies with a standard deviation of 0.013 MA m^{-2} but does not show any net response to the NTM onset. This means that although we have observed the impact of the NTM on the current density profile in figure 8.5, this impact can be accounted for by the sum of the three current

contributions $\sigma \langle \mathbf{E} \cdot \mathbf{B} \rangle, \langle \mathbf{j} \cdot \mathbf{B} \rangle_{boot}, \langle \mathbf{j} \cdot \mathbf{B} \rangle_{aux}$ alone, i.e. it does not require the existence of a 4th current contribution. If a 4th current contribution due to the NTM onset were present, it would need to be less than 0.013 MA m^{-2} to remain undetected in the $\langle \Delta j \rangle_{core}(t)$ time series.

In shot #20853 (figure 8.6) a substantial change of 0.1 MA m^{-2} is observed in $\langle \Delta j \rangle_{core}$, some time after the NTM onset. This change is very rapid compared to the resistive timescale, occurring in less than 10 ms. Note that this jump is artificially fast because we are not taking current diffusion into account. It occurs almost exactly in time with a change in the NBI heating configuration. In this discharge the overall heating power is supplied by 4 of

the current discrepancy. To further resolve this point a high resolution study of two well diagnosed improved H-mode shots has been carried out to observe the evolution of $\langle \Delta j \rangle_{core}$ throughout the discharge. The key point of interest is to monitor how the mean core Δj responds to the NTM onset. Figure 8.5 shows the impact of the NTM on the kinetic profiles and the current density. Both the experimental and theoretical current density profiles show a reduction in the plasma centre. By taking the difference

the 8 available NBI sources. At 4.0 s the 6th NBI source abruptly stops and its contribution to the heating is carried on by the 8th beam source. Both sources inject the same power into the plasma, so there is no overall change in the average heating power. It is at exactly this time point that the sudden jump is

observed. This suggests that at least part of Δj comes from the inability of the fast particle deposition code to correctly calculate the NBI driven current. Shot #20868 shows a control case where there is no change in the heating configuration during the NTM evolution. In this case no changes are observed in $\langle \Delta j \rangle_{core}$ in excess of the standard deviation. This result is in agreement with previous work showing a discrepancy between the calculated and measured current drive due to off axis neutral beam injection [63].

In conclusion, while NTM activity does have an observable impact of the core current density profile, this impact can be accounted for purely in terms of the three current contributions $\sigma \langle \mathbf{E} \cdot \mathbf{B} \rangle$, $\langle \mathbf{j} \cdot \mathbf{B} \rangle_{boot}$, and $\langle \mathbf{j} \cdot \mathbf{B} \rangle_{aux}$. No additional source of current drive is required. The origin of the current discrepancy remains an unanswered question. However, it has been shown that at least some part of Δj is due to inaccuracies in the calculation of $\langle \mathbf{j} \cdot \mathbf{B} \rangle_{aux}$. An investigation into the neutral beam deposition codes responsible for the calculation of $\langle \mathbf{j} \cdot \mathbf{B} \rangle_{aux}$ is outside of the scope of this thesis, but remains an interesting topic for future work. The overall mismatch in ΔI_P may be due to the treatment of plasma impurities. A systematic error in the estimation of Z_{eff} will directly scale the calculated $\sigma \langle \mathbf{E} \cdot \mathbf{B} \rangle$ as the resistivity, $1/\sigma \approx 8 \times 10^{-8} Z_{eff} T_e^{-3/2}$ (here T_e is in keV) [1].

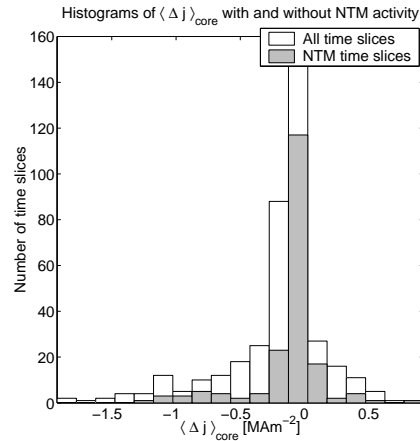


Figure 8.4: The form of the $\langle \Delta j \rangle_{core}$ histograms both with and without NTM activity have more or less the same form. If anything, those time slices with NTM activity tend to have a slightly lower absolute current discrepancy. This result suggests that Δj does not depend on the presence of NTM activity.

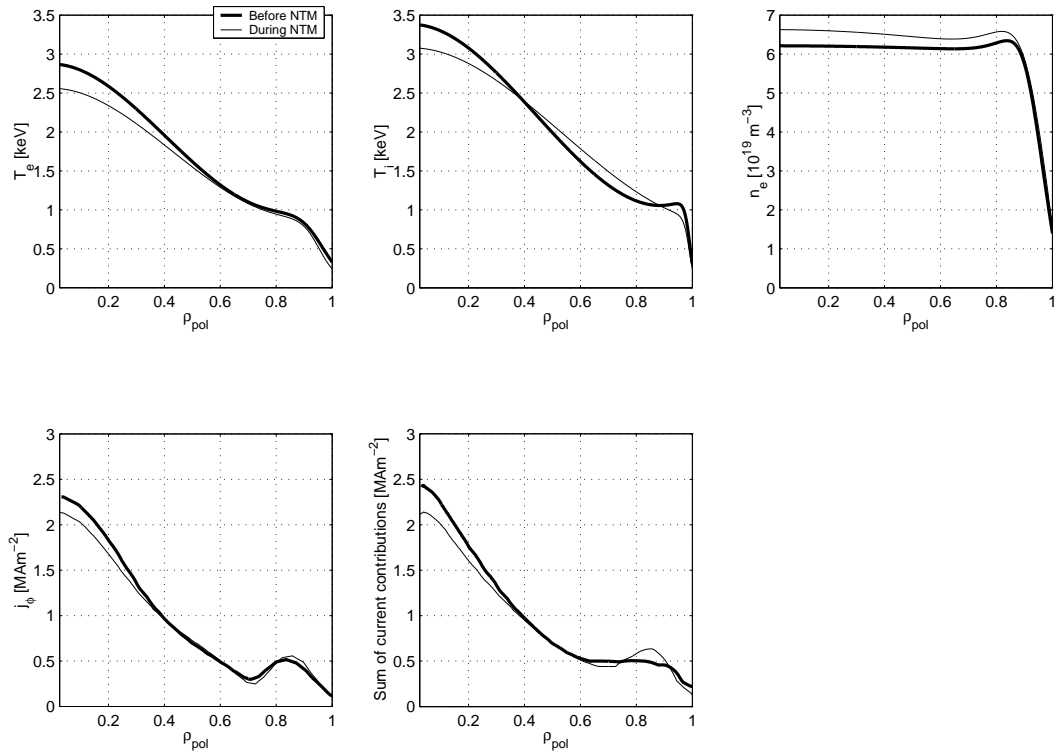


Figure 8.5: This figure shows the impact of an NTM instability on the plasma kinetic and current density profiles. The upper 3 plots show the electron and ion temperature, along with the electron density. The lower 2 plots show the reconstructed (left) and theoretical (right) current density profiles. Both show a reduction in within $\rho_{pol} = 0.3$.

Current discrepancy related to the
NBI heating configuration in #20853

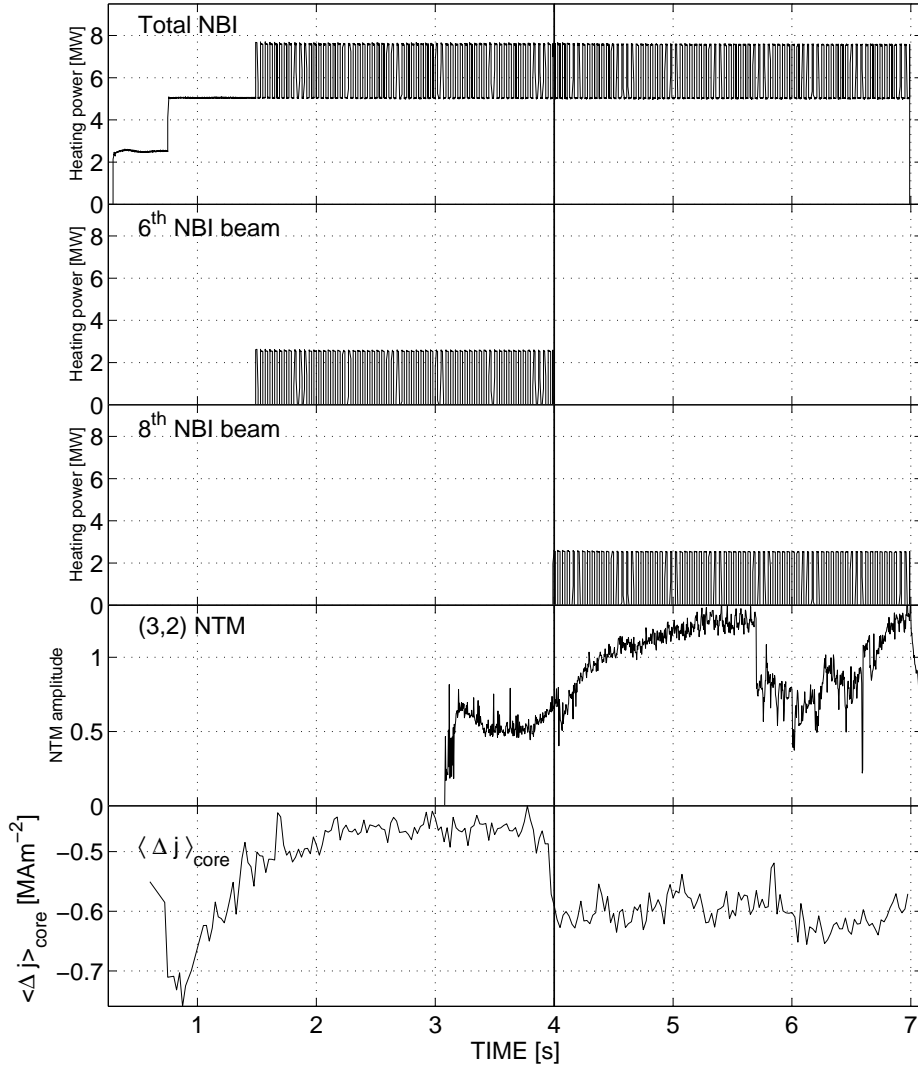


Figure 8.6: No change in $\langle \Delta j \rangle_{core}$ is observed during the NTM onset at 3.1 s. A sudden jump in $\langle \Delta j \rangle_{core}$ is observed some time later at 4.0 s. This change can be linked to a change in the NBI heating configuration rather than the evolution of the NTM. Note the changing $\langle \Delta j \rangle_{core}$ at the beginning of the shot, $t = 0.5 \rightarrow 1.5$ s. This time window is poorly reconstructed because the non-stationary current diffusion is not taken into account during the equilibrium reconstructions.

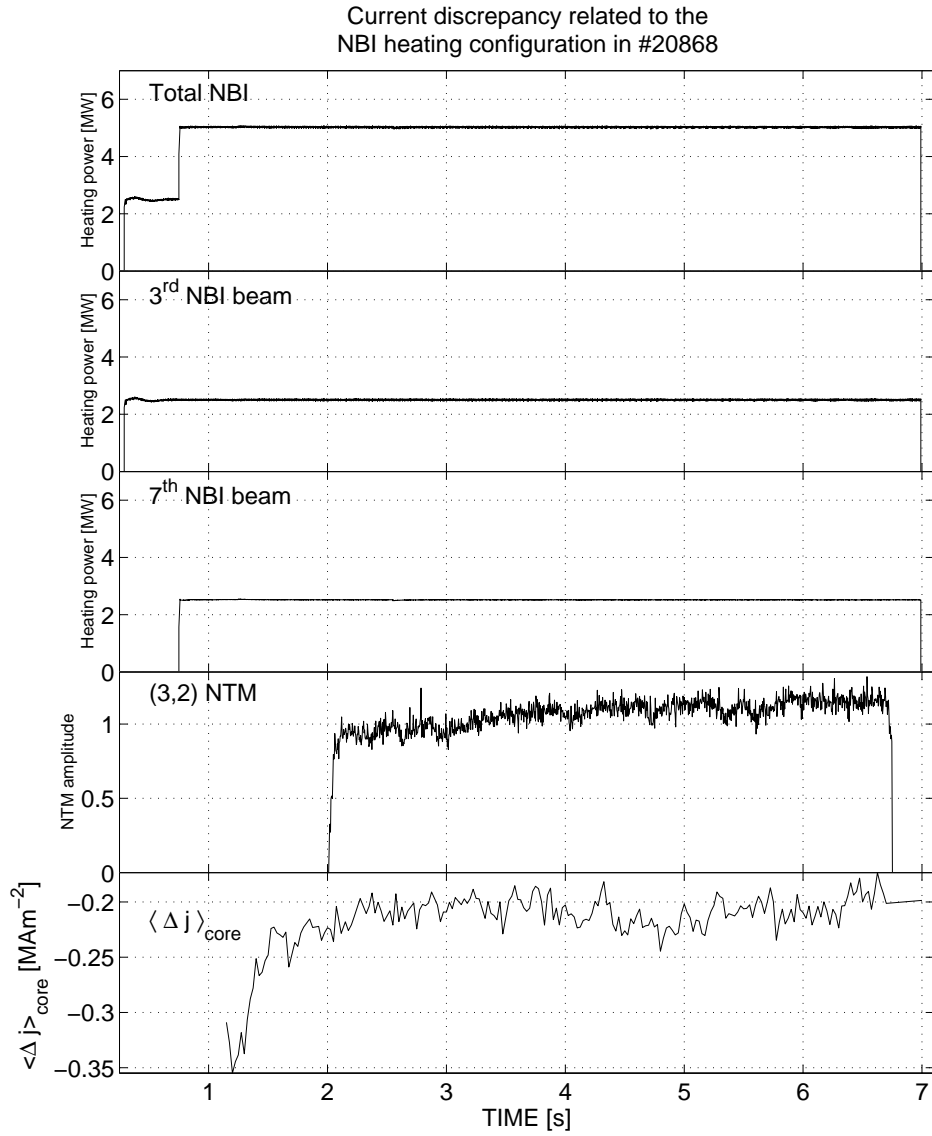


Figure 8.7: No change in $\langle \Delta j \rangle_{core}$ is observed during the NTM onset or evolution. In the previous figure a change in heating configuration appears to have caused a jump in $\langle \Delta j \rangle_{core}$. In this discharge there is no such change in the heating configuration and the value of $\langle \Delta j \rangle_{core}$ remains a constant within the standard deviation, 0.013 MA m^{-2} .

Chapter 9

Conclusions

The interaction between MHD instabilities and the plasma is of key importance for tokamak operation. Large scale instabilities can significantly degrade the energy confinement or even result in a complete disruption of the plasma discharge. In addition to their detrimental impact on the plasma there have been observations indicating that certain MHD instabilities may play a role in establishing the so called improved H-mode scenario (an operational regime which simultaneously achieves high energy confinement and plasma stability, a candidate for long pulse hybrid operation on ITER) [35, 21]. This provided the motivation for this thesis: we have characterised MHD instabilities observed in improved H-mode discharges on ASDEX Upgrade and determined under which conditions these instabilities appear. Their impact on the plasma energy confinement has been quantified. Finally we have investigated claims that MHD instabilities play a role in achieving the improved H-mode scenario through interactions with the toroidal current profile.

To make these investigations possible a database of MHD instabilities was constructed using time slices taken from 166 ASDEX Upgrade improved H-mode discharges. For each time slice the plasma conditions were recorded including quantities such as the plasma stability, energy confinement, fast particle pressure, fitted kinetic profiles, equilibrium reconstructions, etc. Additionally the presence/absence of the following 4 types of MHD instability were recorded: Neoclassical tearing modes (NTM), frequently interrupted regime NTMs (FIR-NTM), fishbones, and sawteeth, along with the following quantities: mode frequency, radial location, relative amplitude, island

width (for NTMs), normalised sawtooth amplitude, envelope and sawtooth inversion radius.¹

To aid in the construction of this database a number of new codes were implemented. This includes an automatic sawtooth detection algorithm (SAWSCAN) which identifies the onset, amplitude and inversion radius of sawteeth using ECE electron temperature measurements. A soft X-ray tomography system was also implemented using maximum entropy regularisation. In the initial implementation it was found that this regularisation was unable to converge to a physical solution in cases with relatively low sight line coverage, < 70 sight lines. For this reason optional additional regularisation was added, allowing the user to include mode rotation and smoothness constraints where necessary. Examples are shown in chapters 4.6, and 6.4.2 where the soft X-ray tomography was used to reconstruct the time evolution of sawteeth and plasma disruptions in unprecedented detail for ASDEX Upgrade discharges.

With the database completed we were able to investigate the role of MHD instabilities in the improved H-mode scenario.

Onset Criteria

One characteristic of the improved H-mode is the relatively frequent occurrence of so called “spontaneous onset” NTMs (SNTMs). Unlike the precursor triggered NTMs (PNTMs) observed in standard H-mode discharges, SNTMs are not triggered by the appearance of relatively large seed islands created by fishbone or sawtooth reconnection. Instead, they grow from significantly smaller island sizes, close to the diagnostic sensitivity limits. This growth has two distinct phases. The initial phase appears to have an exponential growth character, rising sharply from the noise level, which then makes a transition to the linear resistive NTM growth rate.

The mechanism behind the initial growth phase is not currently understood. We present the following hypothesis: an ideal MHD mode is destabilised for high β and/or low magnetic shear, not dissimilar to the ideal infernal mode involved in the FIR-NTM mechanism. Under normal circum-

¹Radial location and island width were subject to the limited availability of the Soft X-ray (SXR) diagnostic and the Nyquist/spatial-resolution limits of the Electron Cyclotron Emission (ECE) diagnostic, and were therefore not available for every timeslice in the database.

stances this instability would saturate quickly, growing and decaying on the ideal MHD timescale. However, when the drive for this mode is high enough that its perturbation exceeds the minimum seed island size for the NTM onset, w_{min} , the system will make a transition to linear resistive growth, eventually saturating at an island size, w_{sat} .

This model goes some way to explain why this type of NTM onset is observed more regularly in improved than in standard H-mode discharges. The characteristic flattened q profile acts to reduce the plasma stability against the ideal mode, while the high β not only increases the drive for the ideal instability but also reduces the value of w_{min} required for NTM growth.

If we take this model to be true, we find that the ratio of seed and saturated SNTM island sizes, w_{seed} , w_{sat} , must be fixed for a given set of plasma conditions, e.g. poloidal β , q pressure profile scale lengths, etc. This was verified in chapter 6.1, where it was shown that SNTMs could be positively identified by comparing the ratio w_{seed}/w_{sat} as predicted by the Rutherford equation with w_{seed}/w_{sat} as inferred from relative island size measurements.

This relationship allowed us to infer the average size of naturally occurring seed islands in improved H-mode plasmas by solving the Rutherford equation for w_{seed} during the onset of SNTMs observed in the improved H-mode database. This yielded a value of $w_{seed} = 0.95 \pm 0.40$ cm. Although it is not possible to directly confirm with ECE measurements of w_{seed} (due to the limited spatial resolution of this diagnostic) it was possible to infer an approximate w_{seed} using ECE measurements of w_{sat} and extrapolating back to w_{seed} using the relative mode amplitude (as measured by the external magnetics). This study yielded values of $w_{seed} = 1.3 \pm 0.7$ cm, which is in good agreement with the result above, albeit with a relatively high uncertainty.

Observations of the onset conditions required for NTMs to enter the frequently interrupted regime have found a β_N threshold of $\beta_N \geq 2.0$, which is slightly lower than the threshold reported in previous literature, $\beta_N \geq 2.3$ [17]. This can be explained by the characteristic improved H-mode profile. The central shear is low compared to standard H-mode discharges, which in turn lowers the plasma stability against the ideal $(m+1, n+1)$ infernal mode (which is a key ingredient for the FIR-NTM) without necessarily requiring an increase in the radial separation of the $(m+1, n+1)$ and (m, n) rational surfaces, see chapter 6.2 for details.

Fishbones were found to occur within the range $q_0 < 1.0$ and $\beta_{fast} \geq 0.0075$ (where β_{fast} refers to the core fast particle pressure). The first onset criterion comes as no surprise as fishbones result from fast particle interaction

with a $(1, 1)$ instability, i.e. there must exist a $q = 1$ surface, therefore q_0 must be less than one. This result simply shows that our reconstructions of the central q profile are reasonably accurate, at least when MSE pitch angle information is available to constrain the equilibrium reconstructions. The second criterion is slightly lower than that found for standard H-mode discharges, $\beta_N \geq 0.009$ [56].

Furthermore, it was shown that in every instance where fishbone activity is suppressed by either a sawtooth crash or NTM onset, the disappearance and subsequent reappearance of fishbone activity can be explained purely in terms of the core β_{fast} threshold. The fishbones disappear as soon as the core β_{fast} is reduced below $\beta_{fast}^{crit.}$ for the discharge, and reappear as soon as β_{fast} recovers to $\beta_{fast}^{crit.}$. Note, in order to calculate β_{fast} in the presence of an NTM we have made the assumption that NTMs affect both the thermal and fast particle populations in the same way. Secondly, we could not calculate β_{fast} during the sawtooth crash as the timescale of the crash is much shorter than the ion slowing down time, τ_{sd} , used to calculate β_{fast} . However, the reappearance of the fishbones during the recovery phase of the sawtooth envelope is accurately predicted by this method.

This result is significant as, in some models, the sawtooth and NTM instabilities suppress $(1, 1)$ activity by increasing the value of q_0 above unity, either through total reconnection (in the case of sawteeth) [23], or through a process of NTM current drive [35]. The observations above show that neither process is necessary to explain fishbone suppression.

The onset conditions for the sawtooth instability were found to be $q_0 < 1$, and a local shear, s at the $q = 1$ surface in excess of $s_{crit.}$, (2.49), which is in good agreement with theoretical predictions [23]. However, while no sawteeth were observed below the critical shear, it was found that not all discharges which satisfied the Porcelli onset conditions contained sawteeth. These observations highlight the need for a complete model of sawtooth stabilisation including the stabilising effects of energetic ions and toroidal rotation [59, 60].

Impact on Confinement

The impact of NTMs on the energy confinement is predicted by the Belt Model (7.1) which relates the relative change in energy confinement, $\Delta H/H$, to the saturated island size of the NTM and its radial location. In chapter 7.1 it was shown that NTMs observed in improved H-mode discharges show a near perfect agreement with the Belt Model.

It was also found that those time slices containing FIR-NTMs statistically achieve a higher energy confinement than those containing standard regime NTMs. This is an expected result as stochastic interaction between the FIR-NTM and an ideal infernal mode located on a nearby rational surface effectively prevents the NTM from reaching its full saturated island size, thereby mitigating its impact on the energy confinement.

Fishbones and sawteeth are observed statistically more often in time slices with high energy confinement than in low ones. This result is somewhat surprising as a short term loss in confinement is observed during the sawtooth envelope. However, averaging over long time scales, discharges containing sawteeth and fishbones achieve higher energy confinement than those without. This suggests that they are either symptomatic of high confinement, or that they in some way play a role in establishing favourable plasma conditions. The latter is in agreement with previous studies where it was suggested that fishbone/sawtooth reconnection may periodically redistribute the plasma current. This process effectively locks the evolution of the central current profile, which in turn leads to the characteristic flattened improved H-mode q profile.

Interaction with the Current Profile

Finally, we have investigated the interaction between MHD instabilities and the plasma current profile. Observations on the DIII-D tokamak reported that current appears to be driven by NTM modes. This current is in addition to the 3 standard current contributions, namely: the ohmic, bootstrap and NBI driven currents [35]. This was investigated by comparing the total reconstructed current density profile, fitted to the experimental results, with the sum of the 3 standard current contributions. It was found that although NTMs have a measurable impact on the current profile this impact can be accounted for purely in terms of the 3 standard current contributions without requiring a 4th current source. The sensitivity limits of this study suggest that, if a 4th contribution is present, it must be less than 0.013 MA m^{-2} .

While the NTM impact on the current density profile does not require a 4th current contribution, a general mismatch between the experimental and theoretical current profiles has been observed. It has been shown that this mismatch comes, at least in part, from the fast particle simulations responsible for the calculation of the neutral beam driven current. Another source for this discrepancy may come from the treatment of plasma impurities. A slight

change in the the effective Z of the plasma will adjust the plasma resistivity, and thereby the ohmic current contribution.

As we mentioned before, although a short term loss in confinement is observed due to sawteeth, discharges containing fishbones and sawteeth tend to have higher energy confinement than those without. This suggests that they may play some role in establishing favourable plasma conditions. In chapter 8.1 it was shown that the evolution of the central magnetic shear consistently locks in the presence of sawteeth and fishbones, suggesting they do indeed play a role in establishing and maintaining the characteristic improved H-mode current profile.

The form of the improved H-mode current profile plays a central role in improving both the energy confinement and plasma stability. It simultaneously reduces the threshold for the FIR transition and the NTM drive. While it appears that both sawteeth and fishbones can help establish this regime, fishbones are preferred as they are less prone to triggering NTMs [21]. A certain level of $n \geq 2$ NTM activity can be tolerated as their impact can be mitigated through reduced drive and FIR crashes. However, low n NTMs such as the $(2, 1)$ must be avoided as they will significantly degrade the energy confinement and can often result in disruptions. It is also believed that the low central magnetic shear prevents the occurrence of high frequency sawteeth which can limit the achievable plasma β .

Appendix A

ASDEX Upgrade

Axial Symmetric Divertor Experiment		
Major plasma radius	R_0	1.65 m
Minor plasma radius	a	0.5 m
Plasma height	b	0.8 m
Plasma elongation	$s = b/a$	1.6
Plasma aspect ratio	A	3.3
Plasma volume	V_{plasma}	13 m ³
Plasma density	n	$\leq 3 \times 10^{20} \text{ m}^{-3}$
Plasma mass		3.3 mg
Plasma current	I_P	2 MA
Discharge duration	t_D	10 s
Average plasma temperature	$T_i \approx T_e$	5 keV
Additional heating power	P [MW]	20 _(NBI) , 5.7 _(ICRH) , 1.6 _(ECRH)

Bibliography

- [1] **J. Wesson**, *Tokamaks*, Clarendon Press - Oxford, (2004).
- [2] **M. Keilhacker**, *H-mode confinement in tokamaks*, Plasma Phys. Control. Fusion, **29**, 10A, (1987), 1401.
- [3] **J. Stober, et. al.**, *The role of the current profile in improved H-mode discharges in ASDEX Upgrade*, Nucl. Fusion, **47**, (2007), 728.
- [4] **C.F. Maggi, et. al.**, *Characterisitics of the H-mode pedestal in improved confinement scenarios in ASDEX Upgrade, DIII-D, JET and JT-60U*, Nucl. Fusion, **47**, (2007), 535.
- [5] **G. Becker**, *Scaling law for effective heat diffusivity in ELMy H-mode plasmas*, Nucl. Fusion, **44**, 11, (2004), L26.
- [6] **V.D. Shafranov**, in *Reviews of Plasma Physics*, edited by **M.A. Leontovich** (Consultants Bureau, New York, 1975), Vol. 2.
- [7] **P.J. Mc Carthy**, *Analytical solutions to the Grad-Shafranov equation for tokamak equilibrium with dissimilar source functions*, Phys. Plasmas, **6**, No. 9 (1999), 3554.
- [8] **G.G. Lister**, *A fully 3D neutral bream injection code using Monte Carlo methods*, (1985), Max-Planck-Institut für Plasmaphysik Technical Report, IPP 4/222.
- [9] **O. Sauter, et. al.**, *Partial Stabilisation of NTMs with ECCD for standard scenarios in ITER*, In. Europhys. Conf. Abstr., Vol 29C, (2005)
- [10] **S. Günter, et. al.**, *Influence of neoclassical tearing modes on energy confinement*, Plasma Phys. Control. Fusion. **41** (1999) 767-774.

- [11] **L. Urso, M. Maraschek, H. Zohm**, *Fitting of the Rutherford Equation for Neoclassical Tearing Mode Stabilisation in ASDEX Upgrade*, Institute of Physics Publishing, Journal of Physics: Conference Series **25** (2005) 266-273.
- [12] **L. Urso**, *Modelling and experiments on NTM stabilization at ASDEX Upgrade*, Ph.D. Thesis, Ludwig-Maximilians-Universität München, (2008).
- [13] **Q. Yu., S. Günter, K. Lackner**, *Numerical modelling of nonlinear growth and saturation of neoclassical tearing modes*, (2004) *Phys. Plasmas* **11**, 140.
- [14] **H. Lütjens, J. Luciani**, *Curvature effects on the dynamics of tearing modes in tokamaks*, *Phys. Plasmas*, **8**, No. 10, 4267.
- [15] **J.P. Meskat, H. Zohm, G. Gantenbein, S. Günter, M. Maraschek, W. Suttrop, Q. Yu, and the ASDEX Upgrade Team**, *Analysis of the structure of neoclassical tearing modes in ASDEX Upgrade*, *Plasma Phys. Control. Fusion*, **43**, (2001), 1325.
- [16] **A. Gude, et.al.**, *Temporal evolution of neoclassical tearing modes and its effect on confinement reduction in ASDEX Upgrade*, *Nucl. Fusion*, **42**, (2002), 833.
- [17] **S. Günter, et.al.**, *The frequently interrupted regime of neoclassical tearing modes (FIR-NTMs): required plasma parameters and possibilities for its active control.*, *Nucl. Fusion*, **44**, (2004), 524.
- [18] **L. Chen, R.B. White, M.N. Rosenbluth**, *Excitation of Internal Kink Modes by Trapped Energetic Beam Ions*, *Phys. Rev. Lett.*, **52**, (1984), 1122.
- [19] **B. Coppi, F. Porcelli**, *Theoretical Model of Fishbone Oscillations in Magnetically Confined Plasmas*, *Phys. Rev. Lett.*, **57**, (1986), 2272.
- [20] **R.B. White, et. al.**, *Theory of mode-induced beam particle losses in tokamaks*, *Phys. Fluids*, **26**, (1983), 2958.
- [21] **S. Günter, et. al.**, *The influence of fishbones on the background plasma*, *Nucl. Fusion*, **39**, (1999), 1535.

- [22] **A. Gude, S. Günter, S. Sesnic, ASDEX Upgrade Team**, *Seed islands of neoclassical tearing modes at ASDEX Upgrade*, Nucl. Fusion, **39**, (1999), 127.
- [23] **F. Porcelli, D. Boucher, M.N. Rosenbluth**, *Model for the sawtooth period and amplitude*, Plasma Phys. Control. Fusion, **38**, 12, (1996), 2163.
- [24] **A.M. Mück**, *Study of the Sawtooth Instability and its Control in the ASDEX Upgrade Tokamak*, Dissertation, Technischen Universität München, Juni, 2004.
- [25] **A. Letsch, et. al.**, *Incomplete reconnection in sawtooth crashes in ASDEX Upgrade*, Nucl. Fusion, **42**, (2002), 1055.
- [26] **V.S. Udintsev, et. al.**, *Experimental observation of $m/n = 1/1$ mode behaviour during sawtooth activity and its manifestations in tokamak plasmas*, Plasma Phys. Control. Fusion, **47**, (2005), 1111.
- [27] **V. Igochine, O. Dumbrajs, H. Zohm, A. Flaws, and the ASDEX Upgrade Team**, *Stochastic sawtooth reconnection in ASDEX Upgrade*, Nucl. Fusion, **47**, (2007), 23.
- [28] **A.J. Lichtenberg, et. al.**, *The role of stochasticity in sawtooth oscillations*, Nucl. Fusion, **32**, (1992), 495.
- [29] **A. Staebler, et. al.**, *The improved H-mode at ASDEX Upgrade: a candidate for an ITER hybrid scenario*, Nucl. Fusion, **45**, (2005), 617.
- [30] **A. Sips, et. al.**, *The performance of improved H-modes at ASDEX Upgrade and projection to ITER*, Nucl. Fusion, **47**, (2007), 1485.
- [31] **P.J. Mc Carthy, et. al.**, *Current profile identification on ASDEX Upgrade via motional stark effect and the CLISTE interpretive equilibrium code*, In 27th EPS conference, Budapest, Europhysics Abstract, volume 24B, 440-443, 12th – 16th June (2000).
- [32] **P.J. Mc Carthy, et. al.**, *Plasma geometry and current profile identifications on ASDEX Upgrade using an integrated equilibrium generation and interpretation system*, The 21st IAEA Fusion Energy Conference, (2006), TH/P3-7.

- [33] **O. Sauter, C. Angioni, Y.R. Lin-Liu**, *Neoclassical conductivity and bootstrap current formulas for general axisymmetric equilibria and arbitrary collisionality regime*, Phys. Plasmas, **6**, (1999), 2824.
- [34] **A.G. Peeters**, *The bootstrap current and its consequences*, Plasma Phys. Control. Fusion, **42**, (2000), B231.
- [35] **M.S. Chu, et. al.**, *Maintaining the Quasi-Steady State Central Current Density Profile in Hybrid Discharges*, Nucl. Fusion, **47**, (2007), 434.
- [36] **R.J. Groebner, et. al.**, *Progress in quantifying the edge physics of the H-mode regime in DIII-D*, Nucl. Fusion, **41**, (2001), 1789.
- [37] **I. Fidone, G. Granata**, *Electron cyclotron emission from thermal plasmas*, Plasma Phys., **21**, (1979), 315.
- [38] **H. Murmann, et. al.**, Rev. Sci. Instrum, **63**, (1992), 4941.
- [39] **H. Brocken, H. de Kluvier, F. Hendriks**, *Active ion temperature determination by energetic neutral beam probing critically discussed*, Plasma Phys. Control. Fusion, **26**, (1984), 749.
- [40] **Z. Pietrzyk, P. Bieger, D. Summers**, *Deconvolution of electron density from lithium beam emission profiles in high edge density plasmas*, Plasma Phys. Control. Fusion, **35**, (1993), 1725.
- [41] **L. Spitzer**, *Physics of Fully Ionised Gases*, Interscience, (1962), 127.
- [42] **J. Kim**, *MHD mode identification of tokamak plasmas from Mirnov signals*, Plasma Phys. Control. Fusion, **41**, (1999), 1399.
- [43] **H.A. Bethe, E.E. Salpeter**, *Quantum Mechanics of One- and Two-Electron Atomics*, Springer-Verlag, Berlin, (1957).
- [44] **R. Wolf**, *Measurement of the Local Magnetic Field Inside a Tokamak Plasma (JET) by Means of the Motional Stark Effect and Analysis of the Internal Magnetic Field Structure and Dynamics*, PhD Thesis, Univ. Düsseldorf, (1993).
- [45] **H. Zohm**, *Untersuchung magnetischer Moden am Tokamak ASDEX*, Dissertation, Universität Heidelberg, Oktober, (1990).

- [46] **F. Reif**, *Fundamentals of Statistical and Thermal Physics*, Mc Graw-Hill, Boston, (1965).
- [47] **I.H. Hutchinson**, *Principles of Plasma Diagnostics*, Cambridge University Press, (1987).
- [48] **C.P. Tanzi**, *Emission of Soft X-Ray and Microwave Radiation from Tokamak Plasmas*, Ph.D. Thesis, FOM Instituut voor Plasmafysica, Rijhuizen, The Netherlands, (1996).
- [49] **C. Görner**, *Tomographische Untersuchung von globalen Alfvén-Eigenmoden am Stellarator Wendelstein VII-AS*, Dissertation, Technischen Universität München, Juli, 2002.
- [50] **M. Anton, et.al.**, *X-ray tomography on the TCV tokamak*, Plasma Phys. Control. Fusion **38** (1996) 1849-1878.
- [51] **J.W. Cooney, J.W. Tukey**, *An Algorithm for the Machine Computation of the Complex Fourier Series*, Mathematics of Computation, **19**, (1965), 297.
- [52] **J. Berrino, et. al.**, *Electron cyclotron emission temperature fluctuations associated with magnetic islands and real-time identification and control system*, Nucl. Fusion, **45**, (2005), 1350.
- [53] **R. Fitzpatrick**, *Helical temperature perturbations associated with tearing modes in tokamak plasmas*, Phys. Plasmas, (1995), 2:825.
- [54] **G. Golub, C. Van Loan**, *Matrix Computations*, 3e., Johns Hopkins University Press, Baltimore, (1996).
- [55] **C.C. Hegna, J.D. Callen**, *Ideal ballooning stability near an equilibrium magnetic island*, Phys. Fluids B, **4**, (1992), 3031.
- [56] **T. Kass, et. al.**, *The Fishbone Instability in ASDEX Upgrade*, Nucl. Fusion, **38**, No. 6 (1998), 807.
- [57] **M. Garcia-Munoz**, *Fast Response Scintillator Based Detector for MHD Induced Energetic Ion Losses in ASDEX Upgrade*, PhD Thesis, Univ. München, (2006).
- [58] **I.T. Chapman, et. al.**, *The physics of sawtooth stabilisation*, Plasma Phys. Control. Fusion, **49**, (2007), B385.

- [59] **D.J. Campbell, et. al.**, *Stabilization of Sawteeth with Additional Heating in the JET Tokamak*, Phys. Rev. Lett., **60**, (1988), 2148.
- [60] **G.B. Crew, J.J. Ramos**, *Stabilization of the internal kink mode in finite beta toroidal plasmas*, Phys. Rev. A., **26**, (1982), 1149.
- [61] **G. Gan-cheng, et. al.**, *Compound Sawteeth and Analysis of Reversed Shear in HL-1M*, Plasma Sci. Technol., **2**, (2000), 437.
- [62] **J. Stober, et. al.**, *Dependence of the density shape on the heat flux profile in ASDEX Upgrade high density H modes*, Nucl. Fusion, **41**, (2001), 1535.
- [63] **J. Hobirk, et. al.**, *Off-axis Neutral Beam Current Drive Experiments on ASDEX Upgrade and JT – 60U*, The 30th Europhysics Conference on Controlled Fusion and Plasma Physics, St. Petersburg, (2003), Vol. 27A, O-4.1B.

Acknowledgements

I would like to thank Prof. Hartmut Zohm for the opportunity to carry out this work under his supervision. This thesis owes a great deal to his support and direction. I gained much from our discussions on plasma physics and from his advice.

I also thank Prof. Ulrich Stroth and the University of Stuttgart for supporting this thesis through to fruition.

During my time at the Max-Planck-Institut for Plasma Physics I worked together with many people and I thank all the ASDEX Upgrade team for their support and collaboration. I would like to thank the following people in particular:

I owe a great deal to Dr. Valentin Igochine for his constant friendly support during my Ph.D. He was always available to answer my questions, and taught me much about the theory and analysis of MHD instabilities.

The soft X-ray diagnostic group consisting of Dr. Igochine, Dr. Anja Gude, and myself went through a lot together, especially during the transition to the new acquisition system. I would like to thank them for their camaraderie and for their assistance with the SXR tomography system. Additionally, I thank Dr. Gude for her helpful discussions on the FIR-NTM phenomenon.

I would like to thank Dr. Marc Marascheck for all of his support and advice. In particular for his help with the MTR program, which proved to be a central work-horse in the identification and characterisation of MHD instabilities. I thank also Dr. Matthais Reich for his help with the MSE diagnostic, Dr. Wolfgang Suttrop for his help with the ECE diagnostic, and

all the other diagnosticians whose efforts made this thesis possible.

Laura Urso taught me everything I ever needed to know about neo-classical tearing modes and the Rutherford equation. I would like to thank her for her friendship, collaboration, and patience in answering my many many questions.

I thank also Prof. Patrick McCarthy for his help with the CLISTE equilibrium code. CLISTE proved instrumental in answering some of the most interesting questions posed by this thesis.

I would especially like to thank my office mate Karl Sassenberg for his friendship, advice, and coffee money. No one helped me get through this Ph.D. more than him.

Finally, I would like to thank the rest of my friends and my family who saw me through the best times and the worst.

Eidesstattliche Erklärung

Hiermit erkläre ich an Eides Statt, dass ich diese Arbeit ausschließlich unter Anleitung meiner wissenschaftlichen Lehrer und unter Verwendung der angegebenen Hilfsmittel angefertigt habe. Sie hat weder ganz noch zum Teil an einer anderen Stelle im Rahmen eines Prüfungsverfahrens vorgelegen.

Stuttgart, im Mai 2009

Asher Flaws

CURRICULUM VITAE

Asher Flaws

Name:	FLAWS, Asher Cale Bowie	Max-Planck-Institut für Plasmaphysik
D.O.B.:	19 th April 1980	Boltzmannstraße 2.
Nationality:	New Zealand	D-85748 Garching b. München
	Ireland	Germany
E-mail:	asf@ipp.mpg.de	
Office:	+49 (0) 89 3299 1294	Hans-Mielich-Straße 10.
Home:	+49 (0) 89 2018 3070	D-81543 München
Cell:	+49 (0) 176 2650 6928	Germany

EXPERIENCE AND QUALIFICATIONS

- 2005 - 2008 : Ph.D. in Physics, *Max-Planck-Institut für Plasmaphysik, München*
Development of a Soft X-ray tomography system for ASDEX Upgrade. Analysis and characterisation of the behaviour of magneto hydrodynamic instabilities in the Improved H-Mode scenario. Thesis: *The Role of MHD Instabilities in the Improved H-Mode Scenario.*
- 2004 - 2005 : Wissenschaftler zur Aushilfe, *Max-Planck-Institut für Plasmaphysik, München*
Responsible for running and maintaining the Soft X-ray diagnostic on ASDEX Upgrade.
- 2003 - 2004 : Wissenschaftliche Hilfskraft, *Ludwig Maximilians Universität, München*
Analysis of earthquake induced rotations using ring laser technology.
- 2002 - 2003 : International Quality Network, *Ludwig Maximilians Universität, München*
A study of ring laser gyroscope technology as a tool for measuring the rotations due to seismic waves. Comparison of ring laser gyroscope measurements with finite difference seismometer arrays.
- 2001 - 2003 : M.Sc. in Physics, *University of Canterbury, Christchurch, New Zealand*
Thesis: *Ring Laser Technology for Seismic Applications.*
- 1998 - 2000 : B.Sc. in Physics, *University of Canterbury, Christchurch, New Zealand*

SKILLS

Computer Skills: Programming, L^AT_EX, Web-site and User Interface Design
Programming Languages: C, C++, Java, IDL, FORTRAN, MATLAB, Unix, HTML
Languages: English (Native), German (Fluent), French (Basic)
A solid background in experimental plasma physics. Experience with signal analysis, modelling, tomography, software development and database design. Comfortable working in multidisciplinary environments and approaching new fields of research.

REFEREES

Prof. Hartmut Zohm, <i>Ph.D. Supervisor</i> Max-Planck-Institut für Plasmaphysik Boltzmannstraße 2. 85748 Garching bei München Germany	Prof. Heiner Igel, <i>Geophysics LMU</i> Ludwig Maximilians Universität Theresienstraße 41. 80333 München Germany
--	---